Diss. ETH No. 12876

Porous Support Structures and Sintered Thin Film Electrolytes for Solid Oxide Fuel Cells

A dissertation submitted to the
SWISS FEDERAL INSTITUTE OF TECHNOLOGY
ZURICH

for the degree of
Doctor of Technical Science

presented by
Julia Will
born on July, 2, 1962
Germany

ACCEPTED ON THE RECOMMENDATION OF
Prof. L.J. Gauckler, examiner
Prof. S. Virtanen, co-examiner
Dr. K. Honegger, co-examiner

Zürich, 1998

Acknowledgment

I am grateful to Prof. Gauckler for giving me the opportunity to realise this thesis in his laboratory, for his help and guidance throughout this work. He taught me to distinguish between important and unimportant things, not only in science, but also in every-day life.

Prof. Virtanen and Dr. Honegger are acknowledged for serving as co-examiners.

Prof. Bayer is gratefully acknowledged for his assistance and patient proof reading of this thesis.

I am in dept to my many colleagues at the chair of nonmetallic materials, especially to

Urs Schönholzer for holding my hand and for frequent and fruitful visits to the library,

Jens Helbig for many helpful discussions on scientific questions and for many hours of laughter in our chemical laboratory,

Markus Hütter who gave me a lot of help throughout this work,

Martin Hruschka for helpful discussions on electrophoresis,

my students Samir Al-Wakeel, Vinzenz Frauchiger, Lorenz Gubler, Hardmut Rudmann, Zhiqi Wu, and Cyril Rüegg.

Irene Urbánek for her help in navigating through the administrative maze and Peter Kocher for his technical support and for the famous apple pie,

my collegues in the SOFC "dream" team: Anja Bieberle, Martin Gödickemeier, Christoph Kleinlogel and Andreas Mitterdorfer.

Many thanks to Claudia Dreller for hundreds of funny and motivating e-mails and to Claudia Melchiorre for correcting my English.

I wish to thank my husband Norbert Scholz for his support and encouragement throughout my studies. Thanks to my parents for always believing in me.

Financial support from the Swiss Federal Office of Energy program is gratefully acknowledged.

"Begin at the beginning, go on till you come to the end, then stop."

Alice´s evidence,
Lewis Caroll, Alice in Wonderland

Table of Contents

I Support Structures and Sintered Thin Film Electrolytes for Solid Oxide Fuel Cells

Summary

Today's solid oxide fuel cell (SOFC) technology employs almost exclusively stabilized zirconia as solid electrolyte with a typical thickness of 50 - 300 µm. Due to the high specific resistivity of zirconia the cell has to be operated at temperatures of 900-1000 °C. Thinning down the electrolyte to several µm lowers the internal resistivity of the cell and allows therefore lower operating temperatures. These thin electrolytes, however, can not be the load bearing parts of the single cell any more and the anode or the cathode have to take over this function.

The approach in this work was the use of ceramic foams as support structures. The single components of the cell were built up layer by layer: first the ceramic foam is formed, followed by the tape cast active anode and a thin zirconia electrolyte.

The processing of ceramic La-Sr-Mn-Oxide (LSM) and Ni-(Ce-Gd)-Oxide (Ni-CGO) foams using the polymer sponge method was demonstrated. Foams of different pore sizes and thicknesses were produced. Properties of the sintered foams, such as density, compressive strength, and electrical conductivity as a function of the pore size and thickness were measured and compared with the requirements needed in the application of SOFCs. The joining of the separately processed tape cast active anode with the ceramic foam was achieved via dip-coating the ceramic foam and co-sintering it on the anode tape.

For the application of the electrolyte onto this porous anode the electrophoretic deposition (EPD) method was chosen. The Ni-CGO substrates used were reduced to metallic nickel at 700 °C under an H_2-atmosphere. The electrochemical conditions in the EPD-cell were investigated in more detail. Deposition of the positively charged zirconia particles was possible only on electrically conducting substrates. The layer thickness correlates linearly with the total charge transfer. A model was proposed based on a combined charge transfer and diffusion process under stationery conditions.

The colloidal preparation techniques in this work were successful applied to produce SOFC cells. The techniques were discussed and assessed. Suggestions for further improvements on cell preparations were made.

The feasibility of ceramic foams as load bearing support structures for SOFC and EPD as method for preparing thin electrolytes was demonstrated.

Zusammenfassung

In der heutigen Technologie der Festelektrolyt-Brennstoffzellen (SOFC) wird fast ausschließlich stabilisiertes Zirkonoxid mit einer typischen Dicke von 50 - 300 µm als Elektrolyt verwendet. Der hohe spezifische elektrische Widerstand dieser Materials bedingt hohe Betriebstemperaturen von 900-1000 °C. Eine Verringerung der Dicke des Elektrolyten auf einige µm erniedrigt den inneren Widerstand der Zelle, die somit bei niedrigeren Temperaturen betrieben werden kann. Ein solch dünner Elektrolyt verliert jedoch seine selbsttragende Funktion und muß mit einem Substrat unterstützt werden.

Das Träger-Substrat ist in dieser Studie ein keramischer Schaum. Die Brennstoffzelle wird nun auf diesem Schaum Schicht für Schicht aufgebaute: als erstes der keramische Schaum, gefolgt von der foliengegossenen Anode und dem dünnen Elektrolyten.

Es wurden Schaumkeramiken aus La-Sr-Mn-Oxid (LSM) and Ni-(Ce-Gd)-Oxid (Ni-CGO) mittels Abformung von Polymerschäumen hergestellt. Eigenschaften der gesinterten Schäume wie Dichte, Festigkeit bei Raum- und bei Anwendungstemperatur und elektrische Leitfähigkeit wurden als Funktion der Porengrösse und der Dicke der Schäume untersucht. Diese Eigenschaften wurden mit den Anforderungen in einer Brennstoffzelle verglichen und bewertet. Die Verbindung der getrennt hergestellten aktiven Anode und des keramischen Schaumes wurde mittels Dip Coating des keramischen Schaumes erreicht.

Als Herstellmethode für den Elektrolyten wurde die Abscheidung mittels Elektrophorese gewählt. Eine kurze Anreduktion der Substrate bei 700 °C unter H_2-Atmosphäre führte zur Bildung von metallischem Nickel und somit zu gut leitfähigen Substraten, auf denen elektrophoretisch dünne Schichten abgeschieden werden konnte. Die Schichtdicke kann im stationären Fall über die transportierte Gesamtladungsmenge ermittelt werden. Die dabei ablaufenden elektrochemischen Bedingungen wurden genauer untersucht. Für die Abscheidung wurde ein Modell vorgeschlagen, dem eine Kombination eines Ladungs-Transfers und eines Diffusionsprozesses zugrunde liegt.

Die in dieser Arbeit erprobten kolloidchemischen Herstell-Technologien führten zu funktionierenden SOFC-Elementen. Die verwendeten Methoden wurden bewertet.

Die Eignung von Schaumkeramiken als Träger-Substrate und die Abscheidung mittels Elektrophorese als Herstellmethode für dünne Elektrolyte wurde demonstriert.

II Introduction to Solid Oxide Fuel Cells

In this chapter a short overview of the principle of solid oxide fuel cells (SOFC) is given. The functions of the single components of SOFCs are explained and their processing is described. Finally, different possible designs of the basic systems are presented.

A fuel cell is an energy conversion device which directly converts the chemically stored energy of fuel gases into electrical energy via an electrochemical process. Compared with conventional methods of power generation, fuel cells offer several advantages: substantially higher conversion efficiency, easy modular construction, high efficiency under partial loads, and a much lower generation of pollutants. Compared with other types of fuel cells, the energy conversion efficiency of solid oxide fuel cells is particularly high (50-60%) due to the lack of any mechanical moving parts [1].

The main components of a SOFC single cell are the electrolyte, the anode, the cathode, and the interconnector. The set-up of **p**ositive electrode (anode), **e**lectrolyte, and **n**egative electrode (cathode) is called PEN which is shown in Fig. II-1. The interconnector provides the electronic connection between the single PEN elements and separates the gas compartments with the fuel gas from the one with the oxidant (air).

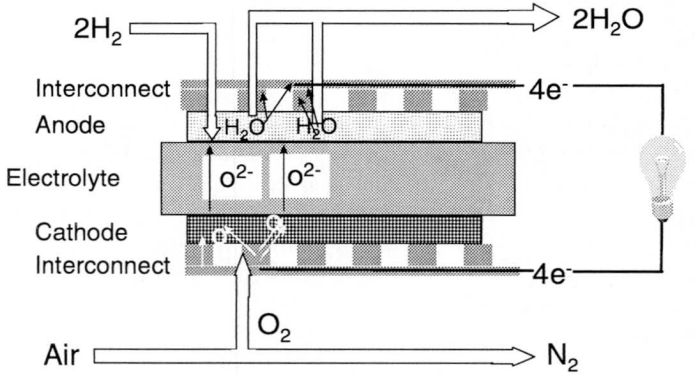

Fig. II-1: Schematic of a solid oxide fuel cell with oxygen conducting electrolyte

Fuel is supplied continuously to the anode and oxidant (air) is fed to the cathode. The solid electrolyte is an oxygen-ion-conductor. The working principle of a SOFC can be described as follows:

Oxygen is absorbed at the cathode, dissociates to 2 O which become charged to O^{2-}

$$O_2 + 4e \rightarrow 2O^{=} \qquad \textit{Eq.II-1}$$

These oxygen ions pass through the solid electrolyte and react at the anode with the fuel gas, e.g. the hydrogen

$$2H_2 + 2O^{=} \rightarrow 2H_2O + 4e^{-} \qquad \textit{Eq. II-2}$$

The overall cell reaction can be written as

$$2H_2 + O_2 \rightarrow 2H_2O \qquad \textit{Eq. II-3}$$

The driving force for the oxygen ions traveling through the electrolyte is the difference between the low oxygen chemical potential at the anode and the high oxygen chemical potential at the cathode. Under no load conditions, a cell produces ~1 V electrical potential [2].

Several PEN elements are combined to form a stack. Stacking of cells is performed to obtain higher voltages needed for technical applications. Each component of the stack has several functions and must meet certain criteria. In the following sections these requirements will be discussed.

1 Components of a SOFC

1.1 Solid Electrolyte

High efficiency fuel cells require electrolytes which must exhibit sufficient oxygen-ion conductivity (>5 S/m) and must be impermeable to the reacting gases. The electrolyte has to be stable under the prevailing oxidizing atmosphere at the cathode($p_{O_2} = 0.2$ atm) and the reducing atmosphere at the anode ($p_{O_2} = 10^{-19}$ atm). In the past most of the research work has focused on oxygen-ion-conducting stabilized ZrO_2-electrolytes [3]. The necessary dopants are selected from a large number of bivalent and trivalent metal oxides (Y_2O_3, Yb_2O_3, Sc_2O_2, CaO, MgO etc.), which stabilize the high temperature tetragonal phase or cubic zirconia phase. In the ZrO_2-Y_2O_3 system 2.5 mol% Y_2O_3 stabilizes the tetragonal and 8.5 mol% stabilizes the cubic phase [4]. The tetragonal phase is a fine grained material (grain size ~ 0.3 µm) with high mechanical strength, high toughness, and thermal shock resistance, and an ionic conductivity of 5.5 S/m at 1000° [5]. The coarse grained cubic phase has lower strength at room temperature, but a higher conductivity of around 10 S/m at 1000°C [5]. Doped ceria (CaO, Y_2O_3, Sm_2O_3, Gd_2O_3 and other rare earth oxides as dopant materials), and stabilized Bi_2O_3 develop rather high ionic conduc-

tivity. They also have been proposed as electrolyte materials for SOFCs, especially for reduced temperature operation (600– 800°C) [6, 7].
Methods for preparing the dense electrolyte include colloidal techniques such as tape-casting [8] and various deposition methods from the gas phase [9-12].

1.2 Anode

Anodes should exhibit a good electronic conductivity and a high catalytic activity for the oxidation of the fuel. Due to the reducing atmosphere at the anode metals are being used as electrodes. Ni is the preferred choice due to its low cost, but shows coarsening during manufacturing and at operational temperatures [13]. For retention of the porous anode structure and in order to reduce thermal expansion coefficient mismatches between anodes and electrolytes, the anode is a cermet composed of metal and stabilized zirconia with volume fractions of Ni/ZrO_2 from 30 to 55 vol.% Ni [14].
Methods of preparing cermet anodes include (1) conventional forming techniques such as tape casting [8], (2) coating techniques such as screen printing [15, 16] and slurry coating, and (3) deposition techniques such as plasma spraying [10] and chemical vapor deposition [17].

1.3 Cathode

The main function of the cathode is to provide reaction sites for the electrochemical reduction of the oxidant. The material used must be stable in the oxidizing environment and have sufficient electronic conductivity and catalytic activity for the oxidant gas reaction. The most common cathode material is doped La-manganite, a p-type semi-conducting perovskite [18, 19]. Doping $LaMnO_3$ with lower valent cations enhances the electronic conductivity. Sr doped La-manganite (LSM) is currently the preferred cathode material. However, interfacial reactions between cathode and electrolyte during operation limits the life of SOFCs and need to be minimized [20].

1.4 Interconnector

The interconnector (also called bi-polar plate) provides the electronic connection between the single PENs, and has to separate the fuel gas on the anode side (hydrogen, coal gas, or natural gas) from the oxidizing gas on the cathode side (air or oxygen). The interconnector is therefore directly in contact with two different reactive gas atmospheres. It must resist high temperatures of up to 1000 °C, corresponding to the operating temperature of SOFCs. The interconnector is at the same time used for current collection and as mechanically stable support for the ceramic

components of the SOFC stack. Due to these multiple functions, the interconnector requires several characteristics, such as high mechanical strength, high temperature stability, compatibility of thermal expansion coefficients, high corrosion resistance, long-term chemical stability, chemical compatibility with the adjacent components, and high electrical conductivity.

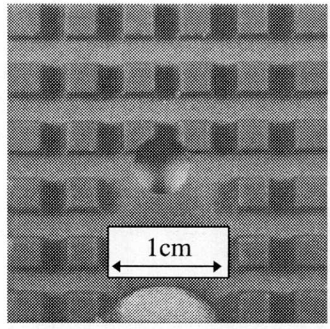

Fig. II-2: Interconnector for a planar SOFC (Sulzer design), made of X20CrN26 1 and coated with a perovskite to suppress the Cr_2O_3 evaporation [21].

Today's SOFCs utilize ceramic interconnectors made from $La_{1-x}Sr_xCrO_3$ [22], Cr-(95%)-based alloys [23] or oxide dispersion strengthened alloys [24-27]. These materials form a stable passive layer of Cr_2O_3 inhibiting a further oxidation of the metal. However, at temperatures above 800 ℃, the Cr_2O_3 layer forms volatile chromium oxides or chromium hydroxides. These products evaporate and are reduced at the cathode/electrolyte interface to form new crystalline phases giving rise to strong cell degradation [23]. The evaporation of Cr oxides can be suppressed by a dense protective layer, e.g. by deposition of perovskites via plasma or powder slurry spraying. Fig. II-2 shows a photograph of an interconnector used in the Sulzer design with a protective perovskite layer deposited via vacuum plasma spraying [21]. The use of conventional ferritic chromium steel is an inexpensive alternative but is restricted to temperatures below 750°C.

Processing techniques of ceramic interconnectors are [22, 27]: hot rolling, hot pressing and sawing, isostatic pressing, electrochemical machining and tape casting. The expensive machining of ceramics is a major drawback in the production of large components. Fabrication of a metallic interconnector is therefore advantageous with the additional benefit of higher electrical and thermal conductivity.

1.5 Fuel and Oxidant

SOFCs use hydrogen or methane which is reformed at the anode where CH_4 and H_2O react to H_2 and CO. Other potential liquid fuels are naphtha, gas oil or kerosene, or biogas and gases from biomass and landfill wastes [28].
Air is commonly used as oxidant due to its availability but pure oxygen would improve the performance of ceramic fuel cells.

2 SOFC and PEN Designs

Although there is a general consensus regarding the selection of the materials, there is still a divergence of opinion about the best configuration to be adopted for economical mass production [29]. At present, four common stack configurations have been proposed and are fabricated for SOFCs: (i) the seal-less tubular design, (ii) the segmented-cell in series design, (iii) the monolithic design, and (iv) the flat-plate design.
The tubular design of Westinghouse is by far the most advanced [30]. Stacks are built up from bundles of tubes connected with Ni felt pads. Support tubes form structural parts onto which active components are deposited via CVD/EVD or plasma spraying. The main disadvantages of this concept are the high cost of the support materials and the rather low power densities (ca. 200 mW/cm^2).
The monolithic design currently developed by Allied Signal Aerospace uses laminated corrugated structures, combined in the green state and sintered. This design has the potential for high power densities but co-sintering proves to be very difficult [31].
Currently, the most widely investigated concept is the planar or flat plate design. In this application, the components are fabricated individually and then stacked together. They are based on 100–300 μm thick self-supporting electrolytes coated with thin porous electrodes which are assembled between metallic or ceramic interconnector plates. The dimensions are limited by the mechanical stability: state-of-the-art cells are in the range of 50x50 to 100x100 mm^2. The planar concept offers high power densities, cheap fabrication methods and simplified quality control. Examples are the planar concepts of Siemens [32] and Sulzer [33]. Typical materials used for the components of the flat-plate arrangement are listed in Table II-1.
There are many possible PEN designs described in literature which are mainly developed on a laboratory scale only. They can be grouped into (1) self-supporting ones, where the electrolyte (80–300 μm in thickness) forms a structural element of the design and (2) supported concepts where the electrolyte is deposited as a thin

layer (< 50 µm in thickness) on porous support structures. Electrolytes less than 10 µm thick have reduced ohmic losses, thus allowing for efficient operation at intermediate temperatures. Supported designs can be divided into cathode supported and anode supported designs. Each of these have their own advantages and disadvantages as illustrated in Table II-2.

COMPONENT	MATERIAL	THICKNESS
Electrolyte	Stabilized Zirconia	10 - 250 µm
Anode	Ni-cermet	25 - 100 µm
Cathode	Doped $LaMnO_3$	25 - 100 µm
Interconnector	Doped $LaCrO_3$ Cr-based alloys or oxide dispersion strength. alloys	2 - 6 mm

Table II-1: PEN-Properties of the components of flat-plate SOFC-designs [34].

	ADVANTAGE	DISADVANTAGE
Anode supported	• processing sequence starts with the element with the highest sintering temperature • adjustable cathode	• low fuel utilization due to hindered gas transport through the thick anode.
Cathode supported	• high fuel utilization due to an adjustable anode	• processing sequence starts with an already rather low sintering temperature

Table II-2: Characteristics of anode and cathode supported PEN designs.

For certain cell designs, the components for a ceramic fuel cell must be amenable to special fabrication conditions, since the process can not be selected independently for each component. If the components are built-up one by one, the sintering temperature for each successive component should be lower or at least not much higher than that of the preceding one in order to avoid changes in the microstructure of the preceding component. Each arrangement has to be designed with respect to the chemical compatibility, thermal expansion matches, and processing sequence.

3 Fuel Cell Operation

A fuel cell may be considered as an oxygen concentration cell of the following type

oxygen partial pressure'/oxide solid electrolyte/ oxygen partial pressure"

where the oxygen partial pressures are at the cathode and at the anode.

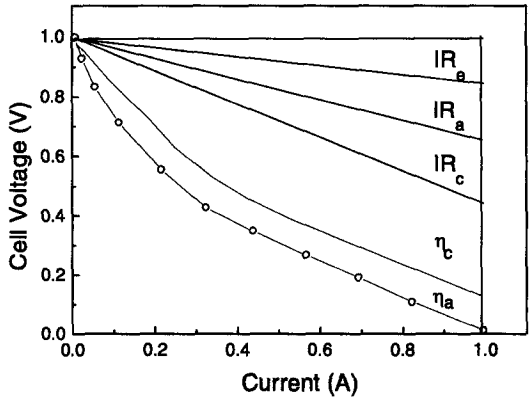

Fig. II-3: Schematic diagram of the current-voltage characteristics of a fuel cell.

The thermodynamic voltage E_{th} of this cell is given by the Nernst law

$$E_{th} = \frac{RT}{4F} \ln \frac{p(O_2')}{p(O_2'')} \qquad \textit{Eq. II-4}$$

where R, T and F are the gas constant, absolute temperature, and the Faraday constant. respectively. When an electric current I is drawn by the fuel cell, the actual operating voltage $V(I)$ is lower:

$$V(I) = E_{th} - (R_e + R_c + R_a)I - \eta_c - \eta_a \qquad \textit{Eq. II-5}$$

R_e, R_c and R_a are electrolyte, cathode, and anode ohmic resistances, respectively, whereas η_c and η_a are the cathodic and anodic polarizations. The typical current-voltage characteristic is shown in Fig. II-3.

4 The System

Compared with other fuel cell systems such as molten carbonate, alkaline, phosporic acid and polymer electrolyte fuel cells, the supporting system is very simple [35]. An overview about the peripheral units around the PEN was given by Bossel [35] and is illustrated in Fig. II-4. Conventional fuels, e.g. natural gas biogas, and propane are directly used or are cracked in the hot area of the stack. Usually, the fuel is upgraded before it is supplied to the anode. The excess heat of this high temperature fuel cell can be used to heat the air and the fuel before supplying it to the cathode or anode. The combination of high conversion efficiency and high temperature of the waste gas makes this system very attractive for industrial combined heat and power systems in the range of 100 KW-10 MW.

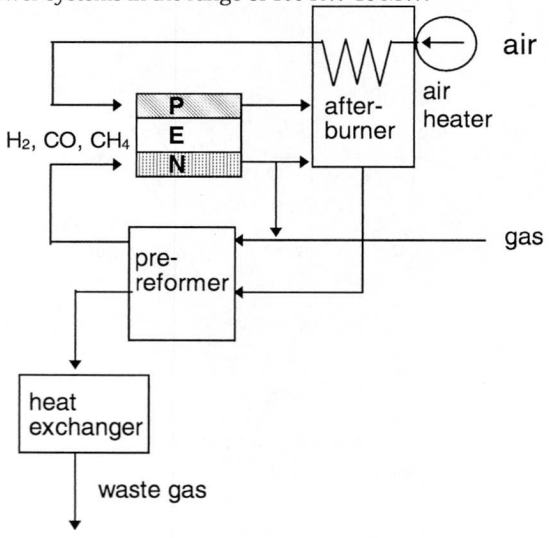

Fig. II-4: Basic system of a SOFC [35].

The Sulzer HEXIS system (as shown in Fig. II-5) has an integrated start-up burner. In normal operation mode this burner is shut-off and the SOFC module runs thermally self sustaining. This means that the stack is held on temperature only with the heat from the cells (which heated up the air) and from the afterburner, which is located directly on the outer rim of the stack. A steam reformer is thermally integrated into the SOFC module and heated with the exhaust gas from the stack. This system is operated with natural gas [33].

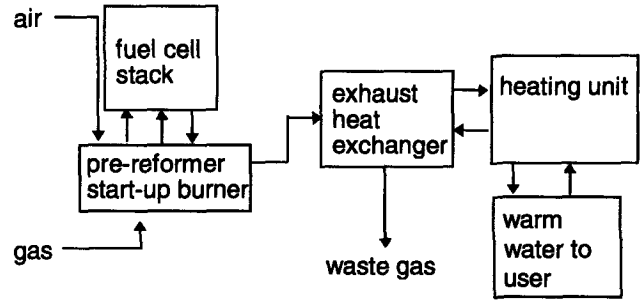

Fig. II-5: The Sulzer SOFC-design (after [33]).

5 References

[1] N. Q. Minh and T. Takehiko, "Science and Technology of Ceramic Fuel Cells", Elsevier, 1995, pp. 1.

[2] R. G. Lerner and G. L. Trigg, "Encyclopedia of Physics, 2nd ed.", New York: VCH Publishers, Inc., 1991, pp. 272.

[3] in [1] pp. 70-90.

[4] in [1] p. 77.

[5] in [1] p. 80.

[6] H. L. Tuller and A. S. Nowick, "Doped Ceria as Solid Oxide Electrolyte", *J. Electrochem. Soc.*, **122**, pp. 255, 1975.

[7] M. Gödickemeier, "Mixed Ionic Electronic Conductors for Solid Oxide Fuel Cells", Diss. ETH No. 11348, Ph.D. Thesis, ETH Zürich, 1996.

[8] J. P. P. Huijsmanns, E. J. Siewers, F. H. Van Heuveln, and J. P. de Jong, "Fabrication of Planar SOFC Components at ECN", 2nd International Symposium on SOFC, Athens, Greece, F. Grosz, F. Zegers, S. C. Singhal, and O. Yamamoto, Eds., p. 113, 1991.

[9] in [1] p. 71.

[10] L. W. Tai and P. A. Lessing, "Plasma Spraying of Porous Electrodes for a Planar SOFC", *J. Am. Ceram. Soc.*, **74**, pp. 501, 1991.

[11] M. Suzuki and A. Kajimura, "Geometrical Analysis of SOFC Anodes Fabricated by Electrochemical Vapor Deposition", *Denki Kagaku*, **65**, pp. 859-864, 1997.

[12] P. K. Srivastava, T. Quach, Y. Y. Duan, R. Donelson, S. P. Jiang, F. T. Ciacchi, and S. P. S. Badwal, "Thin Film Solid Oxide Fuel Cells Prepared by DC Magnetron Sputtering for Intermediate Temperature Operation.", 2nd Europ. SOFC Forum, B. Thorstensen, Ed., pp.761-772, 1996.

[13] in [1] pp. 153-156.

[14] in [1] pp. 159-161.

[15] Y. Matsuzaki, M. Hishinuma, T. Kawashima, Yasuda I., T. Koyama, and T. Hikita, "Current State of Planar SOFC at Tokyo Gas." , Proc. of the 3rd Int. Symp. on SOFC, Honolulu, Hawai, S. C. Singhal, Iwahara, H., Ed., 714-723, 1993.

[16] E. Erdle, W. Dönitz, W. Schäfer, and R. Schamm, "Reversibility and Polarisation Behaviour of High Temperature Solid Oxide Electrochemical Cells" , Fuel Cell Seminar Abstracts, Tucson, AZ, USA, p. 403,1992.

[17] M. Suzuki, H. Sasaki, S. Otoshi, A. Kajimura, N. Sugiura, and M. Ippommatsu, "High Performance SOFC Cathode Fabricated by Electrochemical Vapor Deposition", *J. Electrochem. Soc.*, **141**, pp. 1928-1931, 1994.

[18] in [1] p. 118.

[19] K. Kordesch and S. G., "Fuel Cells and Their Application", Weinheim: VCH Verlagsgesellschaft, pp. 134,1996.

[20] A. Mitterdorfer, "$La_2Zr_2O_7$ Formation and Oxygen Reduction Kinetics of the $La_{0.85}Sr_{0.15}Mn_yO_3$,$O_3$ (g) YSZ System", *SSI (in print)*, 1998.

[21] K. Honegger, Personal communication, Sulzer AG, Winterthur, Switzerland, 1997.

[22] J. W. Park and Y. K. Lee, "Sintering Behavior and Electrical Properties of $La_{0.7}Ca_{0.33}CrO_3$ Prepared by Doctor Blade Method", SOFC V, Aachen, Germany, U. Stimming, S. C. Singhal, H. Tagawa, and W. Lehnert, Eds., 1253-1262, 1997.

[23] J. Quadakkers, H. Greiner, and W. Köck, "Metals and Alloys for High Temperature SOFC Application", 1th European Solid Oxide Fuel Cell Forum, Lucerne, Switzerland, U. Bossel, Ed., 525-536, 1994.

[24] R. Ruckdäschel, R. Henne, G. Schiller, and H. Greiner, "Functional Layers for the Bipolar Plates of Planar Solid Oxide Fuel Cells Produced by Vacuum Plasma Spraying", [22] pp.1273-1282, 1997.

[25] K. Katayama, T. Ishihara, H. Ohta, S. Takeuchi, Y. Esaki, and E. Inukai, "Sintering and Electrical Conductivity of $La_{1-x}Sr_{-x}MnO_{-x}$ ", *J. Ceram. Soc. Jpn. Inter. Ed.*, **97**, pp. 1324-1330, 1989.

[26] H. Greiner, T. Grögler, W. Köck, and R. Singer, "Chromium Based Alloys for High Temperature SOFC Applications", SOFC IV, Yokohama, Japan, M. Dokiya, O. Yamamoto, H. Tagawa, and S. C. Singhal, Eds., pp. 879-888. 1995.

[27] M. Janousek, W. Köck, M. Baumgärtner, and H. Greiner, "Properties of Interconnect Materials", [22], pp. 1225-1233.

[28] in [1] pp. 36-38.

[29] B. C. H. Steele, "Electronic Ceramics", London: Elsevier Applied Science, pp. 20-35, 1991.

[30] S. C. Singhal, "Recent Progress in Tubular Solid Oxide Fuel Cell Technology", [22], pp. 37-50, 1997.

[31] in [1] pp. 268-280.

[32] H. J. Beie, L. Blum, W. Drenckhahn, H. Greiner, and H. Schichl, "Development of Planar SOFC at Siemens Status and Prospects", 3rd European Solid Oxide Fuel Cell Forum, Nantes, France, P. Stevens, Ed., pp. 3-14, 1998.

[33] R. Diethelm, M. Schmidt, B. Doggwiler, T. Gamper, and M. Keller, "Status of the Sulzer Hexis Solid Oxide Fuel Cell (SOFC) System Development", in [32], pp.87-94.

[34] in [1] p. 283.

[35] U. Bossel, *Brennstoffzellen, Bedeutung für die Schweiz*, Oberrohrdorf, Brennstoffzellen-Förderkreis, p. 11, 1998.

III Aim of the Study

The aim of this study is to evaluate different preparation techniques for the components of a solid oxide fuel cell (SOFC) and their sequence.

Special emphasis should be given to an anode supported cell using ceramic foam as current collector and gas distributor. Foam preparation parameters and resulting properties should be assessed. In addition, colloidal techniques should be investigated and developed for the fabrication of thin electrolytes. The electrophoretic deposition should be studied in detail using stabilized zirconia suspensions.

IV Porous Load-Bearing Structures

In this chapter an overview is given of the preparation of highly porous ceramic structures and their potential use as load-bearing electrodes and current collectors in SOFC. Properties such as compressive strength, reliability, creep, and electrical conductivity are examined.

1 Introduction

In SOFCs, the electrical resistivity can be minimized by thinning the electrolyte from several 100 µm to several µm thickness. By doing so, the ohmic losses can be reduced and the operating temperature can be lowered to achieve the same power output density. However, electrolytes can then no longer be the load-bearing parts of a single cell and the anode or cathode has taken over this function. Porous load-bearing substrates with one surface sealed may also function as interconnect in a flat plane design and are then responsible for gas distribution and current collection.

These supports have to fulfill several requirements, such as high mechanical strength, high temperature operation, thermal expansion coefficient compatibility with other SOFC elements, high corrosion resistance, long-term chemical stability, chemical compatibility with other SOFC components, and high electrical conductivity. Metals and ceramics are considered as potential support structures; ceramics are superior to metals due to their excellent strength at high temperatures. However, metal forming methods cannot be applied to ceramics [1, 2]. Another disadvantage of the metallic current collectors are their relatively small current carrying contact areas with the electrodes due to the difficulties in machining high Cr-containing metal alloys which might lead to current constrictions [3].

In the development of porous ceramic structures that are bearing the load of a cell we want to enlarge the current carrying cross section of the current collector that is in contact with the working electrodes. Our approach is to use ceramic foams. This would significantly the area and provide a large density of contact points.

2 Ceramic Foam as Load Bearing Structure in SOFC Application

Today, highly porous ceramics can be found in numerous technical fields due to their chemical inertness. Most chemical applications for ceramic foams involve either filtration or separation. Other applications of porous ceramics are known in

thermal protection, gas combustion burners, catalysis [4] and in the biomedical field as implants [5, 6]. Filtration of high temperature, high-pressure gas streams is performed by using porous ceramics [7-9]. Ceramic foam filters are used for controlling gas and diesel engine emissions [10, 11]. The most important use of open-pore ceramic foams is in filtering molten metals such as cast iron, steel, aluminum, zinc and others [12-14]. They remove nonmetallic inclusions without large pressure drop. These filters must withstand high temperatures and the corrosive attack of reactive elements. Ceramic foam must exhibit resistance to thermal cycling, high trapping efficiencies, and a low gas pressure drop Other important applications include use in manufacturing of low-mass kiln furniture for thermal protection, gas combustion burners, catalysis [6, 15], and implants in the biomedical field [15].

Porous ceramic foams are commonly classified into two types: closed-cell foams and open-cell (or reticulated) foams. The closed-cell foams have structures resembling a network of soap bubbles. The open-cell foams are identical to the closed cell ones except the membranes have been removed which produces large channels of interconnected cells, the main advantage of which is its "flow-through" capability: liquids and gases can flow through the structure with minimal resistance. Ceramic foams can be produced in many configurations and pore sizes by using a variety of different processes:

- Replication of polymeric porous structures [16], also called the polymer sponge method
- Incorporation of volatile or combustible burn-outs in a ceramic powder mix [4, 17, 18]
- Solid state sintering [17, 19]
- Sol-gel systems that develop porosity during phase transformations or chemical reactions [20-22]
- Subcritical drying of highly cross-linked inorganic gels [23]
- Sintering of materials having inclusions of hollow spheres [24-26]
- Foaming of ceramic slurries [27-30]
- Chemical leaching of glasses and glass ceramics [8, 27]
- Infiltration of a pyrolyzed polyurethane foam with various ceramics by e chemical deposition/infiltration [7].

In this work, the polymer sponge method was chosen as the method to prepare the highly porous (> 80 vol. %) support structure.

3 Preparation of Ceramic Foams

For porous structures, on the anode and on the cathode side, the same requirements are important:

1. upscalability to system required dimensions (> 100 cm^2)
2. high compressive strength at room and operating temperature (up to 950 °C)
3. low creep at operating temperatures
4. high electrical conductivity
5. chemical compatibility with adjacent PEN components in contact
6. 3-3-3 connectivity in case of porous anodes (gas, metal, ceramic)
7. high gas permeability, equivalent to a low pressure drop at a given gas flow.

The following sections describe the preparation of the porous structures, including the polymer sponge method, the ceramic suspensions, and the processing of the porous structure, as well as a list of raw materials used. The last section outlines the characteristics of the ceramic foam.

3.1 Polymer Sponge Method

Reticulated open-celled ceramics are produced via the replication of a polymeric porous structure. The patent on this technique called the "replication" or "polymer-sponge" method was first filed by Schwartzwalder and Somers in 1963 [16]. It is the standard method for producing alumina, zirconia, silicon carbide and other ceramic foams [4, 7, 11, 14, 29, 31-37]. The world production of ceramic foams is about 100 billions parts with prices of 15 to 20 cents/$inch^3$, depending on material costs [38].

The foams are manufactured by coating a polyurethane foam with a ceramic slurry. The polymer, having already the desired macrostructure, simply serves as a sacrificial substrate for the ceramic coating. The slurry infiltrates the structure and adheres to the surface of the polymer. Excess slurry is squeezed out leaving a ceramic coating on the foam struts. After drying, the polymer is slowly burned away in order to minimize damage to the porous coating. Once the polymer has been removed, the ceramic is sintered to the desired density. The process replicates the macrostructure of the polymer, and results in a rather distinctive microstructure within the struts. A flowchart of the process is given in Fig. IV-1. The struts retain a triangular void (on the 10 - 50 µm scale) from which the polymer substrate has been removed by pyrolysis, as well as the fine porosity between the ceramic grains (on the 0.1 - 5 µm scale) within the strut walls. The large-scale cellular structure consisting of a three-dimensional arrangement of solid walls will be referred to as

the macrostructure, whereas the morphology of pores and grains within the individual struts will be called microstructure.

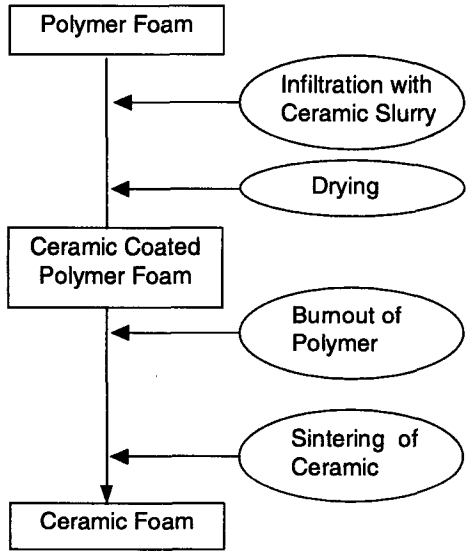

Fig. IV-1: Flowchart of the Polymer Sponge Method [16].

3.2 Raw Materials

3.2.1 Polymer Foams

There are two critical considerations for the selection of polymer sponges: one is the macroscopic pore size which determines the final pore size of the ceramic and second is the type of polymer. The pore size of the polymer foams is classified in terms of pores per linear inch: ppi. Of the polymers available for coating, polyurethane is the most attractive because of its low softening temperature and ease of burn off with low resilience [39]. Polyurethane foams are sufficiently elastic to regain their shape after compression. They are most almost manufactured from polyethers and polyesters [40]. These foams are made by the controlled entrapment of an expanding gas during the polymerization that forms urethane linkages between. polyethers or polyesters. The physical characteristics are largely determined by the selection of the polyether or polyester. Foams are produced that can be described as relatively firm to rather soft [41]. However in our application the wetting

behavior of the foam by the ceramic particle suspension is the most important property. It turned out that the polyester based polyurethane foams had the better wetting behavior compared to polyether based foams. This was evaluated experimentally.

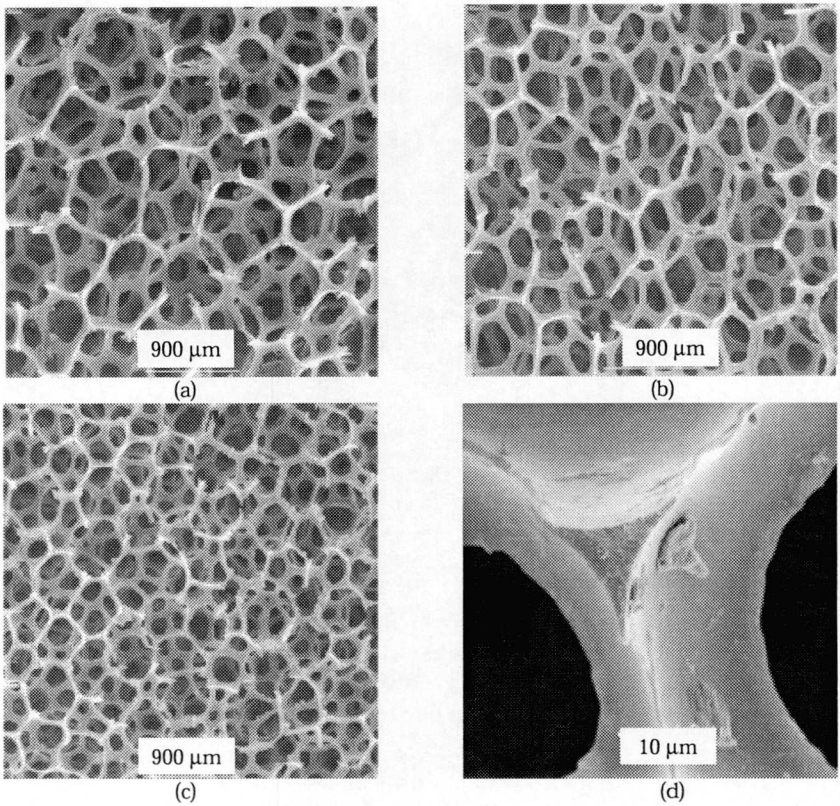

Fig. IV-2: Polyester based polyurethane foams,
(a) 45-ppi, (b) 60-ppi, (c) 80-ppi, (d): single strut.

Examples of the used polymer precursors are illustrated in Fig. IV-2. Fully reticulated polyester based polyurethane foams[1] with ppi-numbers of 30, 45, 60 and 80-ppi were used in this study. The foams were supplied in large plates 3, 5, and 8 mm

[1] Koepp AG, Oestrich-Winkel, Germany

in thickness and were cut to size by punching them out with a metal stamp to cylinders of 40, 45 or 50 mm diameter, respectively. Fig. IV-2d shows some "dirt" on the polymer struts. This remnant stems from the reticulation process in which the closed cells were opened by an oxy-hydrogen gas explosion or by the explosion of acetylene or propane [42].

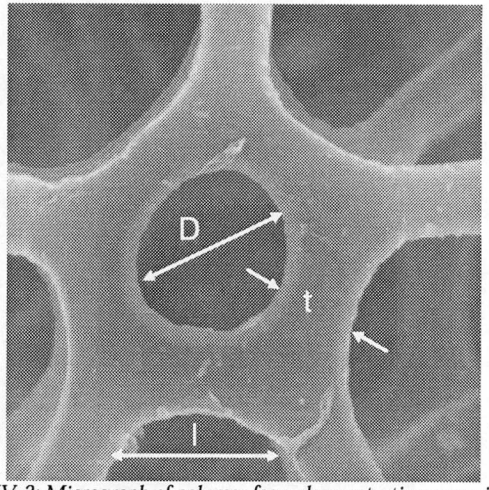

Fig. IV-3: Micrograph of polymer foam demonstrating pore size D, strut thickness t, and length l.

Due to the fact that the pores shown in the micrographs are two-dimensional projections of three-dimensional objects, their maximum diameter may not be represented in the image. The following equation was used to determine the maximum spherical diameter from an average number of circular segments of the cells [43]

$$D_{true} = \frac{D_{measured}}{0.616} \qquad \textit{Eq. IV-1}$$

The measurements of the strut lengths was also corrected by [44]

$$l_{true} = \frac{4}{\pi} l_{measured} \qquad \textit{Eq. IV-2}$$

The strut thickness was measured at the midpoints of the struts which were taken from a random selection and required no stereographic corrections. These measurements were made for each ppi-number and the results are given in Table IV-1. The pore size, the thickness of the struts, and the strut length decreased with increasing ppi-numbers.

ppi	PORE SIZE, *D* [mm]	STRUT THICKNESS, *t* [mm]	STRUT LENGTH, *l* [mm]
30	2.5	0.18	0.81
45	1.7	0.17	0.72
60	1.10	0.07	0.34
80	0.50	0.06	0.19

Table IV-1: Geometries of the polymer foams (numbers are averaged).

3.2.2 Ceramic Powders

A mixture of NiO and stabilized ceria was chosen for the anode and Lanthan-Strontium-Manganate (LSM) was used for the cathode.

POWDER	70 wt.% NiO/30wt%$Ce_{0.8}Gd_{0.2}O_3$ (Ni-CGO)	$La_{0.84}Sr_{0.16}Co_{0.02}MnO_{3-x}$ (LSM)
Supplier	Praxair, USA	Rhône Poulenc, USA
Lot #	03P2249FA	MBK M7-A*-95
Grain Size, d_{50}	0.75 µm	0.79
BET surface	9.3 m^2/g	5.2
Theor. Density	6.8 g/cm^3	6.5

Table IV-2: Ceramic Powders (Ni-CGO and LSM).

3.3 Ceramic Suspensions

Requirements for the suspension used in the polymer sponge method are as follows:

1. Ceramic powders have to be mixed with appropriate additives to make a slurry with a shear-thinning characteristic. The slurry must be fluid enough to enter, fill, and uniformly coat the sponge and subsequently regain enough viscosity under static conditions to remain in the sponge (thixotropy).
2. The suspension must wet the polymer sponge which requires a hydrophilic surface of the polymer in case of water based suspensions.

3.3.1 Anodic Porous Foams

The anodic foam will be the load-bearing structure, whereas a ceramic tape on this foam represents the active anode of the SOFC. These two components are processed separately and joined together after preparation but before sintering (chapter IV-5). For compatibility reasons and sinter adjustments of these two components the suspension of the anodic foam was prepared using almost the same recipe as that of the tape. Tapes produced from Ni-CGO powder based on the organic formula shown in Table IV-3, were brittle and cracked during drying. Several at-

tempts were made to solve this problem by varying the constituent of the organics. Different dispersants and other changes of the recipe in regards dispersant/plasticizer ratios did not improve the situation. A successful tape production was only possible with the addition of 16 wt.% of stabilized cubic zirconia (refer to the amount of Ni-CGO). The properties of the zirconia, such as median grain size and BET surface, are given in Table IV-4.

MATERIAL	wt.%	FUNCTION	SUPPLIER
60 g Ni-CGO	62.7	Powder	Praxair Speciality Ceramics, USA
23 ml Toluene	19.2	Solvent	F.E.R.O.S.A. E-Barcelona
1.8 g Beycostat	1.9	Dispersant	CeCa SA., F-Paris
5.2 g Polyethylenglycol 600	5.4	Plasticizer	Fluka Chemie, CH-Buchs
4.5 g Bis(2-ethylhexyl)phtalate	4.7	Plasticizer	Fluka Chemie, CH-Buchs
5.8 g Polyvinylbutyral (PVB)	6.06	Binder	Hoechst-Chemie, D-Frankfurt,

Table IV-3: Slurry composition of the anode ceramic foams.

POWDER	ZrO_2 (ss) 8 mole%
Supplier	Tosoh, Japan
Median Grain Size, d_{50}	0.23 µm
BET surface	16 m^2/g

Table IV-4: Zirconia Powder.

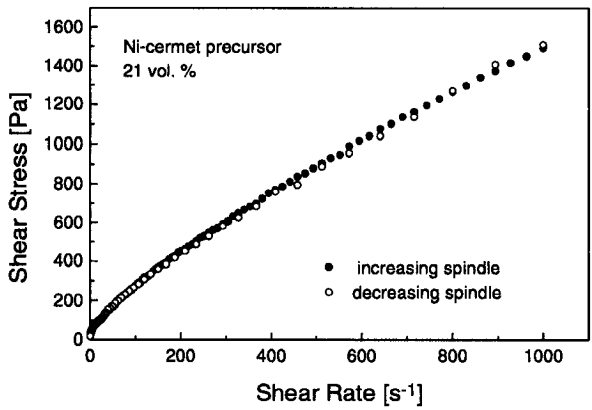

Fig. IV-4: Viscosity of a Ni-cermet precursor slurry.

Possible explanations for the favorable effect of the zirconia particles can be found in Appendix 1. Materials produced from the mixture of Ni-CGO/ZrO_2 will from now on be referred as ni-cermet precursors[2]. A typical way of slurry preparation is to mix of the two ceramic powders with toluene and dispersant, ball-milling with zirconia balls in a polyethylene bottle, and adding plasticizers and binder. The slurry was measured in a viscometer[3] to ensure the desired thixotropic behavior. Fig. IV-4 shows that data which illustrate the shear-thinning behavior of the slurry. Almost no thixotropic behavior could be measured.

3.3.2 Cathodic Porous Structures

These slurries are based on water as dispersant medium and stabilized using the anodic dispersant Sokolan CP 10. The pH is adjusted to between 9 and 11 according to the ESA measurements shown in Fig. IV-5.

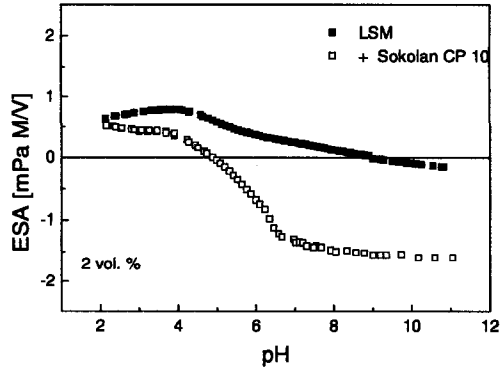

Fig. IV-5: ESA plot of a LSM slurry. The surface charge is increased with the addition of the dispersant. The IEP shifts from 9 to 5.5.

At these high pH values the surface charge of the LSM particles were highest. The slurry was prepared by adjusting the pH with KOH, adding the dispersant agent and the powder with subsequent ball milling. The slurry contained 42 vol. % LSM (Table IV-5). Fig. IV-6 shows the viscosity data which illustrates the shear-thinning behavior of the slurry with a slight thixotropic behavior. Fig. IV-7 demonstrates the viscosity of a slurry with 42.2 vol. % solids LSM in comparison to a suspension with 42.6 vol. % solids. Although the solid content is only slightly higher the shear thickening started at a shear rate of about 700 s^{-1}.

---

[2] Ni cermet precursor: mixture of Ni-oxide and oxide ceramics before reduction to the true Ni-cermet

[3] Contravers, Zurich, Switzerland

MATERIAL	FUNCTION	SUPPLIER
70 g LSM (9.3 m^2/g)	Ceramic Powder	Rhône Poulence, USA
14.6 g Water	Dispersion Medium	
0.05 g KOH 10 mol/l	Adjustment of pH	
1.0 g Sokolan CP 10	Anionic Dispersant	BASF, D-Ludwigshafen,
0.1g Octanol	Lowering the surface tension	Fluka Chemie, CH-Buchs,
0.55 g Dispex	Binder	Wacker Chemie,CH-Liestal

Table IV-5: Slurry composition of the porous cathode structures.

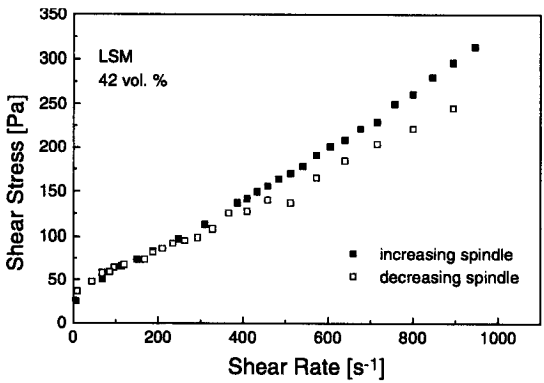

Fig. IV-6: Viscosity of the LSM slurry showing slight thixotropy.

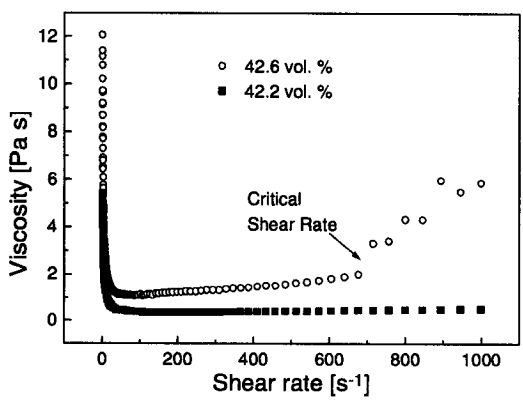

Fig. IV-7: Viscosity of a LSM slurry with two solids loading, showing shear thickening for higher solids loading at high shear rates.

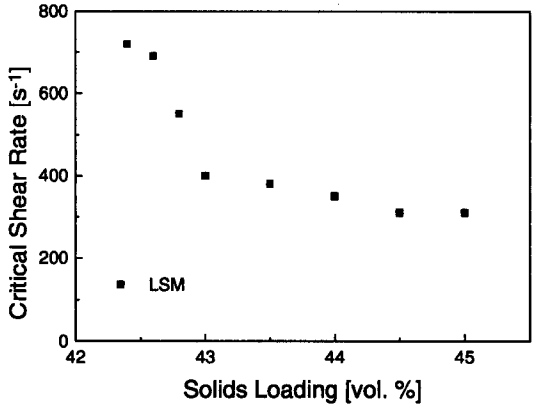

Fig. IV-8: Critical shear rate for the onset of shear thickening versus phase volume of dispersed LSM.

As illustrated in Fig. IV-8 the critical shear rate, above which the viscosity starts to increase, decreases rapidly with increasing solids content. One explanation of this behavior is given by Shaw [45]: Shear thickening occurs particularly in suspensions of densely packed particles in which there is only sufficient liquid to fill the voids. As the shear rate is increasing, this dense packing brokes down to permit the particles to flow past one another. The resulting expansion leaves insufficient liquid to fill the voids and is opposed by surface tension forces. Barnes [46] postulated that the increase in viscosity is due to the transition from a two-dimensional layered arrangement of particles to a random three-dimensional form. The severity of the shear thickening depends on the solids loading, in proportion to some maximum packing fraction which is itself partly controlled by the particle size and the form of the particle size distribution.

3.4 Shaping Process

3.4.1 General Procedure

As described in chapter IV-3.1 the polymer foams are dipped into the ceramic suspensions. Due to the swelling of the polymer caused by the reaction with the toluene based suspensions the polymer foams were moistened with toluene before infiltrating with the suspension. The foams swelled up to 15% of their original siz but regained their original size after drying. Due to these large dimensional changes drying was performed very slowly. In order to improve homogeneity and cababil-

ity to reproduce the experiment the infiltrated foams were passed through a set of rotating rollers in order to remove the excess slurry. The roller unit featured adjustable separation between the rolls. The optimum roller separation was determined by experiment and corresponds to about 15-20% of the thickness of the sample, or to 80-85 % compression. Care had to be taken to prevent individual cells from retaining any slurry. This was most difficult to achieve for the polymer substrates with the highest ppi-number. After passing through the rollers, the samples were placed onto a porous ceramic plate, covered with a glass-beaker, and dried at room temperature for at least 18 hrs.

Thermal analysis (Fig. IV-9) was performed in flowing air on finely cut particles of the polyurethane foam and coated material. The polymer foam material exhibits both thermoplastic and thermoset characteristics. Upon heating partial decomposition occured resulting in vaporization as well as formation of a thick, tar-like melt. The "melting point" was found to be approximately 260 ℃ (Fig. IV-9). Only some permeation permeation of the liquid decomposition products into the porous ceramic coating was expected. In the Poiseuille equation, the flow rate is inversely proportional to the liquid viscosity, and since the melt has a high viscosity, the flow rate should be low. The liquid is therefore expected to remain inside the strut until further decomposition occurs. This effect can be clearly demonstrated by thermal analysis of the ceramic coated polymer. As illustrated in Fig. IV-9 the decomposition starts at a temperature of 260 ℃ for the uncoated sample. Although it is superimposed by the peak of the binder/plasticizer decomposition, the decomposition of the polymer is clearly delayed for the coated polymer.

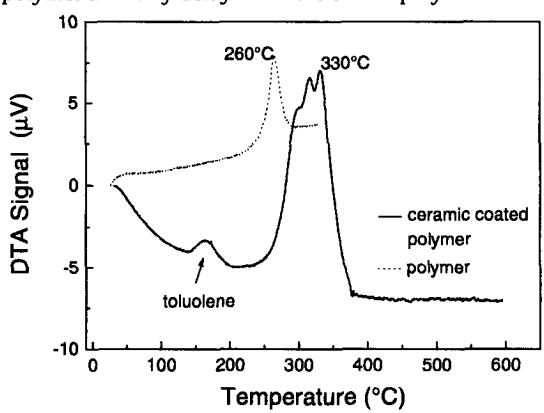

Fig. IV-9: DTA measurement of a polymer and a green Ni-cermet precursor foam. The decomposition of the pure polymer mainly takes place at 260 ℃ whereas it is shifted to 330 ℃ when covered with ceramic. The first peak at about 150 ℃ is due to the decomposition of toluene.

Based on the results of the thermal analysis, the heating schedule for the burnout of the polymer was chosen as follows:

- slowly heating to 450 °C with 0.5 K/min
- one hour holding time at 450 °C
- heating to 1110 °C with 3 K/min
- cooling to room temperature with 5 K/min.

During the first heat treatment, the polymer foam and other organics were removed from the coated foam samples by pyrolysis in air.

3.4.2 Strut Thickness

The thickness of the single struts is a crucial characteristic determining to a large extent the final strength of the ceramic foam. There are several possibilities to increase the strut thickness using the polymer sponge technique:

1. increase of the solid content of the suspension
2. increase of the thixotropy of the suspension
3. multiple coating of the green or the sintered foam
4. impregnation of the sintered foam with a salt solution and transformation to ceramic
5. etching of the polymer foam with chemicals to remove the thin edges of the struts thereby avoiding concentration of stress center in the ceramic
6. heating the polymer foam to soften its contours.

- *Solids Content of the Suspension*

The easiest way to increase the thickness of the struts is to coat the polymer with a suspension with a higher solids content. By doing so the density of the green stage will be decreased, the drying time shortened, and the shrinkage minimized. Unfortunately, the viscosity of both our suspensions changed with increasing solid contents to a shear thickening behavior (see Fig. IV-7) which is very undesirable as it hinders a successful coating of the polymer.

- *Thixotropic Behavior of the Suspension*

The addition of montmorillonite, bentonite or graphite is often described in the literature to achieve the desired thixotropic behavior [47]. A „house-of-card"-structure of e.g. bentonite is responsible for the thixotropic behavior. However, the addition of these substances to our suspension only shifted the viscosity to higher values, but did not change the time dependent behavior of the slurry. It was assumed, that the dispersant also reacts with the Na^+ which sits on the surface of these substances thus preventing the house-of-card-structure.
Another common approach is the use of organic molecules with high molecular weight. Although, the addition of glycerin and/or ethylene [48] did change the vis-

cosity of the LSM-slurry, the resulting green body was very brittle. The combination of polyvinylalcohol as binder with glycerin as plasticizer showed the best results concerning the slurry viscosity. The addition of colloidal silica is widely known in food industry. Ice-cream and tomato-ketchup are examples of that practice. However, upon firing, silica can melt to a glassy phase which alters the properties of the structure. Due to the application of the foams as current collectors such additive have not been used.

- *Second Coating*

The second coating is more difficult to apply since the foam cannot be compressed after drying. Therefore, the slurry must be sufficiently thin to allow drainage by gravity. If the slurry is too thin, however, dissolution of the previously deposited green ceramic coating may occur. Hence, re-coating of sintered LSM foams were performed. The foams were dipped into a diluted LSM-suspension (10 vol. %), air was blown through it to open the closed cell faces and the coated foams were then placed onto a metal net and dried for 12 hrs. Sintering was performed at 1350 ℃ with a heating rate of 3 K/min. Fig. IV-10 demonstrates the resulting microstructure with a large number of closed pores. However, the thickness of the struts has not increased considerably.

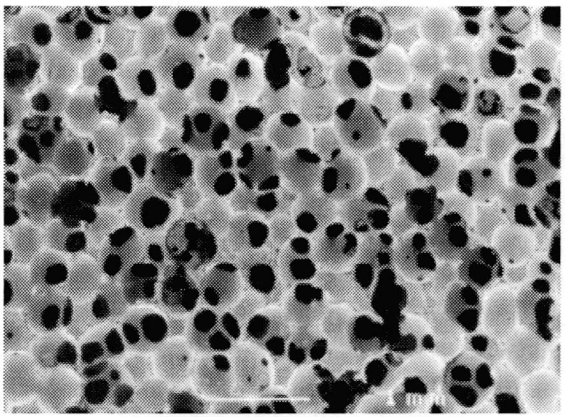

Fig. IV-10: Micrograph of re-coated sintered LSM foam; the foam is characterized by a large amount of closed pores.

- *Impregnation with Salt Solution*

A solution containing the required salt-ions e.g. nitrates could be used to impregnate the sintered foam. During heating the nitrates change to oxides and form the appropriate ceramic. Therefore, the salt solution could "heal" some defects by filling up microcracks and strut voids.

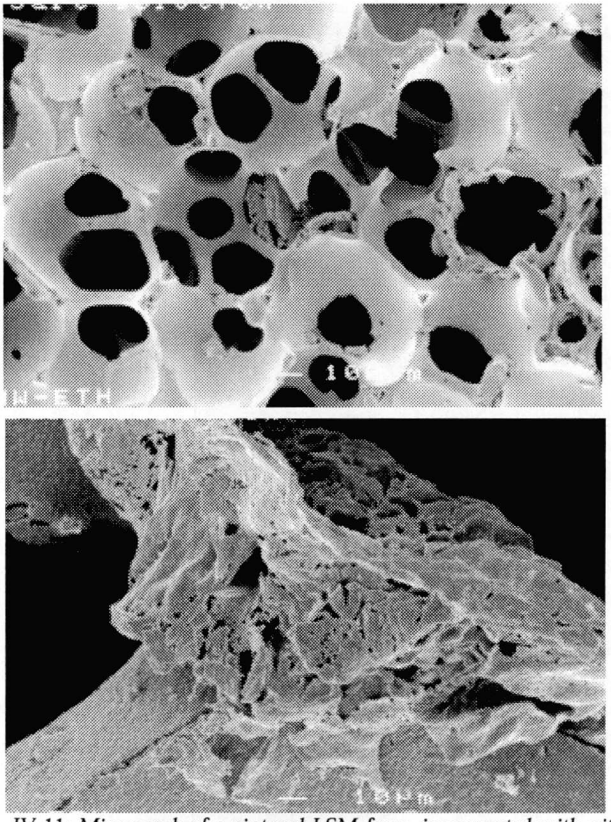

Fig. IV-11: Micrograph of a sintered LSM foam, impregnated with nitrates solution of the elements after heating tot 1000 ℃. The precipitated LSM form large agglomerates with sizes up to 500 μm in certain regions.

For the LSM foams, stoichiometric amounts of the nitrates[4] were desolved in 50 ml water, the sintered foams impregnated with this solution, and dried at room temperature. The foams were then heated up to 1000 ℃ and XRD measurements econfirmed the total transformation of the nitrates to LSM. However, the LSM precipitated from the nitrate solution was not uniformly distributed over the structure of the foam as shown Fig. IV-11. Agglomerates were found in certain regions forming very fissured structures. Microcracks and other defects were not filled because the

[4] (52.1 g $LaNO_3$*6 H_2O, 4.87 g $Sr(NO_3)_2$, 35.27 g $Mn(NO_3)_2$*4 H_2O and 0.83 g $Co(NO_3)_2$* 6 H_2O)

agglomerates with sizes up to 500 µm were deposited on top of the substrate. Therefore, this method was not pursued any further.

- *Etching of the Polymer*

Etching was performed by dipping the polymer foams in different chemical solutions. The foams were examined before and after the etching process under the microscope. Acetone caused the struts to swell. Submersion in concentrated sodium hydroxide or hydrochloric acid degraded the struts to threadlike filaments. Shorter submersion times showed that the shape of the cross section did not change although significant removal of material occurred.

- *Heating of the Polymer*

The polymer foams were carefully heated to 150-250 ℃. Unfortunately, this resulted in permanent bending of the struts and densification of the foam structure rather than changing the strut cross section. Also, the softening did not occur uniformly across all the regions of the sponge.

The methods used so far, did not show the desired effect. The most promising way to increase the strut thickness is probably adjusting the ceramic suspension to achieve a thixotropic behavior. However, in such cases, many experiments with different kinds and amounts of ceramic powders, plasticizer, and binders have to be performed. In this study, however, only a few of such experiments were undertaken due to the high price and lack of availability of the powder (one gram of each powder costs 1$. For each experiment at least 30 g powder is necessary).

3.5 Pyrolysis Process

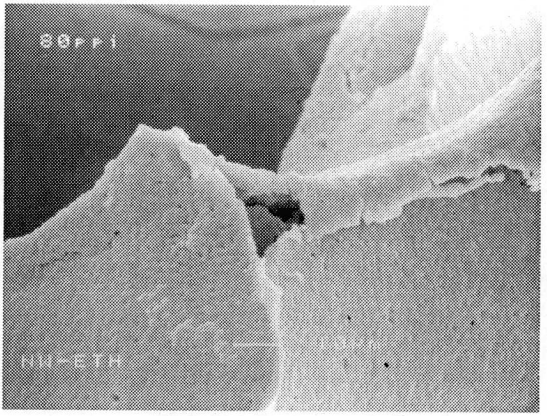

Fig. IV-12: Thermally etched markings of cracks.

After drying the impregnated foams were heated to pyrolyze the polymer and to sinter the ceramic. After the pyrolysis and after sintering cracks could be observed in the microstructure. Some fracture surfaces of the strut cracks in the sintered foam showed a thermally etched appearance (Fig. IV-12), suggesting that they had been formed already before sintering took place. It was assumed that the crack formation started ruing the pyrolysis process, when the plastic foam substrate is converted to gaseous products. If the gas cannot escape fast enough, pressure will build up inside the hollow strut causing fracture. The effect of the heating rate was demonstrated by varying it from 1 K/min, 0.7/min to 0.5 K/min. In Fig. IV-13 samples are shown after the sintering procedure. Quick burnout-times resulted in many longitudinal cracks of the struts (Fig. IV-13a,b), whereas with a slow heating ramp (Fig. IV-13c) the foams demonstrated an unbroken microstructure.

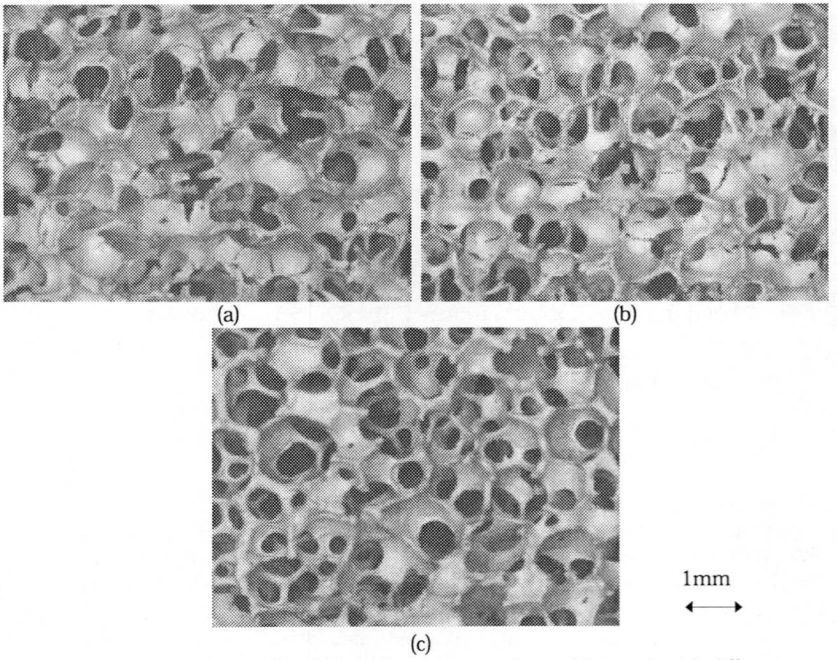

Fig. IV-13: Micrographs of Ni-cermet precursor foams fabricated with different burnout-time,
(a) 1 K/min, (b) 0.7 K/min, (c) 0.5 K/min. After the burnout procedure the samples were sintered to 1400 ℃. Cracks are visible in samples processed at high heating rates.

In the following section it will be shown, that these cracks may also be due to the expansion of the polymer foam. Some calculations to find an explanation why and when these cracks occur. First, it will be calculated which pressure is necessary to break the green ceramic coating. Then, this pressure is compared to the pressure caused by the escape of the pyrolysis gases. The drying stress and the stress caused by the thermal expansion of the polymer can also be estimated and compared to the stress necessary to fracture.

3.5.1 Pressure Required to Damage Struts

The flaws that lead to strut cracks are probable regions where the ceramic coating at the protruding triangular edges of the struts is very thin.

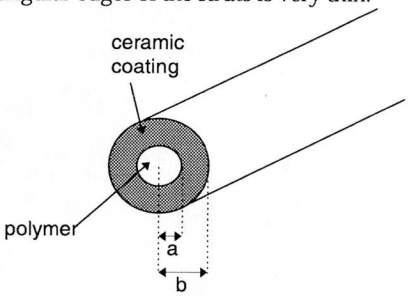

Fig. IV-14: Simple model of a single strut.

By a simple calculation the critical pressure inside the strut that would be required to break the ceramic coating was estimated. The strut was considered to be a thick wall pressure vessel as shown in Fig. IV-14. For this vessel, the critical internal pressure P_{crit} to cause fracture is [49]

$$P_{crit} = \sigma_f \left(\frac{b^2 - a^2}{b^2 + a^2} \right) \qquad \text{Eq. IV-3}$$

where a and b are the inner and outer radii and σ_f is the fracture strength of the ceramic coating. (A synopsis of the constants and numbers used in the following equations is given in Table IV-6). The polymer strut diameter was estimated from the diameter of a cylindrical strut with a cross-sectional area equal to that of the actual triangular strut. This equivalent diameter is about 70 µm (a = 35 µm). A minimum coating thickness of 10 µm was assumed, since fracture will occur at the thinnest coated areas; hence b = 45 µm. The green strength σ_f was estimated to be in the range of 1 to 10 MPa [50]. By using Eq. IV-3 the internal pressure to produce these stresses was calculated to be P_{crit} = 0.24-2.4 MPa.

3.5.2 Gas Flow Rate

The radial gas flow rate (Q) out of a cylinder was used [51]:

$$Q = \frac{\pi K l \cdot \rho_0 \Delta P}{\mu \ln(b/a)} \qquad \textit{Eq. IV-4}$$

K is the permeability, l is the length, ρ_0 is the gas density, ΔP the internal pressure above atmospheric pressure, μ the gas viscosity, and a, b as explained above.
The length of a strut was estimated to be 0.001 m. The viscosity μ and the density ρ_0 of the gas can be estimated[5] to have values of $\mu = 4.7 \cdot 10^{-3}$ Pa·s and $\rho_0 = 9.47 \cdot$ g/cm^3. Reed [53] and Brown [36] estimated $K = 1.1 \cdot 10^{-9}$ m^2 for green porous ceramics. An average coating thickness of 40 µm was chosen; therefore $b = 75$ µm. Using the above calculated minimum value P_{crit} for $\Delta P = 0.24$ MPa and $a = 35$ µm, the minimum Q value obtained is $6.65 \cdot 10^{-8}$ kg/s or 1100 mg/min. A comparison with thermogravimetric data of Fig. IV-15 shows that the weight loss rate was much lower.

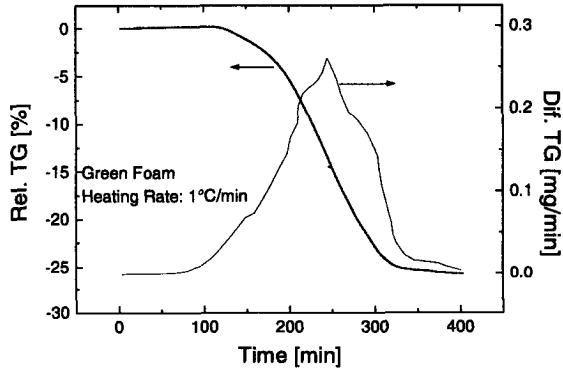

Fig. IV-15: Thermogravimetric analysis of a Ni-cermet precursor foam.

Thus, the pyrolysis gases should escape at pressures less than those that lead to strut damage. Therefore, some other damage mechanisms must also be producing high stress levels in the coating.

3.5.3 Pressure Caused by Drying Stress

When the coated foam sample dries, the green ceramic coating shrinks linearly about 0.6%. This is an estimated value resulting from measurements on slip cast samples using the same suspension. Since the polymer foam substrate does not shrink, stresses will be generated in the ceramic coating. However, because the

[5] The polymer foam oxidized to form carbon dioxide, nitrogen, and water. The viscosity was calculated for this gas mix [52]. The density was calculated using the general gas equation and an assumed molecular weight of 34.46 g/mole for the gas mixture.

Young's modulus of the polyurethane is very low, about 0.0045 GPa, it should offer little resistance to the shrinkage of the coating, preventing the generation of high stresses. To calculate these stresses the following approach was used [36]:
The ceramic coating can be considered as a hollow ceramic cylinder that experiences a shrinkage of 0.6% upon drying. There would be no stresses if the polymer will not be present. Now consider inserting the polymer cylinder into the already shrunk ceramic cylinder. The compressed polymer cylinder causes a „contact pressure" which can be calculated. The displacement at the inner surface of the ceramic cylinder, Δ_c, is given by [49]

$$\Delta_c = \frac{P_{cont} \cdot a}{E_c}\left(\nu_c + \frac{b^2 + a^2}{b^2 - a^2}\right) \qquad \textit{Eq. IV-5}$$

where P_{cont} is the contact pressure, E_c the Young's modulus, and υ_c the Poisson's ratio of the ceramic.

For the polymer cylinder, which experiences an external pressure, the displacement, Δ_p, is given by

$$\Delta_p = \frac{P_{cont} \cdot a}{E_p}\left(1 - \nu_p\right) \qquad \textit{Eq. IV-6}$$

where E_p is the Young's modulus and υ_p the Poisson's ratio of the polymer.
The total displacement Δ is given as

$$\Delta = \Delta_c + \Delta_p = P_{cont}\, a\left[\frac{1}{E_c}\left(\nu_c + \frac{b^2 + a^2}{b^2 - a^2}\right) + \frac{1}{E_p}\left(1 - \nu_p\right)\right] \qquad \textit{Eq. IV-7}$$

Hence, the contact pressure P_{cont} can be written as

$$P_{cont} = \frac{\Delta}{a}\left[\frac{1}{E_c}\left(\nu_c + \frac{b^2 + a^2}{b^2 - a^2}\right) + \frac{1}{E_p}\left(1 - \nu_p\right)\right]^{-1} \qquad \textit{Eq. IV-8}$$

By substitution of the appropriate values a = 35 µm, b = 75 µm, E_c = 11.6 GPa [54], E_p = 0.045 GPa [55], ν_c = 0.14 [54], ν_p = 0.2 [55] and the total displacement Δ = 0.006 · 75 µm, a contact pressure P_{cont} = 0.35 MPa can be calculated.
The internal stress within the ceramics was calculated using Eq. IV-4 with P_{cont} = 0.35 MPa, a = 75 µm and b = 75 µm. A stress of 0.54 MPa was the result. As mentioned above the green strength of the coating is expected to be at least 1 MPa, but not higher than 10 MPa [56]. Therefore, the calculated stress is not sufficient to cause cracking. However, this calculation does not consider that the outside of the coating dries faster than the inside. The outside of the coating could shrink but will be constrained by the still undried inner region of the coating, raising the stress

levels. This effect which could be for the stress fractures should be minimized by careful slow drying of the foams.

3.5.4 Pressure Caused by Substrate Thermal Expansion

Cracking may also occur due to thermal expansion differences between the polymer and ceramic coating at relatively low temperatures. Since the polymer has a higher expansion than the ceramic coating, this could lead to crack formation below the pyrolysis temperature range. This assumption was tested by thermal stress calculations. Thermal strains can be estimated for the temperature ranges discussed above. The expansion coefficient α is $13.5 \cdot 10^{-6}$/K for the LSM-foams and $100 \cdot 10^{-6}$/K for poly-urethane. The thermal strain between 25-330 °C is $\Delta\varepsilon = \Delta\alpha \cdot \Delta T = 86.5 \cdot 10^{-6}\,K^{-1} \cdot 305\ K = 0.026$. The thermal expansion stress was calculated using the same method as for the drying stress (Eq. IV-8). This gives a tangential stress of 8.1 MPa, which is sufficient to cause cracking. Moreover, as the thermal expansion coefficient of polyurethane is expected to increase as the temperature approaches the melting point, the stress should be even higher than estimated.

P_{crit}: internal critical [Pa] = 0.24-2.4·10^6 Pa (calcul. in Eq. IV-2)	ΔP: internal pressure above atmospheric pressure [Pa] ≡ P_{crit} = 0.24·10^6 Pa
σ_f: fracture strength of ceramic coating = 1-10·10^6 Pa [56]	μ: gas viscosity [Pa·s] = 4.7·10^{-7} [Pa·s] (estimated)
a: inner radius of strut [m] (Fig. IV-14) = 35·10^{-9} m (estimated)	Δ: displacement [m] = 0.45·10^{-9} m (calculated)
b: outer radius of strut [m] (Fig. IV-14) = 45·10^{-9} m (estimated)	P_{cont}: contact pressure [Pa] = 0.35·10^6 Pa (calcul. in Eq. IV-8)
Q: radial gas flow rate [kg/s] = 6.65·10^{-8} kg/s (calcul. in Eq. IV-8)	E_c: Young's modulus of the ceramic [Pa] = 11.6·10^9 Pa [57]
l: strut length [m] = 0.001 m (estimated)	E_p: Young's modulus of the polymer = 4.5·10^6 Pa [55]
K: gas permeability [m^2] = 1.1·10^{-9} m^2 [36, 53]	υ_c: Poisson's ratio of the ceramic = 0.12 [57]
ρ_o: gas density [kg/m^3] = 9.47·10^{-3} kg/m^3 [52]	υ_p: Poisson's ratio of the polymer = 0.35 [58]

Table IV-6: Synopsis of the used numbers in Eq. 3-8.

To summarize this section: the cracks which appeared after the pryolysis step are not only due to the pressure caused by the escaping gases but moreover caused by the thermal expansion mismatch of the polymer and the ceramic. An approach to overcome the cracking problem would be to increase the coating thickness relative

to the polymer strut radius or to reduce the strut edges, where the coating is most susceptible to cracking. It is apparent that the pronounced triangular cross section of the polymer foam struts is responsible for the strength limiting flaws in the ceramic struts of the foam. Therefore any process that could make the strut cross section less angular would help to overcome this problem.

3.6 Sintering Process

Expansion measurements using a differential dilatometer[6] were performed in order to establish the optimum sintering program. Foam samples in the green state were pre-sintered at 700 °C. This was necessary to give the foam some mechanical strength before the measurement. The length change during heating in air was measured in reference to a sapphire single crystal.

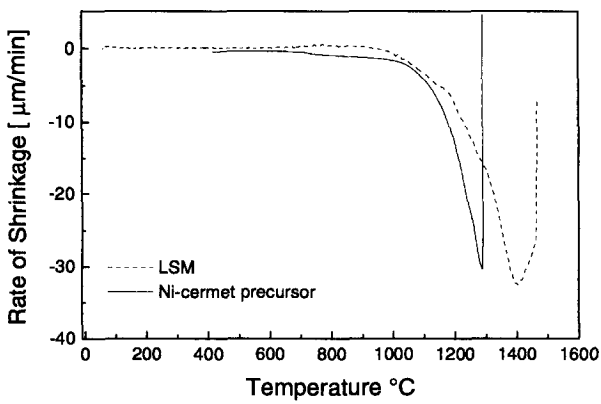

Fig. IV-16: Sintering behavior of the two foams. The foams were pre-sintered at 700 °C. The linear shrinkage was about 30%.

The relative length change for both samples is given in Fig. IV-16. For both structures sintering started at 1000 °C. The Ni-cermet precursor foam was sintered at lower temperatures than the LSM sample. The following sinter program was chosen according to these measurements:

- burnout with ¼ K/min to 400 °C (chapter IV-3.4.1)
- further heating with 1 K/min up to 1100 °C
- holding time 1 hour
- transfer to the sinter furnace

[6] Baehr Thermoanalysis, Dil 802 S, Germany

- rapid heating with a heating ramp of 5 K/min to 1050 °C
- further heating with 2 K/min to 1400 °C and 1450 °C for Ni-cermet precursor and LSM, respectively
- 1 hour holding-time
- cooling with 4 K/min to room temperature.

4 Properties of Sintered Ceramic Foams

In this chapter, the density, micro- and macrostructure, compressive strength, electrical conductivity and gas permeability of ceramic foams are reported.
The aim of this work was to study the compressive behavior of Ni-cermet precursor and LSM foams with regard to their application as load-bearing structures in solid oxide fuel cells. The foams must have sufficient strength to allow handling and bearing the load applied to them. The "handling" property cannot be specified by a single measurable number but must be judged subjectively. In the Siemens cell design they must bear a weight of up to 400 g/cm^2 [59] whereas the Sulzer design requires a loading capacity up to 120 g/cm^2 [60]. With regard to the use as current collectors and air distributors, the electrical conductivity and the gas permeability of the foams should be as high as possible.

4.1 Density, Micro- and Macrostructure

Density
The most important property governing the behavior of ceramic foams is the relative density ρ_{rel} [55]i.e. the density of the bulk foam normalized by the theoretical density of the solid that forms the cell edges and faces.
The relative densities of ceramic foams usually range from 0.003 to 0.30. In this project foams were processed with relative densities from 0.05 to 0.30. The loss of the cellular makes it difficult to identify a repeating unit cell structure For relative densities over 0.30. For these densities, the material is better considered as a solid containing isolated pores or fine interconnected porosity.
It is intuitively evident that increasing porosity will reduce elastic moduli and strength. Theoretical models describing the mechanical behavior of foams usually relate the elastic modulus and fracture strength to the relative density [57, 61, 62]. Properties other than mechanical are also influenced by density or porosity. Thermal conductivity increases with relative density whereas the creep rate decreases substantially with increasing relative density. The electrical conductivity is especially sensitive to the degree to which phases are connected. Ceramic foams processed via the polymer sponge method possess a percolative network. Therefore the electrical conductivity is almost constant for all densities beyond the percolation

threshold density. The relative density was measured for all specimens prior to any mechanical or electrical tests. The theoretical density of the Ni-cermet precursor foams was derived by applying the rule of mixtures to the weight fractions of the major phases in the material and was calculated to 6.7 g/cm^3 (NiO : $Ce_{0.8}Gd_{0.2}O_3$: ZrO_2= 60 : 25.7 : 14.3 wt.%)[7]. The theoretical density of the LSM-material was 6.5 g/cm^3. The density of the foams was calculated from their mass and volume.

Microstructure

The average grain size of the Ni-cermet precursor material was 0.3 μm whereas the LSM material exhibit a grain size of 1 μm (Fig. IV-17).

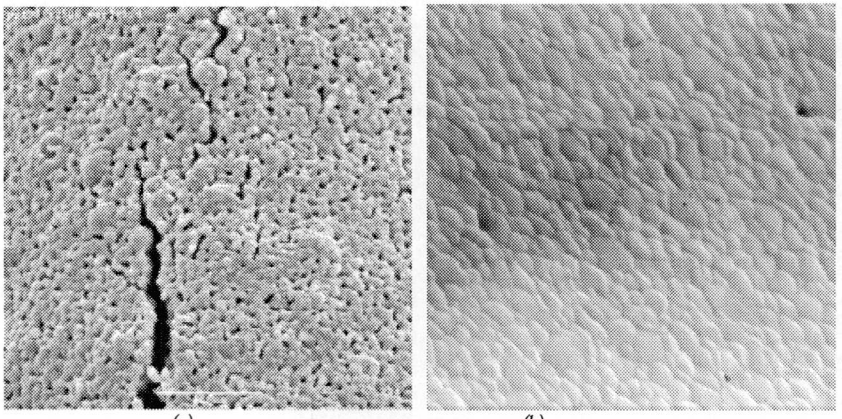

(a) *(b)*

Fig. IV-17: Microstructure of sintered foams
(a) Ni-cermet precursor (with additional cracks) scale 11 μm,
(b)) LSM, scale 11 μm.

In ceramic foams two types of porosity are found: a large triangular pore in the center of the struts and a fine-scale porosity within the solid portion. The volume of the fine porosity within the strut wall was determined using mercury porosimetry[8]. The sintered foam samples were broken up into individual struts in order to expose the large central holes allowing them to fill easily with mercury. The tests were run to a maximum pressure of 2 kbar. Knowing the dimensions of the single struts (Table IV-7) and their weight, the volume of the strut voids could be calculated. This volume was subtracted from the total amount of mercury giving the volume

[7] Theoretical Density NiO: 6.67 g/cm^3, CeO_2: 7.41 g/cm^3, ZrO_2: 5.98 g/cm^3 [52]

[8] Porosimeter 2000 Series, Carlo Erba Instruments, USA

of strut wall porosity. The Ni-cermet precursor foams had a strut wall porosity of 10 vol. %, while the LSM foams had 2 vol. %. The average pore size was 250 nm for the Ni-cermet precursor foams and 95 nm for the LSM foams. As shown in the microstructure (Fig. IV-17) the major porosity within the strut wall was located between the ceramic grains.

Macrostructure

The macrostructure of the sintered LSM foam is shown in Fig. IV-18.

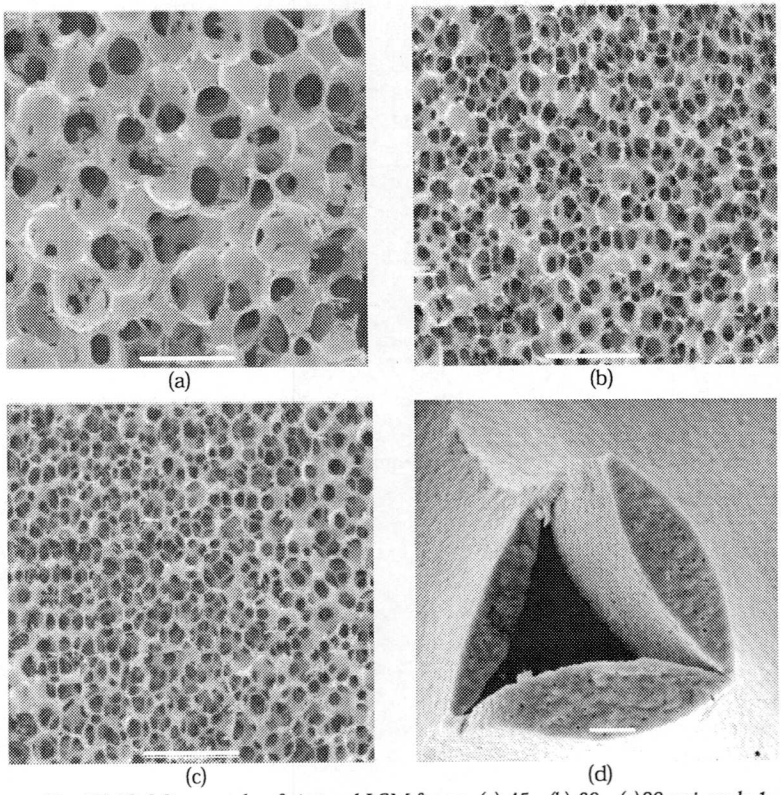

Fig. IV-18: Micrographs of sintered LSM foams, (a) 45-, (b) 60-, (c)80-ppi, scale 1 mm, (d) single strut, triangular void results from polymer removal, scale 10 µm.

The foams are characterized by a fully open structure for all ppi-numbers, although a certain number of closed cells is always present. These closed cells are

mainly broken ones in the 45-ppi foams whereas they are intact in the 80-ppi foams.
The ppi-number of the sintered foam is slightly higher than that of the original polymer substrate due to the shrinkage during sintering. However, the ppi-numbers given in Table IV-7 refer to the ppi value of the polymer substrates (this study will adhere to this value).

PPI	REL. DENSITY	STRUT THICKNESS [mm]	STRUT LENGTH [mm]
60	0.12	0.16±0.04	0.46±0.09
60	0.18	0.13±0.03	0.31±0.08
60	0.18	0.15±0.05	0.35±0.11
80	0.15	0.09±0.02	0.18±0.04
80	0.14	0.07±0.04	0.16±0.04
80	0.21	0.10±0.03	0.21±0.09
80	0.27	0.14±0.04	0.26±0.10

Table IV-7: Geometrical measurements of the sintered foams, values are given as averaged numbers with their standard deviations.

One approach commonly used to describe the relationships between the parameters of the foam and the mechanical behavior involves the development of a micromechanical model. This implies the assumption of a unit cell geometry and the deformation mode within the struts. The failure of a single strut generally constitutes the failure of the unit cell and thereby of the bulk foam. It is assumed that the mechanical behavior of this unit cell is representative of the bulk structure.
Several theoretical models exist to predict the behavior of cellular materials [39, 63-66]. One simple model describing the mechanical behavior of cellular ceramic materials has been published by Gibson and Ashby [55]. The complications encountered in trying to identify a suitable unit cell that characterizes the complex macrostructure of real foams led them to consider a simple geometry for this unit cell as shown in Fig. IV-19. The open-cell foam is modeled as a cubic array of individual members of length l and thickness t. The cell walls are joined together so that loads cause bending moments on the cell walls. The mechanical analysis is substantially simplified by this cell geometry allowing the derivation of a general set of expressions for the mechanical behavior.
For ceramic foams, equations were applied for the elastic constants, tensile and compressive strengths, fracture toughness, hardness and thermal shock behavior [55]. One should realize however, that assigning a single unit cell to these complex macrostructures may be a big oversimplification.

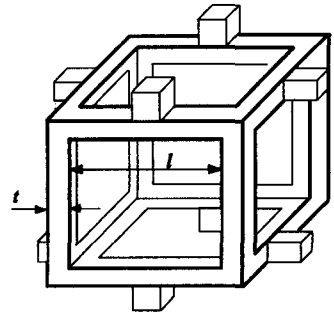

Fig. IV-19: Unit cell used by Gibson and Ashby to derive mechanical relationships for open-cell materials [55]. The open-cell foam is modeled as a cubic array of members of length l *and thickness* t. *Adjoining cells are staggered so that they connect at the mid-points of the edges.*

Gibson and Ashby [55] have shown that by using this unit cell the relative density of most three-dimensional cellular solids can be related to the macrostructure by the simple expressions:

$$\rho_{rel} = C_2\left(\frac{t}{l}\right)^2 \text{ (open cells)} \qquad \textit{Eq. IV-9}$$

$$\rho_{rel} = C_2\left(\frac{t}{l}\right) \text{ (closed cells)} \qquad \textit{Eq. IV-10}$$

for open and closed cell foams, respectively. These expressions should be accurate for relative densities less than 0.3. The parameters C_1 and C_2 are constants characterizing the cell geometry. Asby and Gibson derived 0.333 and 0.766 for C_1 and C_2. These equations suggest also that the struts become thicker and shorter at higher densities which is in conflict from our findings as will be shown later.

One way to check the agreement between the macrostructure of the real, open cell foams and the theoretical predictions is to plot the dependence of the density on the parameters of Eq. IV-10. The changes in the $(t/l)^2$ ratio of the LSM-foams are plotted in Fig. 22 along with values derived by Brezny [62]. The values of the strut length and thickness were taken from Table IV-7. For the alumina material the slope was calculated as $C_1 = 0.7$ whereas the value of the LSM material was $C_1 = 0.24$. For both cases the relationship of the strut length and thickness with the relative density could be demonstrated.

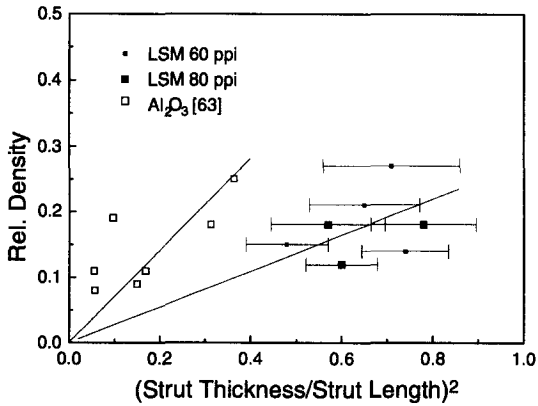

Fig. IV-20: Changes in the t/l ratio vs. relative density. The straight lines represent Eq. IV-9 with the constants C_1=0.7 *for the values derived by Brezny [62] for alumina foams and* C_1=0.27 *for the values derived for LSM foams.*

4.2 Compressive Strength and Creep

Porous ceramics suffer from relatively low strength particularly when they are made by the polymer sponge method. In this case, after the organic sponge is burned-off, very thin webs of ceramic structure may be left. Therefore, ceramic foams have a much lower strength than theoretically possible. The single struts of the foams are weak because of the holes left behind by the polymer burn-off process. References are available in the literature for fracture toughness [15, 34, 55, 62, 67-70] bending [71, 72], tensile [34, 68, 73], and the compressive strength [57, 62, 68-70, 73-76]. Less data is available on the Weibull statistics of ceramic foams [68, 77]. Aoki [72] reported 1.0 MPa for the compressive strength of SiC foams with densities of 0.12. Green [78] measured the compressive strength of open cell vitreous carbon and came up with a strength of 1 MPa for cell sizes of 0.49 mm. Goretta [71] measured the compressive strength of alumina foams as a function of density. The strength was 0.5 MPa for foams with a density of 0.1 and 1.1 MPa for foams with relative densities of 0.2. Brezny [62] measured 2.1±0.36 MPa for alumina-mullite foams with relative densities of 0.11 and 4.23±0.3 MPa for relative densities of 0.16. The company Hi-Tech Ceramics [79] reported on the compressive strength of cordierite, mullite, alumina, and zirconia foams. Strength values of 0.75-2.01 MPa were measured for 30-ppi foams with densities of about 0.15. Antiserov [76] studied the compressive strength of cellular porcelain and reported 1.7 - 2.0 MPa.

Only some data is available on the compressive testing and creep at higher temperatures of foams. Goretta [71] measured the compressive strengths of alumina foams at 800 - 1600 °C. The values were stable up to 1000 °C and then decreased substantially above 1200 °C. The decrease was explained by the onset of creep processes. The compressive strengths of SiC coated vitreous carbon foams were measured at 25, 1000, 1200 and 1400 °C by Wereszczak et al. [73]. No obvious trends were observed in their respective strengths as a function of temperature. The strengths were 3.6 MPa at room temperature and 2.8, 3.2 and 3.2 MPa at 1000, 1200 and 1400 °C respectively. The creep of zirconia foams used as heating element in electrical furnaces was investigated. The creep was due to recrystallization, which is sensitive to the tetragonal-cubic phase transition and to the stress.

It is interesting to note the similarity in the compressive strengths of different materials such as alumina, zirconia, mullite cordierite, and porcelain. It seems that the intrinsic material's strength is not the strength limiting property, but the geometrical arrangement of the cells in the ceramic foams is. This can be explained by the relationship of the porosity with the mechanical strength which was first proposed by Ryshkewitch [80]

$$S = S_0 \cdot \exp(-bp) \qquad \textit{Eq. IV-11}$$

where S is the strength of the porous material, S_0 is the zero-porosity strength, b is determined by the complexity of the pore structure, and p the volume fraction of pores. Thus, assuming the same pore structure for all the reported ceramic foams, the compressive strength is in the same order for all kinds of ceramic due to this exponential relationship.

4.2.1 Experimental Set-up

Compressive crushing tests were performed with an universal testing device[9]. A crosshead speed of 0.5 mm/min was used as recommended earlier [62, 73, 81]. The compression specimens were placed between two Si_3N_4-plates (5x5x0.3 cm^3).
A typical stress-strain curve of a LSM sample is shown in Fig. IV-21: In region 1 the specimen and loading fixture alignment takes place. Region 2 corresponds to the elastic region and can involve strut fracture, either in the contact region or internally. As a crack propagates through the cellular material it does so by fracturing individual struts. This can clearly be seen in region 2 where the fracture of single struts is connected with some load drops. At the collapse point (region 3), macroscopic cracks propagate with an associated load drop (region 4). In the foam mate-

[9] Instron Limited, United Kingdom

rials this corresponds to pieces of material breaking away from the sample. Additional deformation of the fractured material occurs in region 5 where the strain is independent of stress as the material is progressively crushed. The cross-sectional area of the sample and the failure load were used to calculate the fracture stress. The failure load was taken as the peak load after which the load carrying capacity of the specimen was severely reduced. The failure mode was associated with the catastrophic collapse of several layers of cells. The peak load occurred at almost the same values as reported in the literature. It seems that the specific foam's structure is responsible for the compressive strength, independent of the ceramic used.
One important feature for the application of a ceramic foam in a solid oxide fuel cell is that even if a crack occurs locally the foam can bear the load and is still electrically conducting.

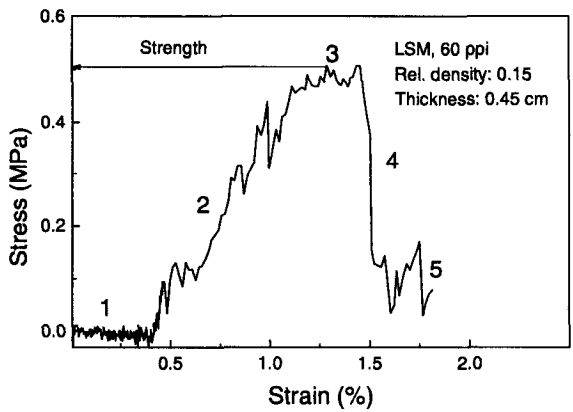

Fig. IV-21: Typical stress strain curve for a compressive test on ceramic foams. The numbers are explained in the text. The peak load was taken as the compressive strength of this specific foam.

Not all the experiments were performed on both foam materials. However, it was assumed that the general conclusions are mutually applicable.

Surface loading

Gibson and Ashby [55] have pointed out that the results of the indentation of a brittle foam with a hard flat punch depends strongly on the contact area, which they attributed to difficulty in uniformly loading the struts. Their analysis predicts that the probability of contacting a given fraction of struts decreases with an increasing indented area, resulting in the indentation strength being inversely proportional to the square root of the area. By using a buffer material at the punch sur-

face, the probability of contacting a strut goes to unity and one obtains the true crushing strength of the foam.

Several possibilities to reach this high contact area were tried:

- Grinding of the foam's surface to avoid the protrusion of single struts above the surface. The foams were polished on a manual grinding machine with grid 1000 grinding paper.
- Using a buffer alumina felt layer.
- Dipping the foam's surface in a low-viscous epoxy. The epoxy infiltrates the surface layer, thus achieving an improved distribution of the load over the entire surface.

Five sets of crushing experiments were performed:

- foams without any treatment
- foams with ground surface
- foams with an alumina felt placed between sample surface and the push rods of the testing machine
- foams with ground surfaces with an alumina felt placed between sample surface and the push rods
- foams with ground surfaces with epoxy infiltrated cells at the contact surface.

All the different samples were sandwiched between two Si_3N_4-plates. For each of the experiments eight 60-ppi LSM foams with a relative density of 0.15 were used. The experimental data are plotted in Fig. IV-22. The lowest strength was found for samples without any treatment (I). After sintering, the foams were characterized by a slight unevenness of the surface. This fact was clearly responsible for the poor results. Grinding of the surface alone resulted in an increase of the compressive strength by a factor of 2 (II). The compliant alumina layer (III) increased the strength even more and showed the dramatic effect of changing the uniformity of surface loading. The additional grinding (IV) had no effects on the strength. The highest values of compressive strength with the smallest scattering were obtained for samples where the struts within the surface were infiltrated with epoxy (V). This appeared to indicate that the epoxy infiltrated layer distributed the load to all struts within the contact area. The porous struts adsorbed some of the low viscosity epoxy and thus increased the strength of the single struts. The failure modes were also very different. The uncovered samples (I, II) showed a macroscopic crack oriented perpendicular to the loading direction, through the center of the specimens. After the experiment, the foam could be removed in several (but still intact) pieces. The material of the covered samples (III, IV) was crushed progressively throughout

the entire thickness and resulted in a total destruction of the foam-structure. These results indicated that the compressive strength and the failure mode are very sensitive to the method of load application used. The recommended technique of compressive testing of these materials is by infiltrating the cells at the contact surface with epoxy. However, it is not possible to carry out any high-temperature experiments using epoxy. Therefore, grinding of the foams was performed and the alumina felt was applied as buffer layer for all further experiments.

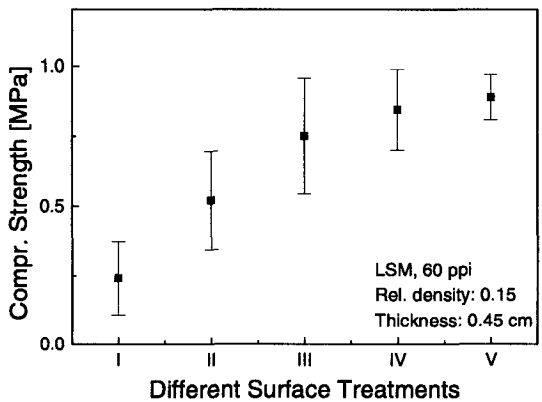

Fig. IV-22: Compressive strength of LSM foams with different surface treatments:
(I) no treatment, (II) ground surface, (III) compliant layer, (IV) ground surface and compliant layer, (V) infiltration with epoxy.

Specimen Size

Cylindrical shaped 60-ppi LSM samples with diameters of 12, 17, 28, 35 and 45 mm were used. The thickness of all samples was 0.45 cm and the relative density 0.15. Their surface was ground and covered with an alumina felt to distribute the load uniformly over all struts. The results are shown in Fig. IV-22 where the compressive strength is plotted against the different foam diameters. Specimen size had no effect. This implies that the results of compressive strength measurements can be compared to each other, independent of the specimen's size (if other parameters are kept constant).

The following experimental set-up was chosen for all experiments:

- crosshead speed 0.5 mm/min
- ceramic foams sandwiched between an alumina felt and silicon-nitride plates
- foam diameters: 33 mm for the cermet and 38 mm for the LSM foams

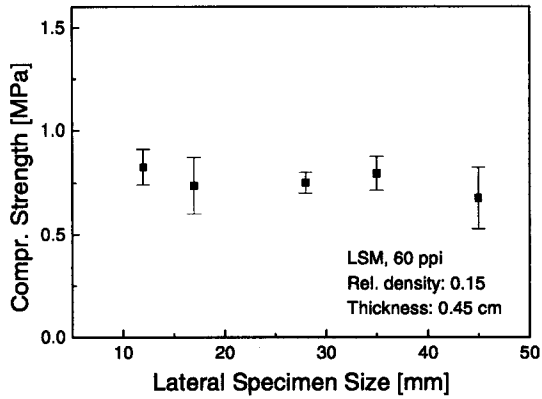

Fig. IV-23: Compressive strength vs. specimen size, samples were prepared by grinding the surface and using a compliant alumina layer.

4.2.2 Effect of Density

Ashby developed a model for the compressive strength of open cell foams [61]: Ceramic foams collapse by brittle fracture in compression. A cell wall will then fail (Fig. IV-24) when the moment M acting on it exceeds

$$M = \frac{1}{6}\sigma_f t^3 \qquad \textit{Eq. IV-12}$$

where σ_f = Modulus of rupture of cell-wall material [MPa]

M = Moment which will fracture a cell wall [Nm]

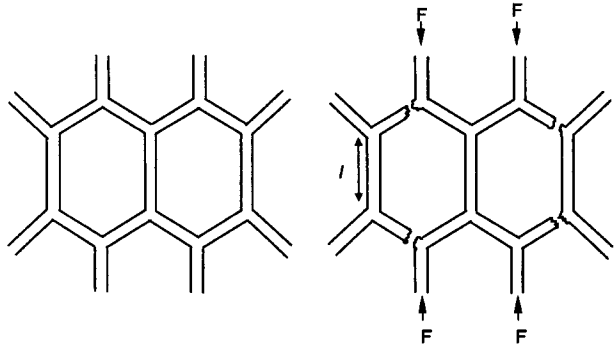

Fig. IV-24: The crushing of a ceramic foam: the modulus of rupture of the cell wall, l is exceeded, causing fracture.

A force F exerts a moment which is proportional to Fl. The stress σ on the foam is proportional to F/t^2. Combining these results, collapse by crushing will occur at the stress:

$$\sigma_f^* \propto \frac{M}{l^3} \propto \sigma_f \left(\frac{t}{l}\right)^3 \qquad \textit{Eq. IV-13}$$

where σ_f^* = compressive strength of the brittle foam [MPa].

Using Eq. IV-9 we obtain

$$\frac{\sigma_f^*}{\sigma_f} = C\left(\rho_{rel}\right)^{3/2} \qquad \textit{Eq. IV-14}$$

or by assuming that the modulus of rupture is a constant concerning the microstructure

$$\sigma_f^* \propto C_4\left(\rho_{rel}\right)^{3/2} \qquad \textit{Eq. IV-15}$$

Hence, the strength of a foam is proportional only to its density, and independent of the cell size (ppi-number) and the foam volume. This relationship will be validated in the following sections where the compressive strength is measured as a function of cell size and foam thickness.

Gibson and Asby proposed that the value of the constant C_4 is 0.65 based on a least-square fit to experimental data. However, they found this equation to be true only for relative densities less than 0.1. In structures having a relative density greater than 0.1, the material located in the corners of the cells contributes significantly to the density and must be included in the analysis. Gibson and Ashby have given the following relationship for higher-density materials:

$$\rho_{rel} = \frac{(t/l)^2 + C_5 \cdot (t/l)^3}{C_5 \cdot (1 + t/l)^3} \qquad \textit{Eq. IV-16}$$

with $C_5 = 0.333$

In Fig. IV-25 the compressive strengths of Ni-cermet precursor and of LSM foams are plotted against their density. The plot includes all measured foams independent of their cell sizes and thicknesses. It can be distinguished between three regions: Region I includes the foams with the lowest densities and the thickest foams. Foams have inhomogeneously distributed ceramic material as will be shown later, in region II the compressive strength is independent of the density. In this region the ceramic foam struts must be interconnective. Region III is characterized by a linear relationship of the strength with the density as proposed by the model.

The lowest density foams exhibit the least compressive strength. These low compressive strengths which may be attributed to the propagation of pre-existing cracks that were probably caused by the thin coating applied to the struts to lower the density. Due to the generally higher strength of the Ni-cermet precursor, it was possible to process very low density foams (rel. density 0.06) whereas the LSM-foams could only be processed with densities of at least 0.10. This is due to the general lower strength of the LSM material from which ceramic particles could be rubbed off the surface quite easily. This could not be observed for the much stronger cermet foams. Using the model equation IV-15 only region III has a linear relationship as suggested by the model. This was interpreted in terms of a significantly different failure process than assumed in the model. The theoretical failure of a foam is associated with the failure of a single strut. The observed failure in these materials can be described by a cumulative damaging process.

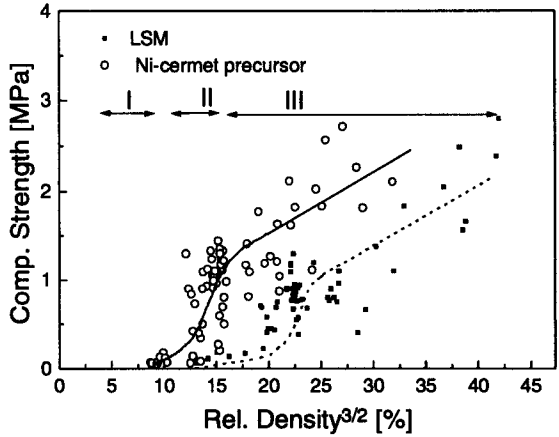

Fig. IV-25: Compressive strength vs. rel. density. For both foams three regions can be distinguished.

The number of closed cells increases significantly as the relative density of the foam increases or the cell size decreases. The foams were open celled at the low densities; however, the number of closed cells became significant larger at relative densities above 0.25. At higher densities there were also inhomogeneous regions consisting of entirely filled cells. Then the proposed relation deviated considerably from the experimental finding as the geometrical model becomes invalid.

4.2.3 Effect of Cell Size

The theoretical relationship presented by Gibson and Ashby (Eq. IV-15) suggests that the cell size should have no effect on the compressive behavior provided that the strut strength does not vary with cell size.

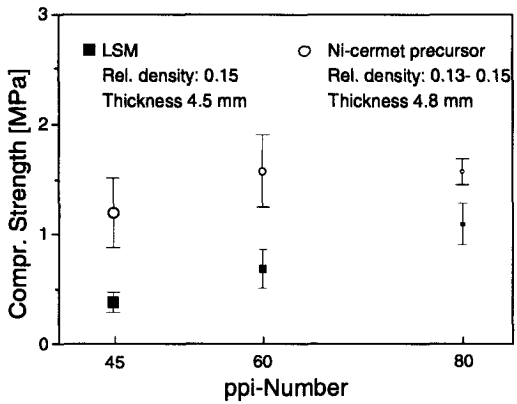

Fig. IV-26: Compressive strength of Ni-cermet precursor and LSM foams vs. ppi number.

45-, 60- and 80-ppi Ni-cermet precursors and LSM foams with different thicknesses were tested in compression. For each ppi-number and thickness, at least three samples were used. The results are illustrated in Fig. IV-26. The compressive strength of the Ni-cermet precursor foams was independent of the cell size; however, the strength of the LSM-foams depends strongly on cell size. The strength varied consistently with the ppi-number. The observed behavior may be explained in terms of a higher strength due to filled pores and due to increasing strut strength with decreasing strut length.

4.2.4 Effect of Foam Thickness

In order to study the effect of specimen thickness on compressive strength, 60-ppi foams having different thicknesses were tested in compression. For each thickness at least three foams were tested. Although the theoretical equation (Eq. IV-15) suggests that the sample thickness should have no influence on the compressive strength, the thickness of the samples did have a crucial influence on the strength (Fig. IV-26). In both materials, the strength decreases with increasing sample thickness. Ceramic foams are stronger on the outside compared to the inside. During the processing the excess slurry is squeezed out of the foams. Thus the outside of the

foam is enriched with ceramic. The thin foams with a thickness of 1.8 - 2 mm have the same strength throughout the whole volume. The difference of the stronger outer skin to the less strong inner volume can be seen at the foams with a thickness of 4.5 to 4.8 mm. The lowest strength was exhibited by the thickest foam samples with the highest volume.

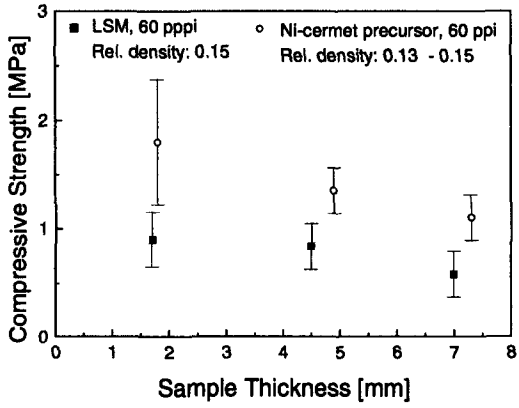

Fig. IV-27: Specimen thickness vs. *compressive strength of Ni-cermet precursor and LSM foams.*

4.2.5 Effect of Foam-Treatment

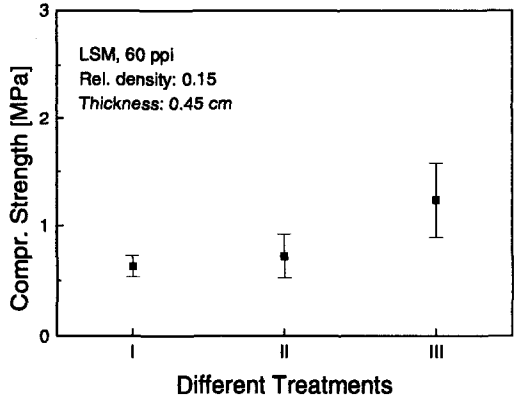

Fig. IV-28: LSM-foam: compressive strength of foam samples : (I) untreated, (II) salt impregnated, (III) twice impregnated.

As mentioned before experiments were also performed to increase the strut's thickness. One approach was by coating the foams with a second LSM-layer, the other was by impregnating the sintered foams with a salt solution which pyrolyzes to LSM (ch. IV-3.4.1). The compressive strength of five samples from each method was measured and the results are plotted in Fig. IV-28. Whereas the re-coating increased the compressive strength, the treatment with salt solution practically showed no effect. As already mentioned in chapter 2.5.2, re-coating results in a higher amount of closed cells and not in thicker struts. Nevertheless, some defects of the foam's surface will be healed by this second coating. The higher strength values are mainly due to the presence of these closed faces.

4.2.6 Reliability

Weibull statistics were performed on 16 foams of the two materials, having relative densities of 0.09 and 0.13. The results are shown in Fig. IV-29. The Weibull modulus of 8.8 of the Ni-cermet precursor foams, and 5.5 for the LSM foams, respectively, corresponds to a median strength of 1.10 MPa for the 45-ppi-Ni-cermet precursor and 0.98 MPa for the 60-ppi-LSM foams. These weibull moduli are quite high compared with those given in literature: Weibull moduli of 1.5-4 are reported for alumina foams [61, 62, 68]. The superiority of the Ni-cermet precursor precursor material over the LSM is clearly demonstrated in this plot. Although the cermet material had a lower density, the Weibull modulus and the average strength were much higher than those of the LSM material.

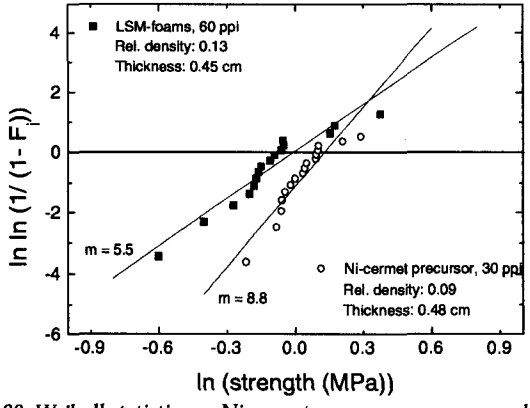

Fig. IV-29: Weibull statistics on Ni-cermet precursor precursor and LSM foams.

4.2.7 Effect of Temperature

- *Compressive Strength at Elevated Temperatures*

In Fig. IV-30 the results of compressive crushing tests at 700 °C and room temperature are compared.

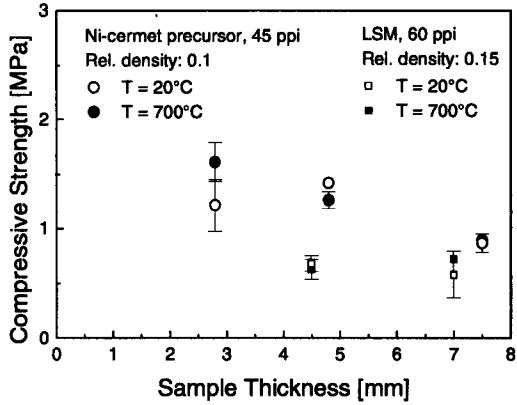

Fig. IV-30: Compressive strength of Ni-cermet precursor and LSM foams at 700 °C in comparison with room temperature measurements.

Both materials did not show a change in their compressive strength at room temperature compared with the strength at 700 °C. The strength decreased with the thickness of the samples as was already demonstrated.

Creep

Creep is a slow deformation which occurs in crystalline materials at elevated temperatures under the action of an applied stress [82]. For both materials creep during application in a SOFC would seriously affect the performance.

The creep was measured at 700 °C under a constant load of 50 N. The Ni-cermet precursor foams were tested in a reducing atmosphere to reflect the conditions at the anode, whereas the LSM foams were tested in normal air. Both materials did not show any deformation during the measurement period of 100 hrs. The creep rates were too slow at this temperature to be reliably measured.

4.2.8 Origin of Flaws

The microscopic flaws consist of pores or cracks within the struts, whereas the macroscopic flaws are broken cell struts and other imperfections in the structure. Examples of these defects are shown in Fig. IV-31. Flaws can also be present in the polymer foam before coating or can form during the processing of the ceramic. The most likely source of fracture are the sharp edges occurring along the lateral strut cracks. Failure origins often develop in the strut corners near the apex of the triangular hole where the wall is very thin. The bare, uncoated strut edges are visible as

dark streaks along the strut edges (Fig. IV-31a). Occasionally, a broken strut (Fig. IV-31b) and a pore or inclusion was observed within the strut wall (Fig. IV-31c). The large triangular holes in the struts do not necessarily reduce the strut strength, unless the apex is near the surface of the strut or is associated with a strut crack.

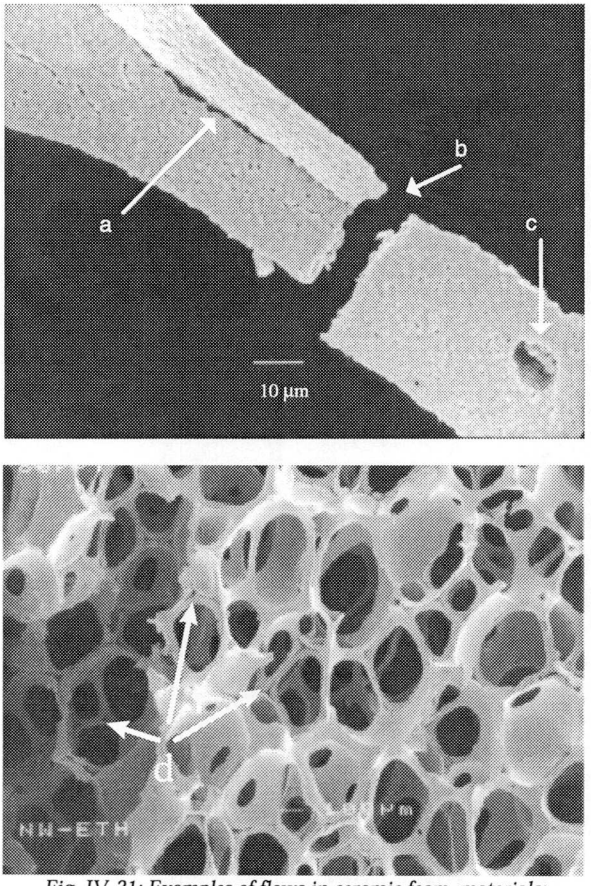

Fig. IV-31: Examples of flaws in ceramic foam materials: sharp edges (a), broken struts (b), pores (c), lateral strut cracks (d).

4.3 Electrical Properties

4.3.1 Experimental Setup

Van-der-Pauw's [83, 84] was used to measure the specific electric conductivity of the ceramic foam. This method was chosen because of the special structure of the foam which inhibits a normal 4point set-up. Bulk samples of the two materials were tested with the 4 -point method. Bulk samples were dry-pressed from powders and sintered at 1450 for LSM and at 1400 ℃ for Ni-cermet precursor. They were connected to Pt-wires according to the normal 4-point set-up. The foams are prepared for the measurements by contacting four Pt-wires with ball shaped ends to them. The Ni-cermet precursor foams were measured in air between room temperature and 700 ℃ as well as in a reducing atmosphere (50 nml H_2, 200 nml N_2). Measurements of the LSM-foams were performed in air.

4.3.2 Results and Discussion

Fig. IV-32 and Fig. IV-33 show a comparison of the electrical conductivity of foams and bulk samples of the two materials.

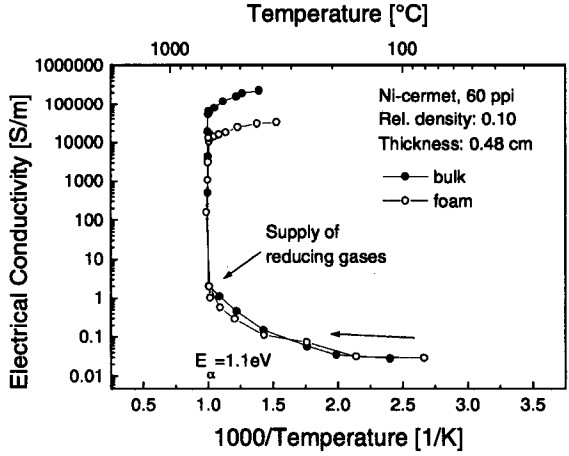

Fig. IV-32: Electrical conductivity of Ni-cermet foams and bulk Ni-cermet under oxidizing and reducing conditions.

The Ni-cermet precursor material (Fig. IV-32) exhibits ionic conductivity in air which increases with increasing temperature. This is because the doping of ceria with trivalent cations results in substitution of Ce^{4+} in the lattice which is compen-

sated by oxygen vacancies [85]. The activation energy for the conductivity in air was 1.1 eV. At low oxygen partial pressures ceria is partially reduced and develops n-type electronic conductivity. However, at low oxygen pressure the NiO is also reduced to Ni and exhibits metallic conduction. Therefore, the measured total conductivity at these low partial pressures is mainly governed by the metallic nickel with a conductivity of $85 \cdot 10^5$ S/m at 400 K [52]. The metallic conduction increases with decreasing temperature as shown in Fig. IV-32. The bulk Ni-cermet precursor material had a conductivity of $65 \cdot 10^3$ S/m at 700 °C after reduction which is considerably higher than the value of $50 \cdot 10^3$ S/m reported for Ni-zirconia at 1000 °C [86]. The foam sample had a conductivity of $14 \cdot 10^3$ S/m at 700 °C.

In the $La_{0.84}Sr_{0.16}Co_{0.02}MnO_{3-x}$ material, the substitution of Sr^{2+} for La^{3+} is expected to convert some of Mn^{3+} to Mn^{4+}. The electronic conductivity of strontium doped $LaMnO_3$ takes place via the small polaron conduction mechanism and increases with increasing temperature. A conductivity of $3.3 \cdot 10^5$ S/m was measured for the bulk LSM and $2.8 \cdot 10^4$ S/m at 700 °C for the 80-ppi LSM foam. These values are considerably higher than those reported in the [87, 88] which might be due to the small amount of Co in the starting powder. The activation energy was calculated to 0.09 eV. Generally, foams with higher ppi-numbers gave higher conductivities. The 60-ppi LSM-foams were loaded with 120 g/cm^2 for 10 and 100 hrs at 700 °C. The electrical conductivity measured before and after the mechanical loading did not show any changes.

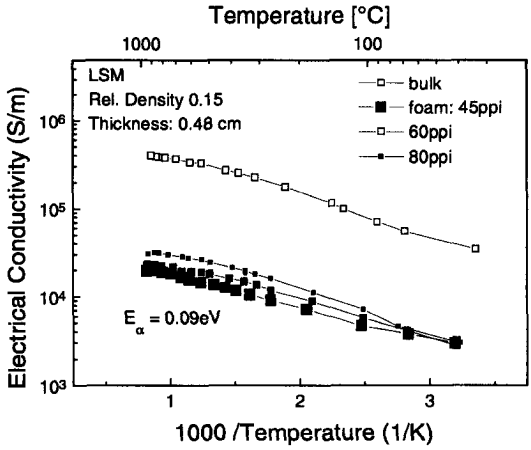

Fig. IV-33: Electrical conductivity of LSM foams and bulk LSM.

4.4 Gas Permeability

One function of the ceramic foams is the gas distribution in a solid oxide fuel cell. The applied gas (fuel or the oxygen bearing gas) has to permeate the porous structure to reach the areas of the electrodes (cathode or anode). The foam must therefore be porous enough to allow the gas to permeate easily through it, which means that the gas permeability has to be as high as possible.
There are only relatively few studies that report on the behavior of flow-through porous media [89-92]. Most references used geometrical models that resemble the unique pore structure of a foam and compared these calculated permeability values with experimental data. Generally, the pressure drop Δp can be calculated using Darcy's law [52]:

$$\frac{\Delta p}{l} = \cdot \frac{\mu}{k_1} \cdot U \qquad \textit{Eq. IV-17}$$

where Δp is the total pressure drop across a medium of length l, and specific permeability is k_1. The superficial velocity U of the fluid (with viscosity μ) is the same everywhere in the medium implying isothermal flow at a low pressure drop.
However, as shown in [92], when pore sizes are in the millimeter range, deviations from Darcy's law may occur. Such deviations are due to the contribution of fluid inertia to the energy dissipation in the porous medium. Darcy's law has to be modified to

$$\frac{\Delta p}{l} = \frac{\mu}{k_1} \cdot U + \frac{\delta}{k_2} U^2 \qquad \textit{Eq. IV-18}$$

where δ is the fluid mass density and k_2 is the "non-Darcian" permeability.

4.4.1 Experimental Set-Up

The pressure drop across the ceramic foams as a function of air-flow rate was measured at room temperature using the set-up shown in Fig. IV-34. The foams were placed on a support in an outer cylinder and kept in position by a tightly fitting inner cylinder. Air was supplied to the equipment at different flow rates. The pressure drop was taken as the pressure difference between p_1 and p_2 as indicated in the figure. 60- and 80-ppi LSM foams with a thickness of 7.8 mm were tested.

4.4.2 Results and Discussion

The pressure drop Δp is plotted versus the air flow rates in Fig. IV-35. Whereas the 60-ppi LSM foams show only a small pressure drop, the 80-ppi foams show a remarkable pressure drop of almost 4 mbar for an air flow rate of 0.6 m^3/s.

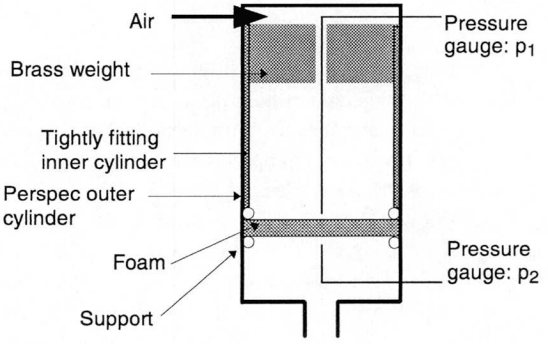

Fig. IV-34: Set-up for measuring air pressure drop across a ceramic foam. The pressure difference $\Delta p=p_2-p_1$ was taken as the pressure drop.

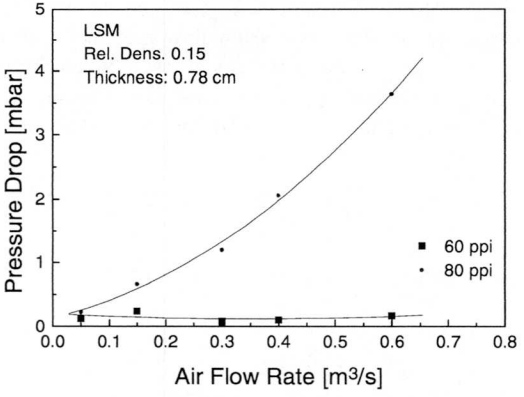

Fig. IV-35: Pressure drop of LSM foams.

The air pressure drop Δp divided by the air velocity U and foam thickness l was plotted versus the air velocity U (Fig. IV-36). The permeabilities k_1 and k_2 can now be calculated according to Eq. IV-18. μ / k_1 is taken from the value at zero flow rate and δ / k_2 is the slope of the fitted line. ($\mu = 1.83 \cdot 10^{-5}$ Pa·s at 20 ℃ and $\delta = 1.3$ g/cm^3 [52]). Hence, k_1 and k_2 are $4.49 \cdot 10^{-10}$ m^2 and $2.5 \cdot 10^{-5}$ m^2 for the 60-ppi foam. The pressure drop at 1000 ℃ can now be derived (1) assuming k_1 and k_2 do not depend on temperature and (2) using the dynamic viscosity of air at 1000 ℃ = 0.049 Pa·s [52].

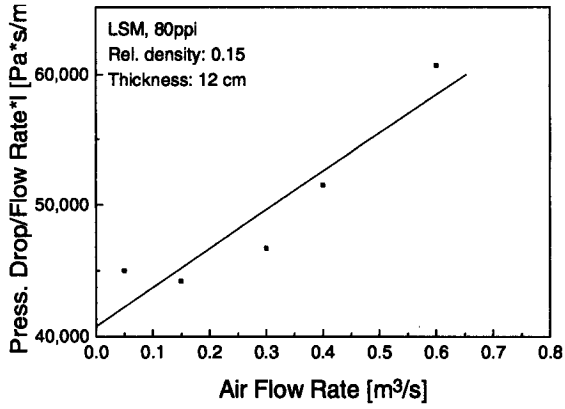

Fig. IV-36: Pressure drop of LSM foam to calculate the permeatibilities k_1 and k_2.

The calculated pressure drop at 1000 ℃ for a 60-ppi foam with a thickness of 1 cm at a flow rate of 0.6 m^3/s is 16.8 mbar which can be tolerated. However, in the Sulzer design of a solid oxide fuel cell, the gas is supplied from the outside of the planar foam, so that the "foam thickness" may reach up to 12 cm. Calculations (Eq. IV-18) for this foam thickness with the assumptions mentioned above and using the calculated numbers for k_1 and k_2 gave a pressure drop of 200 mbar. Therefore, the gas flow rate has to be adjusted to the pressure drop of the specific foam. Otherwise the solid oxide fuel cell "starves" at the reaction zone (triple phase boundary) which lowers the performance of the fuel cell.

Δp: air pressure drop[mbar] = 0 - 4 mbar (measured in Fig. IV-35) = 16.8 mbar at 1000 ℃ (calculated for foams thickness of 0.0078 m) = 200 mbar (calculated for foam thickness of 0.12 m)	k_2: "non-Darcian permeability" [m^2] = $2.27 \cdot 10^{-5}$ m^2 (calculated with Eq. IV-18 and Fig. IV-36)
l: foam thickness [m] = 0.0078 m in the experiment or 0.12 m (assumed)	U: air flow rate [m^3/s] = 0-0.6 [m^3/s] (experiment)
μ: air viscosity [Pa s] = $1.83 \cdot 10^{-5}$ Pa· s at 20 ℃ = 0.049 Pa·s at 1000 ℃ [52]	δ: air density [g/cm^3] = $1.3 \cdot 10^{3}$ [kg/m^3] [52]
k_1: specific permeability [m^2] = $4.49 \cdot 10^{-10}$ m^2 (calcul. with Eq. IV-18 and Fig. IV-36)	

5 Substrate for Electrolyte Deposition and Joining Technique

The substrate for the deposition of the electrolyte consisted of a ceramic foam as load-bearing structure and an active anodic tape as depicted in Fig. IV-37

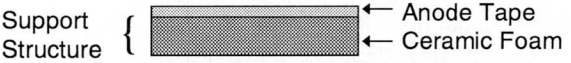

Fig. IV-37: Schematic drawing of the support structure.

The raw material for both components was Ni-cermet precursor (chapter IV-3.2), in which the ceramic constituents are ceria solid solutions (CGO) and zirconia solid solutions.

5.1 Ceramic Foam

The preparation of the load-bearing structure was already described in chapter V-3. In this section we concentrate on the preparation of the active anode and the joining of the two components.

The ceramic foam acts not only as load-bearing structure but also as current collector in the SOFC. Therefore, the two electronically conducting solids, the active anode and the ceramic foam have to be in close contact.

5.2 Active Anode

Tape casting was chosen as the most suitable method for preparing thin porous anode structures [93, 94]. The composition of the tape casting slurry is given in Table IV-8.

MATERIAL	FUNCTION	SUPPLIER
60 g Ni-CGO (9.3 m^2/g)	Powder	Praxair Speciality Ceramics, USA
10 g ZrO_2 (ss) 8 mole% Y_2O_3 (16 m^2/g)	Powder	Tosoh, Japan
23 ml Toluene	Solvent	F.E.R.O.S.A. Barcelona, Spain
1.8 g Beycostat	Dispersant	CeCaS.A., Paris, France
5.2 g PEG 600	Plasticizer	Fluka Chemie, Buchs, Switzerland
4.5 g Bis(2-ethylhexyl)phtalate	Plasticizer	Fluka Chemie, Buchs, Switzerland
5.8 g Polyvinylbutyral [10](PVB)	Binder	Hoechst, Frankfurt, FRG

Table IV-8: Slurry composition for tape casting of the active anode

The ceramic powders were dispersed in a mixture of solvent and dispersant and ball milled in a polyethylene bottle for six hours with zirconia milling balls having a diameter of 0.5 cm. After the milling the plasticizers and the binder were added and the suspension was homogenized again by ball milling for 30 minutes followed by a degassing step.

The tape-casting equipment consists of a flat glass plate and a movable doctor blade[11]. Before casting, the glass plate was covered with a PE-foil[12]. The slurry was poured onto the plate and spread by the doctor blade with an opening of 250 - 1000 μm at a speed of 30 cm/min. The tape was dried at room temperature for one day. The Ni-CGO tapes exhibited microcracks parallel and perpendicular to the pulling direction. With the addition of 16 wt % zirconia to the slurry it was possible to produce crack free tapes (A possible explanation for this effect is given in appendix 1). Circular plates were cut from such green tapes by means of a round metal puncher. The cut tapes together with the adherent polyethylene foil were placed between two porous zirconia sheets[13] and transferred to the sinter furnace.

In tape casting, the tape is normally removed from the polymer foil before sintering. However, due to the high content of organic material, our anodic tapes were very soft and adhered strongly to the polymer foil. They could not be removed from the foil without destroying the microstructure and were therefor left on the foil.

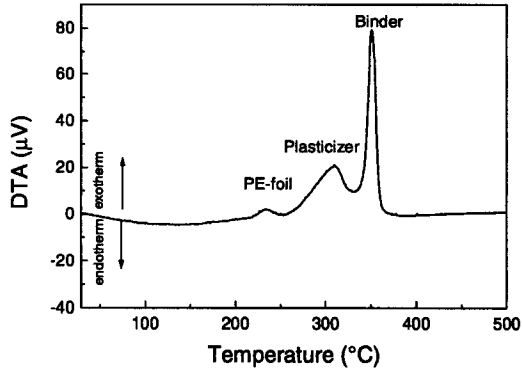

Fig. IV-38: DTA and TG measurement of the green anodic tape with PE-foil. Peaks can be assigned to the pyrolysis of the polyethylene foil, the plasticizer and the binder.

During the burn-off step the plastic foil was pyrolized. The burnout schedule was chosen in accordance with the thermogravimetric measurements shown in Fig. IV-38. The tapes were slowly heated with a heating rate of 0.5 K/min up to 400 °C. The holding time at this temperature was one hour. The tapes were then heated at

2 K/min up to 1100 ℃ in order to increase their strength. The tapes exhibit a shrinkage mostly in the radial direction whereas the thickness of the tapes changes only from 250 μm (cast) to 220 μm (dried) to 21 μm (pre-sintered at 1100 ℃) to 170 μm (fully sintered). In Fig. IV-39 the microstructure of a pre-sintered Ni-cermet precursor tape is shown. It had a high porosity of 53 vol. % (which decreased to 40 vol. % after final sintering).

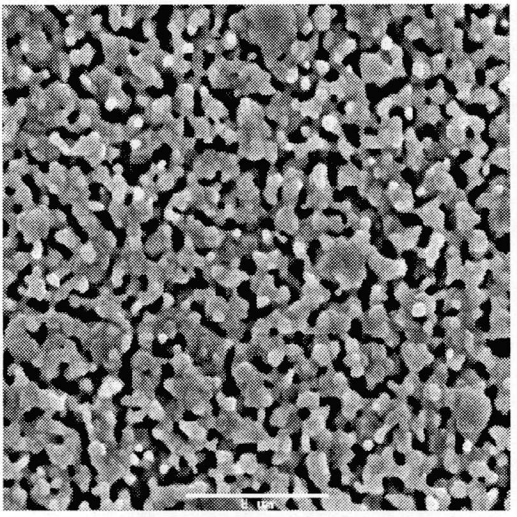

Fig. IV-39: Pre-sintered anode tape, scale 8 μm, porosity 53 vol. %, average pore size: 0.8 μm.

5.3 Joining of the Active Anode to the Ceramic Foam

Several possibilities exist for the joining of two ceramic parts [95, 96]. The two methods are: (1) joining before and (2) joining after sintering (Fig. IV-40).
In order to join two ceramic components an interlayer can be used. A ceramic interlayer joins two ceramic parts which are sintered after applying the interlayer: This is the traditional method in the ceramic industry. The two parts can be green, pre-sintered or fully sintered. Two parts may also be joined by lamination. Laminating means that two green ceramic parts are put into close contact by pressure and/or heat. Mechanical attachments are also widely used in heat exchanger and engine applications. Mechanically attached joints are usually not suitable when the components are subjected to thermal cycling. Gluing is a joining mechanism based on the surface adhesion of the glue and its strength which also limits the strength of the joint. There exist inorganic glues which resist temperatures up to 1600 ℃ [95].

Joining ceramics with a glass intermediary is a common practice in the SOFC-world and is used for joining and sealing stack elements [86, 97]. Using a metallic interlayer usually involves brazing, soldering, or diffusion bonding.

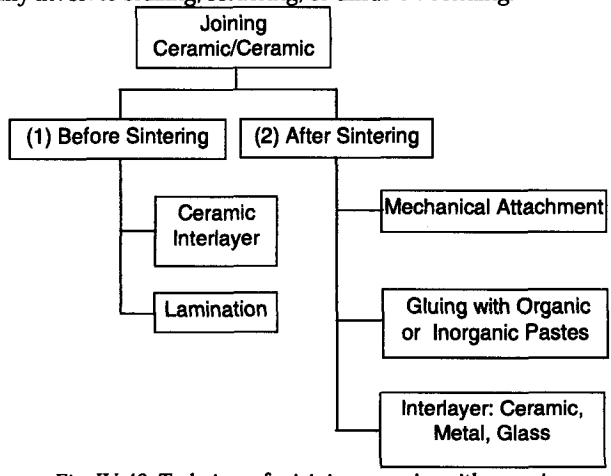

Fig. IV-40: Techniques for joining ceramics with ceramics.

The requirements for this specific joint between the ceramic foam and the anodic tape are

- good electronic conductivity with low ohmic losses
- chemical and mechanical compatibility of the intermediate material with the foam and the tape
- mechanical stability at the working temperature of the SOFC
- translation to a larger scale must be possible
- no hindrance of the accessibility of the reducing gas to the active anode.

With respect to these requirements only two joining methods are feasible:
(1) Application of a ceramic interlayer of identical composition as the ceramic foam after sintering and (2) laminating. Honegger et al. [98] who used the same substrate for the deposition of the electrolyte via PVD pressed the green foam and the green tape together before sintering.

5.3.1 Experimental Procedure

Ceramic Interlayer

The pre-sintered foam was dipped into a diluted Ni-cermet precursor suspension (10 vol. % solids loading in solvent) with the composition given in Table IV-8 and then pressed onto the pre-sintered tape. This process is schematically shown in Fig.

IV-41. Both components were pre-sintered at 1100 ℃ for one hour to give the ceramics some strength.

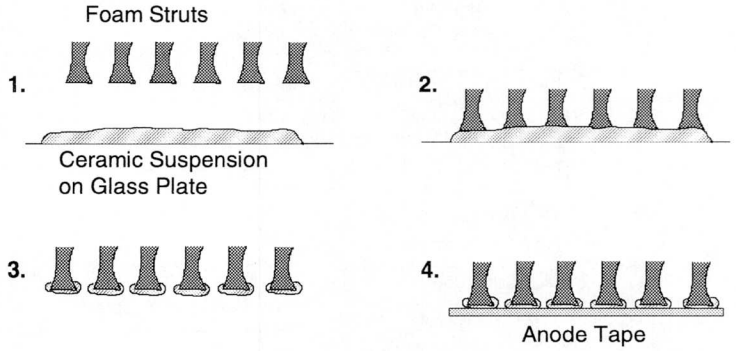

Fig. IV-41: Dip coating the ceramic foam struts with suspension of the active anode and joining to the anode tape in the green state.

Special care was taken to coat the single struts of the foams with as little ceramic as possible. A thick ceramic interlayer would give excellent strength of the joint but this layer would hinder the gas flow to the anode. Sintering was carried out at 1100 ℃ for 1 hr.

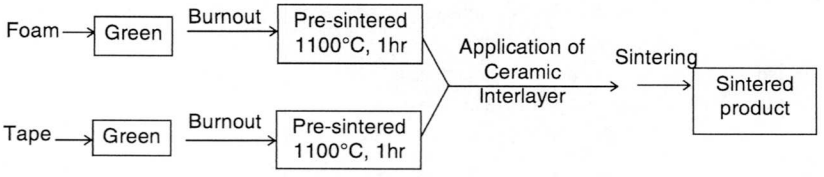

Laminating

Laminating offers several advantages such as good accessibility of the gases in the SOFC and short processing time. Laminating was performed with both components in the green state. The anodic tape was placed onto a porous zirconia plate, covered with the green foam and another porous zirconia plate, and sintered at 1100 ℃. During the final sintering at 1400 ℃ for 1 hr an additional load of 4 g/cm^2 was applied.

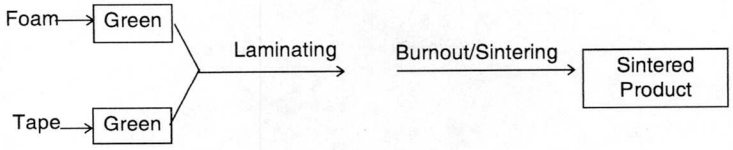

5.3.2 Characterization

Fig. IV-42 illustrates the joint resulting from the interlayer-method after completion of the sintering process at 1400 ℃. A good connection is visible between the ceramic foam and the anode tape, the ceramic interlayer has co-sintered with the two components. However, the space in between the foam struts is lowered by the interlayer (Fig. IV-43).

In Fig. IV-44 a laminated sample is shown after completion of the sinter process. It can be clearly seen that the two parts are fully sintered together thus guaranteeing the electric conductivity. The access of the reducing gases is assured because only those areas of the anodic tape are covered which are directly connected to the ceramic foam.

There is no generally valid measuring principle for the mechanical testing of such ceramic joints, however a variety of different methods is described in the literature which all measure the adhesion qualitatively or relatively. Hence the adhesion strength was tested with the "scotch tape test" [99] which is illustrated in Fig. IV-45. An adhesive tape is fixed onto the surface of the anodic tape and then removed as indicated.

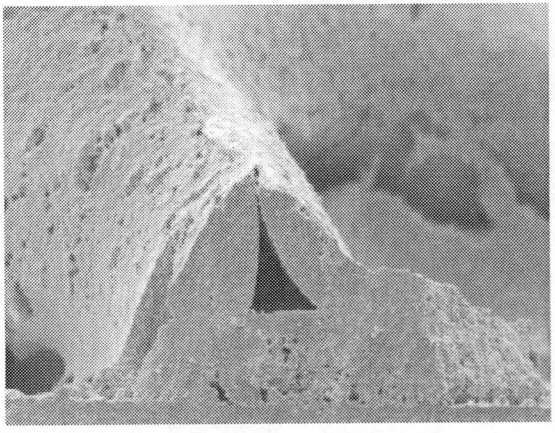

Fig. IV-42: Joint of a tape with the foam strut using a ceramic interlayer [100].

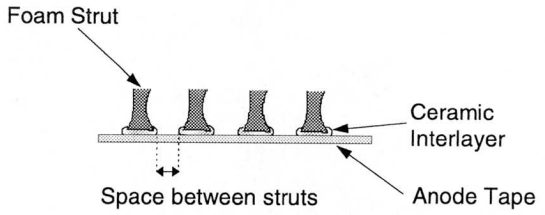

Fig. IV-43: Schematic illustration of the space between the foam struts.

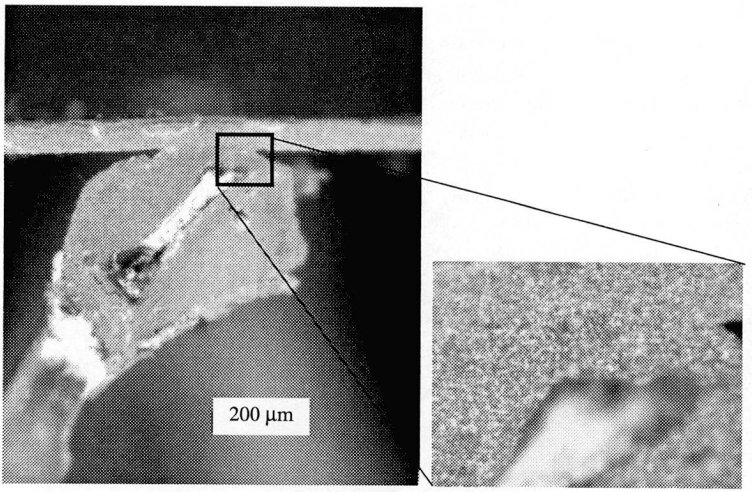

(a) *(b)*

Fig. IV-44: Joint of the tape with the foam using the laminating technique. In the left figure, a single foam strut is seen, whereas the right figure is an enlargement of the marked region which illustrates the tape interface.

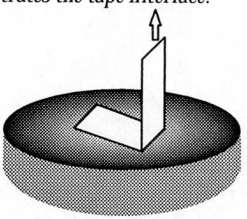

Fig. IV-45: Scotch tape test. A scotch tape is fixed onto the anodic tape and pulled as indicated.

The laminated samples exhibited by a lower mechanical strength compared with the interlayer samples. After the scotch tape test, the ceramic tapes of the interlayer samples sticked to the adhesive tape. Parts of the ceramic which were not covered by the adhesive tape remained on the foam. The ceramic tapes of the laminated samples, however, were completely detached from the foam.
Samples processed via both techniques could withstand the volume change required by the reduction of Ni-oxide to metallic nickel. The joints were still intact after heating up to 1000 ℃ in a reducing atmosphere. Both samples showed also the same high conductivity after this treatment.
The following experiments used the ceramic interlayer method.

6 Summary

Ceramic foams offer the opportunity to act simultaneously as load-bearing structure, current collector, and gas distributor in solid oxide fuel cells. Each function requires different properties such as strength, electrical conductivity, and gas permeability.

The compressive strength of cermet and LSM foams of various densities, ppi-numbers and thicknesses were measured and compared to the simple model of Gibson and Ashby [55]. It was observed that the compressive strength depends on the uniformity of loading. The mode of loading appears to affect the failure mode in these materials and can result in significant multiaxial stresses being generated within the cellular material. The recommended method of compressive testing of these materials at room temperature and at high temperatures is to apply a buffer layer of alumina felt which distributes the load more uniformly on the entire surface.
An increase of the compressive strength with increasing cell size was observed in the LSM material, whereas that of the Ni-cermet precursor foams did not depend on cell size which is in agreement with the theoretical model. The increase of strength with an increase in the number of pores can be explained by the increased strut strength and closed pores in the higher ppi-foams. The specimen thickness had a crucial influence on the compressive strength which decreases with increasing thickness due to the inhomogeneous density distribution in the workpiece. Thus, the optimum foam in regards to stability is thin with a high ppi-number for the LSM material, whereas the ppi-number is irrelevant for the Ni-cermet precursor.

Handling of the sintered foams was generally satisfactory except for the LSM-foams from which particles could be rubbed off quite easily.
45-ppi Ni-cermet precursor foams had an average strength of 1.6 MPa whereas 60-ppi LSM foams exhibit an average strength of 0.73 MPa. Hence, the foams fulfill the requirements of load-bearing structures. The foams can bear quite easily the required weight of 400 g/cm^2 (Siemens) or 120 g/cm^2 (Sulzer).
All compressive strength values are in the same order of magnitude as given in the literature [62, 69, 74, 76].
The electrical conductivity of both materials was measured as a function of temperature. The bulk materials exhibit higher conductivities than the foam samples. However, the foam samples show a conductivity high enough for the use as current collectors in solid oxide fuel cell applications. The conductivity did not change after applying a load of 120 g/cm^2 or 400 g/cm^2 to them which corresponds to the weight requirement by the Sulzer or the Siemens design. Compared to the conductivities of bulk samples, the foams showed a considerable lower conductivity. With increasing pore size (decreasing ppi-number) the conductivities showed smaller values. This result implies that the best foam with regard to electrical conductivity has a high ppi-number.
It was demonstrated that the pressure drop in ceramic foams is a variable of the cell size. The pressure drop can be neglected at room temperature but is remarkably increased at higher temperatures due to the strongly increasing viscosity of the gases used at higher temperatures. Using a gas flow rate at 0.6 m^3/s there is a pressure drop of about 16 mbar at 1000 ℃ for 60-ppi foams with a thickness or 7.8 mm, which can is acceptable. However, for thicker foams and for foams with high ppi-numbers the pressure drop increases dramatically. The pore size of these foams has to be as low as possible to guarantee a good performance of the solid oxide fuel cell. Depending on the fuel cell design used, the pore size and the thickness of the foams have to be adjusted. The lower the pressure of the used gases is, the larger the pore size of the used ceramic foams must be. The air permeability is also a function of cell size and thickness. The optimum foam concerning permeability should have a low ppi-number and be as thin as possible.

In order to fulfill all these requirements a compromise has to be found depending on the fuel cell design and the gas flow rate used. For the Sulzer design e.g. it turned out that a 30-ppi Ni-cermet precursor foam and a 60-ppi LSM foam, both with a thickness of 3 mm had the best combination of all required properties [60].

The substrate for the electrophoretic deposition experiments which will be described in the following chapter V, consisted of a ceramic foam and an active anodic tape. The raw material for both components was Ni-cermet precursor (chapter

IV-3.2), in which the ceramic constituents are ceria solid solutions (CGO) and zirconia solid solutions. The ceramic foam and the active anode were prepared using the polymer-sponge method described in chapter IV-3 and via tape casting as described in chapter V-6, respectively. For the joining of the two separately prepared components the applying of a ceramic interlayer between ceramic foam and anodic tape was chosen.

7 References

[1] H. Greiner, T. Grögler, W. Kock, and R. Singer, "Chromium Based Alloys for High Temperature SOFC Applications", SOFC IV, Yokohama, Japan, M. Dokiya, O. Yamamoto, H. Tagawa, and S. C. Singhal, Eds., pp. 879-888., 1995.

[2] H. P. Buchkremer, U. Diekmann, L. G. J. de Haart, H. Kabs, U. Stimming, and D. Stöver, "Advances in the Anode Supported Planar SOFC Technology", SOFC V, Aachen, Germany, U. Stimming, S. C. Singhal, H. Tagawa, and W. Lehnert, Eds., The Electrochemical Society, pp. 160-170,1997.

[3] K. Sasaki, "Phase Equilibria, Electrical Conductivity, and Electrochemical Properties of ZrO_2-In_2O_3," Diss ETH No. 10331, Ph.D. Thesis, ETH Zürich,. 1993.

[4] D. A. Hirschfeld, T. K. Li, and D. M. Liu, "Processing of Porous Oxide Ceramics", *Key Engineering Materials*, **115**, pp. 65-80, 1996.

[5] C. Lavernia and J. M. Schoenung, "Calcium Phosphate Ceramics as Bone Subsitutes", *J. Am. Ceram. Soc.*, **70**, pp. 95-100, 1990.

[6] M. Mathey, C. Meier, P. Lüscher, J. Mayer, E. Wintermantel, and B. Koch, "A New Intervertebral Disc Respacing Biomaterial: Open Porous, Hydroxylapatite Filled Polymethacrylate", Int. Symp. Biomed. Eng. 21st Century, Taipei, Taiwan, pp. 1-6,1992.

[7] A. J. Shermann, R. H. Tuffias, and R. B. Kaplan, "Refractory Ceramic Foams: A Novel, New High-Temperature Structure", *J. Am. Ceram. Soc. Bull.*, **70**, pp. 1025-1029, 1991.

[8] A. Makishama, J. D. Mackensie, and J. J. Hammel, "The Leaching of Phase Separated Sodium Borosilicate Glasses", *J. Non-Cryst. Solids*, **31**, pp. 377-383, 1979.

[9] P. Eggerstedt and J.-F. Ziever, "Use of Porous Ceramics to Remove Particulates from Hot Gas Streams", Particulate and Multiphase Processes,

Miami, Fl., USA, Hemisphere Publ Corp, Washington, DC, USA, pp. 27-42,1987.

[10] T. Mizrah, J.-P. Gabathuler, L. J. Gauckler, A. Baiker, L. Padeste, and H. P. Meyer, "SELEE: Schaumkeramik für die Abgasreinigung", Keramik im Umweltschutz, Köln, Germany, DKG, pp. 143-169, 1988.

[11] T. Mizrah, A. Maurer, L. J. Gauckler, and J.-P. Gabathuler, "Open-Pore Ceramic Foam as Diesel Particulate Filter", International Congress and Exposition, Detroit, USA, The Engineering Society, pp. 19-27, 1989.

[12] L. M. Sheppard, "The Changing Demand for Ceramic Additives", *Ceram. Bull.*, **69**, pp. 802-805, 1990.

[13] J. D. Rutherford, G. P. Walker, and C. A. Loong, "Ceramic Foam Filtration of Zinc Alloys", SDCE International Die Casting Exposition & Congress, Die Casting Engineers, Grove, IL, USA, p. 10, 1985.

[14] J. Brockmeyer and J. F. Pirzzirusso, "Ceramic Foam Offers Surprising Properties", *ME*, **5**, pp. 39-41, 1988.

[15] S. B. Bhaduri and Z. B. Quian, "Processing/Properties Correlations of Composite Ceramic Foams.", *J. Mat. Synth. and Processing*, **3**, pp. 361-369, 1995.

[16] K. Schwartzwalder and A. V. Somers, "Method of Making a Porous Shape of Sintered Refractory Ceramic Articles" Patent No. 3 097 830, USA, 1963

[17] P. Sepulveda, "Gelcasting Foams for Porous Ceramics", J. *Am. Ceram. Soc. Bull.*, **76**, pp. 61-70, 1997.

[18] H. Abe, A. Tsuzuki, H. Tateyama, and M. Egashira, "Preparation of Microporous Material from Cordierite by Acid Treatments", *Key. Eng. Mater.*, **115**, pp. 159-166, 1996.

[19] M. Lehigh and I. Nettleship, "Microstructural Evolution of Porous Ceramics", Advances in Porous Materials Materials Research Society Symposium, Boston, MA, USA, Materials Research Society, Pittsburgh, PA, USA, pp. 315-320, 1995.

[20] R. B. Bagwell and G. L. Messing, "Critical Factors in the Production of Sol-Gel-Derived Porous Alumina", *J. Am. Ceram. Soc.*, **77**, pp. 3137-3141, 1996

[21] L. C. Klein and R. H. Woodman, "Porous Silica by the Sol-Gel Process", *Key Eng. Mater.*, **115**, pp. 109-124, 1996.

[22] T. Fujiu, G. L. Messing, and W. Huebner, "Processing and Properties of Cellular Silica Synthesized by Foaming Sol-Gels", *J. Am. Ceram. Soc.*, **73**, pp. 85-90, 1990.

[23] R. Pirard, S. Blacher, F. Brouers, and J. P. Pirard, "Interpretation of Mercury Porosimetry Applied to Aerogels", *Mat. Res. Soc. Proc.*, **3317**, pp. 517-522, 1995.

[24] D. J. Green, "Fabrication and Mechanical Properties of Lightweight Ceramics Produced by Sintering of Hollow Spheres", *J. Am. Ceram. Soc.*, **68**, pp. 403-409, 1985.

[25] T. Litovsky, R. Ytermann, E. Litovsky, M. Shapiro, and A. Shavit, "Thermal Conductivity of High-Temperature Ceramic Thermal Insulations", *Mater. Res. Soc. Symp. Proc.*, **371**, p. 309, 1995.

[26] H. Verweig, G. Dewith, and D. Veenenam, "Hollow Glass Microsphere Composite", *Mater. Eng.*, **105**, pp. 39-41, 1985.

[27] M. B. Volf, *Technical Glasses*, London: Pitman, pp. 43-57, 1961.

[28] M. Wu, T. Fujiu, and G. L. Messing, "Synthesis of Cellular Inorganic Materials by Foaming Sol-Gels", *J. Non-Cryst. Solids*, **121**, pp. 407-412, 1990.

[29] S. J. Powell and J. R. G. Evans, "Structure of Ceramic Foams Prepared from Polyurethane-Ceramic Suspensions", *Mater. Manuf. Processes*, **10**, pp. 757-771, 1995.

[30] R. T. Smith, J. G. P. Binner, and R. Sambrook, M,, "Processing of High Porosity Engineering Ceramics", 2nd Int. Conf. on Ceramics in Energy Applications, London, p. 381,1994.

[31] J. Adler, G. Standke, and H. Stöver, "Schaumkeramik - ein alter neuer Werkstoff", Werkstoffwoche 1996, Symp. 6: Werkstoff- und Verfahrenstechnik, Stuttgart, Germany, pp. 367-372, 1996.

[32] J. Adler, G. Standke, and H. Stöver, "Offenzellige Schaumkeramik", in *Technische Keramische Werkstoffe*, J. Kriegesmann, Ed. Köln: Deutscher Wirtschaftsdienst, 1997, pp. 4.6.1.0. p.1-25.

[33] J. Saggio-Woyansky, C. E. Scott, and W. P. Minear, "Porous Ceramics", *J. Am.Ceram. Soc. Bull.*, **71**, pp. 1674-1682, 1992.

[34] F. F. Lange and K. T. Miller, "Open-Cell, Low-Density Ceramics Fabricated from Reticulated Polymer Substrates", *Adv. Ceram. Mat.*, **2**, pp. 827-831, 1987.

[35] F. Drache, "Aus Kunststoff wird Keramik für die Metallurgie", *Reportagen, Reports, DKG* **73**, 6, pp. 349-350, 1996.

[36] D. D. Brown and G. D.J., "Investigation of Strut Crack Formation in Open Cell Alumina Ceramics", *J. Am. Ceram. Soc.*, **77**, pp. 1467-1472, 1994.

[37] P. C. Rojas, G. J. Piderit, and P. Toro, "Development of Open-Pore Silicon Carbide Foams", *Key Engin. Mat.*, **132-136**, pp. 1731-1734, 1997.

[38] J. Briggs, "Engineering Ceramics in Europe", FT Managment Report, 1995.

[39] G. Menges and F. Knipschild, *Polym. Eng. Sci.*, **15**, pp. 623-627, 1975.

[40] F. A. Shutov, *Integral/Structural Polymer Foams.* Berlin: Springer Verlag, pp. 8-12, 1986.

[41] F. A. Shutov, *Foamed Polymers: Processing and Production Technology.* Basel, CH: Techn. Publish. AG, p. 15-19, 1991.

[42] F. Drache, "Personal Communication", Fa. Drache, Diez, Germany, 1996.

[43] A.A. Standards, *Cell Size of Rigid Cellular Plastics*, **08.03**, 1977.

[44] E. E. Underwood, *Quantitative Sterology.* MA: Addison-Welsely Publ. Reading, 1970.

[45] D. J. Shaw, *Introduction to Colloid and Surface Chemistry*, London: Butterworths, 1986.

[46] H. A. Barnes, "Shear-Thickening ("Dilatancy") in Suspensions of Nonaggregating Solid Particles Dispersed in Newtonian Liquids", *J. Rheol.*, **33**, pp. 329-366, 1989.

[47] D. Shanefield, "Personal Communication", Rutgers University, Piscataway, USA, 1997.

[48]] D. Shanefield, *Organic Additives and Ceramic Processing.* Boston, USA: Kluwer Academic Press, 1995.

[49] A. P. Boresi and O. M. Sidebottom, *Advanced Mechanics of Materials*, 4th ed. New York: Wiley & Sons, 1985.

[50] J. Reed, *Introduction to the Principles of Ceramic Processing.* New York: J. Wiley & Sons, 1996.

[51] A. P. Amyx, D. M. Bass, and R. L. Whiting, *Petroleum Reservoir Engineering.* New York: McGraw-Hill, 1960.

[52] R. C. Weast and D. R. Lide, *Handbook of Chemistry and Physics.* Florida, USA: CRC Publishers, 1990.

[53] J. Reed, *Introduction to the Principles of Ceramic Processing.* New York: J. Wiley & Sons, p. 306, 1996.

[54] D. J. Green, C. Nader, and R. Brezny, "The Elastic Behaviour of Partially Sintered Alumina", *Ceram. Trans.*, **7**, pp. 345-356, 1990.

[55] L. J. Gibson and M. F. Ashby, *Cellular Solids: Structure and Properties*, New York: Pergamon Press, 1988.

[56] J. Reed, *Introduction to the Principles of Ceramic Processing.* New York: J. Wiley & Sons, pp. 216-217,1996.

[57] D. J. Green, "Mechanical Behavior of Porous Ceramics", 11th Riso Int. Symposium on Metallurgy and Materials Science, Riso, , pp. 297-302,1990.

[58] D. D. Green, The Pennsylvania State University, PA, USA, "Personal Communication", 1998.

[59] H. Greiner, Siemens AG, Erlangen, Germany, "Personal Communication", 1998.

[60] K. Honegger, Sulzer Innotec AG, Winterthur Switzerland, "Personal Communication", 1997.

[61] M. F. Ashby, "The Mechanical Properties of Cellular Solids," *Metall Trans A*, vol. 14A, pp. 1755-1769, 1983.

[62] R. Brezny and D. J. Green, "Fracture Behavior of Open-Cell Ceramics.," *Mat. Res. Soc. Proc*, vol. 207, pp. 3-8, 1991.

[63] A. N. Gent and A. G. Thomas, *J. Appl. Polym. Sci.*, vol. 1, pp. 107-113, 1959.

[64] J. M. Ledermann, *J. Appl. Polym. Sc.*, vol. 15, pp. 693-703, 1979.

[65] R. Chan and M. Nakamura, *J. Cell. Plast.*, vol. 5, pp. 112, 1969.

[66] M. R. Patel, *J. Mater. Sc.*, vol. 5, pp. 909-932, 1970.

[67] R. Brezny and D. J. Green, "Characterization of Edge Effects in Cellular Materials," *J. Mat. Sc.*, vol. 25, pp. 4571-4578, 1990.

[68] R. Brezny and D. J. Green, "The Effect of Cell Size on the Mechanical Behavior of Cellular Materials," *Acta Metall. Mater.*, vol. 38, pp. 2517-2526, 1990.

[69] R. Brezny and D. J. Green, "Uniaxial Strength Behavior of Brittle Cellular," *J. Am. Ceram. Soc.*, vol. 76, pp. 2185-2192, 1993.

[70] D. J. Green and R. Brezny, "Fractographic Determination of Strut Strength in Cellular Ceramics" in *Ceramic Transactions*, **17**, J. R. Varner, V.d. Frechette, Ed. Westerville, Ohio: The American Ceramic Society, pp. 119-128,1990.

[71] K. C. Goretta, R. Brezny, C. Q. Dam, and D. J. Green, "High Temperature Mechanical Behavior of Porous Open-Cell Al_2O_3", *Mat. Sc. Engin.*, **A124**, pp. 151-158, 1990.

[72] Y. Aoki and B. McEnaney, "SiC Foams Produced by Siliciding Carbon Foams", *Brit. Ceram. Transact.*, **94**, pp. 133-137, 1995.

[73] A. A. Wereszczak, E. Liu, V. Heng, T. P. Kirkland, and M. K. Ferber, "The High Temperature Compressive Strength of Non-Oxide Ceramic Foams", *Mat. Sci. and Engin.*, **A219**, pp. 224-228, 1996.

[74] L. A. Strom, T. B. Sweeting, and J. R. Morris, "Advanced Reticulated Ceramics", J. *Cookson Techn.*, pp.13-15, 1996.

[75] R R. Brezny, D. J. Green, and C. Q. Dam, "Evaluation of Strut Strength in Open-Cell Ceramics", *J. Am. Ceram. Soc.*, **72**, pp. 885-889, 1989.

[76] V. N. Antsiferov and V. I. Ovchinnikova, "Optimization of Rheological properties of suspensions to produce high-porous cellular ceramic materials", *Ogneupory*, **3**, pp. 23-27, 1997.

[77] F. Cabannes, K. Dembinski, and Y. Bigay, "Creep Behavior of Zirconia Foams used in Electrical Furnaces", *Journal de Physique (Paris), Colloque C1*, **47**, pp. 649-654, 1986.

[78] D. J. Green, "Mechanical Behaviour of Light Weight Ceramics", J.J. Bentzen, J.B. Bilde, (Ed.), 11th Risø Int. Symposium on Metallurgy and Materials Science, pp 297-302, 1986.

[79] Hi-Tech Ceramic Inc., Alfred, N.Y. USA, 1998.

[80] E. Ryshkewitch, *J. Am. Ceram. Soc.*, **36**, pp. 65, 1953.

[81] C. Q. Dam, R. Brezny, and D. J. Green, "Compressive Behavior and Deformation -Mode Map of an Open cell Alumina", *J. Mater. Res.*, **5**, pp. 163-171, 1990.

[82] R. Cannon and T. G. Langdon, "Review: Creep of Ceramics", *J. Mat. Science*, **18**, pp. 1-50, 1983.

[83] L. J. Van der Pauw, "A Method of Measuring the Resistivity and Hall Coefficient on Lamellae of Arbitrary Shape", *Phil. Techn. Review*, **20**, pp. 220-224, 1958.

[84] L. J. Van der Pauw, "A Method of Measuring Specific Resistivity and Hall Effect of Discs of Arbitary Shape.", *Philips Res. Repts.*, **13**, pp. 1-9, 1958.

[85] M. Gödickemeier, "Mixed Ionic Electronic Conductors for Solid Oxide Fuel Cells", Diss. ETH No. 11348, Ph.D.-Thesis, ETH Zürich, 1996.

[86] N. Q. Minh and T. Takehiko, "Science and Technology of Ceramic Fuel Cells", Amsterdam: Elsevier, pp. 70-90, 1995.

[87] E. Ivers-Tiffée, M. Schiessl, H. J. Oel, and W. Wersing, "SOFC Cathodes with Mixed Conduction: Advantages and Limitations of Co Containing Perovskites.", 69-87, 1993.

[88] K. Katayama, T. Ishihara, H. Ohta, S. Takeuchi, Y. Esaki, and E. Inukai, "Sintering and Electrical Conductivity of $La_{1-x}Sr_xMnO_3$", *J. Ceram. Soc. Jpn. Inter. Ed.*, **97**, pp. 1324-1330, 1989.

[89] G. F. A. Acosta, E. A. H. Castillejos, R. J. M. Almanza, and V. A. Flores, "Analysis of Liquid Flow Through Ceramic Porous Media Used for Molten Metal Filtration", *Metal.. Mat.Transact. B*, **26**, pp. 159-171, 1995.

[90] M. J. Hall and J. P. Hiatt, "Exit Flows from Highly Porous Media", *Phys. Fluids*, **6 (2)**, pp. 469-479, 1994.

[91] M. J. Hall and J. P. Hiatt, "Measurements of Pore Scale Flows Within and Exiting Ceramic Foams", *Experiments in Fluids*, **20**, pp. 433-440, 1996.

[92] A. P. Philipse and H. L. Schram, "Non-Darcian Airflow through Ceramic Foams", *J. Am. Ceram. Soc.*, **74**, pp. 728-732, 1991.

[93] R. E. Mistler, D. J. Shanefield, and R. B. Runk, "Tape Casting of Ceramics", in *Ceramic Processing before Firing*, R. E. Mistler, Ed., pp. 411-449, 978.

[94] W. R. Cannon, J. R. Morris, and K. R. Mikeska, "Tape Casting", in *Mulitlayer Ceramic Device*, **19**, *Advances in Ceramics*, 1986, pp. 161-175.

[95] M. M. Schwartz, *Ceramic Joining*. Ohio, USA: ASM International, pp. 76-83, 1990.

[96] M. G. Nicholas, "Joining of Ceramics", in *Materials Science and Technology*, **17B**, R. W. Cahn, Haasen, P., Kramer, E.J., Ed. Weinheim: VCH, pp. 261-292, 1996.

[97] K. Kordesch and S. Günther, *Fuel Cells and Their Application*. Weinheim: VCH Verlagsgesellschaft, 1996.

[98] K. Honegger, E. Batawi, C. Sprecher, and R. Diethelm, "Thin Film Solid Oxide Fuel Cell (SOFC) for Intermediate Temperature Operation (700 ℃)," SOFC V, U. Stimming, S.C. Singhal, H. Tagawa, W. Lehnert (Eds.),.Aachen, Germany, pp. 321-329,1997.

[99] K. L. Mittal, "Adhesion Measurement of Thin Films", Adhesion Measurement of Thin Films, Thick Films, and Bulk Coatings, Philadelphia, ASTM Special Technical Publication, p. 640, 1976

[100] C. Kleinlogel, ETH Zurich, Chair of nonmetallic materials, Switzerland, private communication.

V Electrophoretic Deposition (EPD) of ZrO_2-Thin Film Electrolytes

In this chapter the preparation of the electrolyte is described. A comparison of the different processing methods for thin electrolyte layers is given. Emphasis is put on the electrophoretic deposition process which is studied in detail. The preparation of the ceramic powder suspension, the substrate, and the design of the electrophoresis apparatus are presented. Conditions for the deposition are discussed and a model of the deposition mechanism is proposed.

1 Introduction

Present SOFC technology employs almost exclusively stabilized zirconia as electrolyte with a typical thickness of 50 to 300 µm. The electrical resistivity of the electrolyte necessitates an operating temperature of 950 to 1000 ℃ to limit voltage losses during operation.
Zirconia layers of about 15 µm have an acceptable conductivity at 700 ℃, with an area resistance of less than 0.15 Ωcm^2 [1, 2]. In the past, several techniques have been reported concerning the development of thin-film processes for SOFC applications [1-16].

The aim of this study was to use deposition methods which start with a ceramic powder suspension to obtain thin zirconia layers on electrode substrates such as described in chapter IV-5.

2 Comparison of Different Electrolyte Preparation Techniques Using Powders

From all the known processes for deposition of thin layers only those were considered which start with a ceramic powder. These are sedimentation [17], pressure filtration [18-20], tape casting [21-24], spin coating [5, 25, 26], sol-gel processes [27-30], slurry coating [4, 15, 31-33], screen-printing [24, 34-36], transfer-printing [37], tape laminating [24, 38, 39] and electrophoretic deposition [40-45]. All such deposition techniques have certain characteristics listed below and require certain properties of the substrates such as porosity, flatness, size, sinter properties, etc.. These are summarized in Table V-1.

Sedimentation:

- very simple processing steps
- easy parameter control (solids content, particle size, sedimentation time etc)
- not suitable for very fine particles
- sedimentation produces very homogeneous and dense layers
- extremely time consuming process
- tolerates rough and uneven substrate surfaces
- tolerates high porosity of the substrate and mechanical weak substrates
- not industrially applicable.

Tape Casting:

- simple processing steps
- difficult parameter control (solids content, particle size, surface area, organic content, etc.)
- smooth surfaces of the tape cast layers
- precise dimensional tolerances
- outstanding productivity
- difficult binder burnout
- success of tape casting process depends strongly on the slurry formulation and process parameters
- difficult sintering for larger parts due to warpage
- industrially established process
- multilayer tapes possible
- applicable for thicknesses from 10 to 400 µm.

Slurry Coating:

- easy parameter control (suspension characteristics, coating cycles, etc.)
- unaffected by substrate roughness.

Screen-printing:

- inexpensive and quick process
- simple of fabrication parameters
- requires high surface flatness and high mechanical strength of the substrate
- industrially established process for flat substrates.

Transfer Printing:

- simple equipment
- difficult organics burn-off step
- process applicable to different substrate geometries
- requires low to medium mechanical strength of the substrate
- unaffected by substrate porosity and geometry
- industrially established process.

Electrophoretic Deposition:

- easy parameter control (voltage, time, field strength, suspension characteristics such as particle size, solids content etc.)
- requires surface charge of ceramic particles
- unaffected by surface roughness and porosity of substrate
- requires medium strength and electric conductivity of the substrate
- difficult substrate fixation
- industrially established process.

Process	Properties of the Substrate		
	Flatness	Porosity	Mechanical Strength
Sedimentation	nsr	nsr	nsr
Pressure Filtration	high	high	high
Spin Coating	very high	low	medium
Sol-Gel Processes	nsr	low-none	low
Slurry Coating	nsr	low	low
Screen-printing	high	nsr	high
Transfer Printing	medium	nsr	medium
Tape Laminating	green substrate		
Elect. Deposition	nsr	nsr	medium

nsr: no special requirement

Table V-1: Requirements on the substrate for electrolyte deposition.

From all the feasible procession techniques only those were chosen which could be applied easily for the existing anode support structure. Hence, all processing techniques were not considered which require very flat surfaces and high mechanical strength of the substrate. Techniques which use special equipment were also rejected. The sol-gel process was discarded because it is applicable only to substrates with very low porosity. Tape laminating is a processing technique which does not require a substrate. If thick and stable enough, the green anode tape (chapter IV-5) can be directly used for the lamination process.

In this work the electrophoretic deposition method was studied in detail whereas the other processing techniques (sedimentation, tape lamination, slurry coating, and transfer printing) were only roughly evaluated. Information on those processes and examples of the deposited layers are given in appendix 2.

3 Electrophoretic Deposition

The phenomenon of electrophoresis was discovered by the Russian scientist Reuss in 1809 [46]. He observed the movement of clay particles in a water based suspension under the influence of an electrical field. The positively charged clay particles thereby moved to the negatively charged electrode. In 1927, electrophoresis was used commercially for the precipitation of latex [47]. DeBoer employed electrophoresis for deposition in 1939 [48], followed later by the first solid ceramic bodies in the form of ceramic crucibles in 1948 [49]. Up to now, electrophoretic deposition (EPD) is relevant in three technical fields: (1) analytical and separation method in the field of biochemistry [50], (2) coating of metals [51-54] and (3) processing of bulk ceramics such as the processing of Al_2O_3-tubes [55, 56] sanitary articles [57], superconductors [58-61] and substrates for superconductors [62, 63], and microlaminate composites [64-67].

Electrophoretic deposition is a colloidal process for ceramics wherein ceramic bodies are shaped directly from a stable colloid suspension by applying a dc electric field [40, 41, 68-72] (Fig. V-1). This causes the charged particles to move toward, and deposit on, the oppositely charged electrode. EPD is a combination of two processes: electrophoresis and deposition: electrophoresis is the motion of charged particles in a suspension under the influence of an electric field; deposition is the coagulation of particles to form a dense layer on the electrode.

The migration velocity of a particle moving under electrophoresis is inversely proportional to the viscosity of the medium, proportional to the strength of the applied filed, proportional to the net charge on the particle, and inversely proportional to the size of the particle [73].

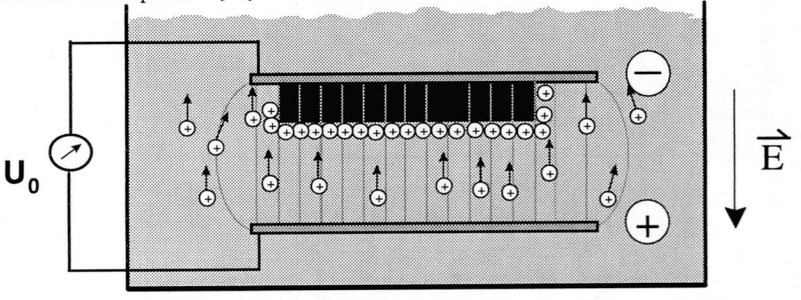

Fig. V-1: Schematic of the deposition cell for electrophoreses. Charged ceramic particles migrate under the influence of an electric field.

In this work, the electrophoretic deposition method was used to deposit zirconia particles in ethanol suspensions on porous Ni-cermet substrates. After sintering, the zirconia acts as

solid electrolyte in a SOFC whereas the porous substrate is the active anode.

3.1 Experimental Set-Up for EPD

3.1.1 EPD-Apparatus and Used Equipment

The EPD-apparatus generally consists of two electrodes at a certain distance in a suspension. An electrical field is produced by applying a voltage between these plates. This field must be homogeneous to guarantee a homogeneous deposition of the ceramic particles. Based on measurements and estimations given in appendix 3 the dimensions of the apparatus were chosen in such a way, that the electrical field is homogeneously distributed over the whole substrate. Two mm thick copper plates were used as electrodes with a size of 120x120 mm^2. The apparatus was constructed with exchangeable PVC spacers to allow variable plate distances from 10 - 100 mm. A schematic drawing of the apparatus is shown in Fig. V-2.

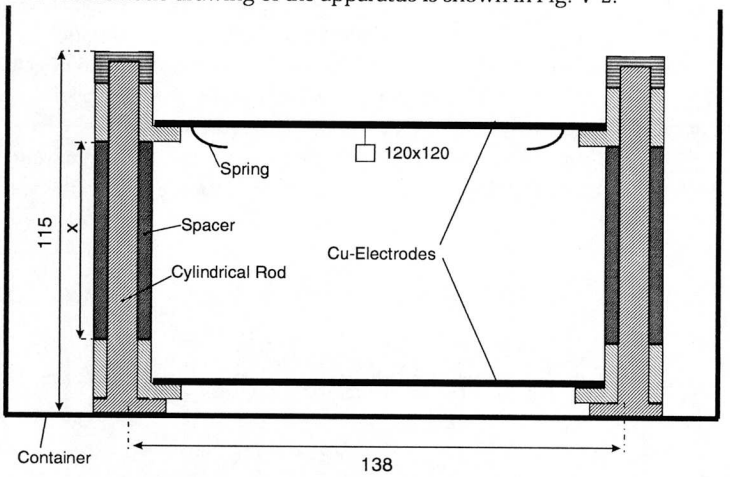

Fig. V-2: Schematic drawing of the EPD apparatus. The masses are given in mm. The plate distance can be varied using different spacers with length x (10,20,30,40,50 and 100 mm).

The substrate was fixed with springs on the top copper electrode thus avoiding any sedimentation effects. For some experiments a small apparatus was also utilized. Two copper electrodes 32x32 mm^2 were connected with plastic screws resulting in a plate distance of 10 mm. The substrate was fixed also on the top electrode.

A potentiostat[1] was used as power supply. Voltages between 0-100 V and currents between 0 and 2 A could be adjusted. The voltage was additionally controlled by a digital voltmeter[2]. The current flow between the electrodes was measured using a multimeter[3].

3.1.2 Substrate

The porous substrate consisted of a pre-sintered, tape-cast Ni-cermet precursor[4] described in more detail in chapter IV-5.2. Its microstructure is shown in Fig. V-3a. For the optimization of the deposition experiments, a cast Ni-cermet precursor tape with a thickness of 450 µm was chosen as substrate. Pre-sintering was performed at a temperature of 1100 °C for one hour at a heating ramp of 2 K/min.

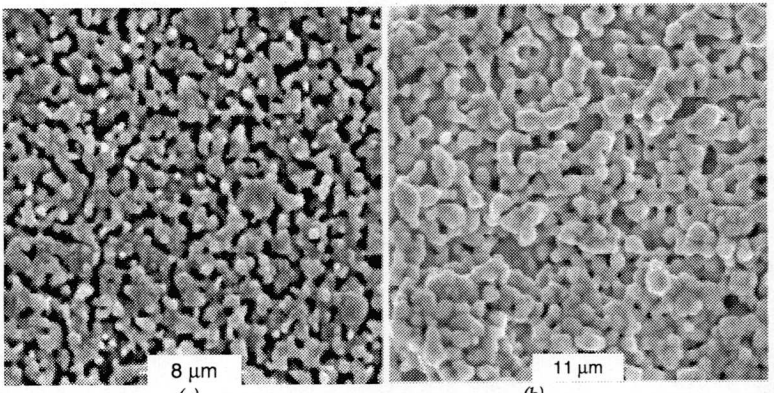

Fig. V-3: Microstructure of (a) the Ni-cermet precursor substrate (a) pre-sintered at 1100 °C for one hour, (b) the pressed LSM substrate, sintered at 1000 °C for one hour.

EPD experiments were also performed on pressed LSM substrates. The LSM powder[5] was mixed with a binder[6], pressed with 125 MPa to pellets with 20 mm in diameter, and pre-sintered at 1000 °C for one hour at a heating ramp of 1 K/min. Af-

---

[1] Heinzinger 100-2, Germany

[2] Keithley 197 A Autoranging Microvolt DMM

[3] Keithley 2000

[4] Ni-cermet precursor: mixture of NiO/CGO and TZP before reduction to the true Ni-Ce-Zr-oxide-cermet

[5] $La_{0.84}Sr_{0.16}Co_{0.02}MnO_{3-x}$, Rhône Poulenc, USA (as used in chapter IV-3.3.2)

[6] 10wt% Ceridust 3910, Hoechst, Germany

ter the deposition experiments the bilayer was sintered for one our at 1350 ℃ at a heating rate of 2 K/min. The microstructure of the sintered LSM is shown in Fig. V-3 b. In both cases pre-sintering was necessary to give the substrates a certain strength. As will be shown later, the pre-sintering temperature is very important to get a crack free, flat sintered EPD layer.
In addition, the electrical conductivity of the substrate plays an important role: One condition for EPD is that the used substrate has a conductive surface. By reducing the pre-sintered substrate prior the deposition process, the Ni-oxide in the substrate is reduced to metallic Ni. After the reducing treatment at 700 ℃ under H_2-gas the Ni-cermet tapes showed a conductivity of 10000 S/m. LSM is electrically conductive and required therefore no pre-treatment.

3.1.3 Suspension

The electrophoretic deposition can be performed in water-based suspensions as well as in organic media. When using water-based suspensions, the main problems are the contamination of the slip and the deposit, and the formation of gas bubbles due to the electrolysis of water. Therefore, ethanol based suspensions were used in this work. In contrast to the well understood stabilization mechanism of ceramic particles in water, the mechanisms in ethanol are not fully established. However, Wang [74] showed that the electrostatic stabilization of zirconia in ethanol involves three steps: (1) adsorption of ethanol molecules in undissociated form onto the basic surface sites of the oxide particles, (2) dissociation of the adsorbed ethanol molecules by hydrogen ions which migrate to the basic surface sites; and (3) desorption of $C_2H_5O^-$-anions into the solution, leaving the particles positively charged.

POWDER	ZrO_2 (ss) 3 mole % Y_2O_3 (TZP)
Supplier	Tosoh, Japan
Median Grain Size, d_{50}	0.23 µm
BET surface	16 m^2/ g
Lot #	Z804068P

Table V-2: Zirconia Powder used for the preparation of the EPD-suspensions

In this work 3 mole % yttria stabilized zirconia powder (TZP) was used as raw material for the preparation of the suspension used for electrophoresis. Properties of the powder such as median grain and specific surface area are given in Table V-2. Suspensions of TZP powder were prepared by mixing 100 g powder with 52 g

ethanol as solvent and 1.5 g polyethyleneimine[7] (PEI) as dispersant. PEI is a polyelectrolyte which absorbs onto the particle surface and additionally charges the particle. The mixture was filled in a polyethylene bottle with zirconia milling balls (diameter 5 mm) and was ball-milled for 24 hrs. After the milling process, the median grain size was 0.3 µm. The suspension was additionally ultrasonically treated for 5 minutes before each deposition process. An ultrasonic probe[8] was used with a 50% pulsed mode where pulses were emitted during 50% of the whole time.
ESA[9] measurements[10] of dispersed TZP particles in ethanol confirm the positive surface charge proposed by Wang. The ESA-value for a 2 vol. % suspension for zirconia particles in ethanol was 0.01 mPa·m/V. The absolute values of the particle charge in organic media are very low and can not be compared directly to those obtained in water. This is due do the fact that the measurement conditions (e.g. applied voltage, dielectric constant) are completely different.

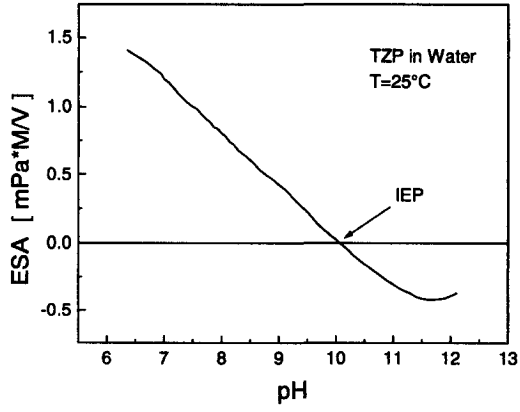

Fig. V-4: ESA curve of zirconia powder (TZP) suspended in water. The isoelectric point is at 10.

Since the ESA-curve of the zirconia powder in water is needed later to discuss the deposition process an ESA curve of 2 vol. % zirconia particles dispersed in water is shown in Fig. V-4. The isoelectric point (IEP) of the zirconia powder is at a pH of 10. Stable powder suspensions can be therefore prepared by adjusting the pH-value much more lower or higher than the IEP.

---

[7] Polyethyleneimine: Polysciences Inc. Warrington, PA, USA
[8] Sonics Materials Inc. Danbury, Connecticut, USA
[9] ESA: Electrokinetic sonic amplitude
[10] ESA 8000 System, Matec Applied Science, Hopkinton, MA, USA

3.2 Deposition Experiments

Unless otherwise noted the applied voltage for the large apparatus was 30 V, and 5 V for the small apparatus; the period of deposition time was three minutes in both cases. The distance between the electrodes was 50 mm for the large apparatus and 10 mm for the small apparatus. In this work zirconia layers were fabricated with thicknesses from 4-100 μm on LSM and Ni-CGO substrates.

3.2.1 Constant Voltage Experiments

Measurements of the Current

The following electrophoretic deposition experiments were carried out under constant voltage conditions. Fig. V-5 illustrates the measurements of the current between the electrodes at different constant voltages as a function of time. In each case, the measurable current decreases with time due to the shielding effect of the already deposited layer and the decreasing particle concentration in the suspension.

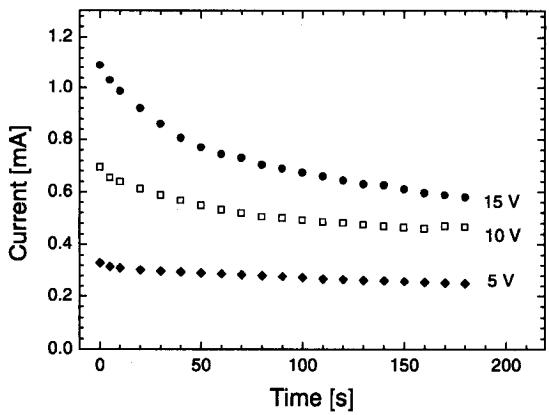

Fig. V-5: Measurements of the current between the electrodes during constant voltage experiments in the small apparatus.

Proton Concentration at the Deposition Electrode

During an EPD experiment using the large apparatus 1 ml of the suspension was taken from the deposition bath every minute. The samples were collected at different positions at the cell and diluted with 5 g water. Measurements of the pH of the suspensions were carried out using a combined pH glass electrode (Metrohm) and the results are given in Fig. V-6;

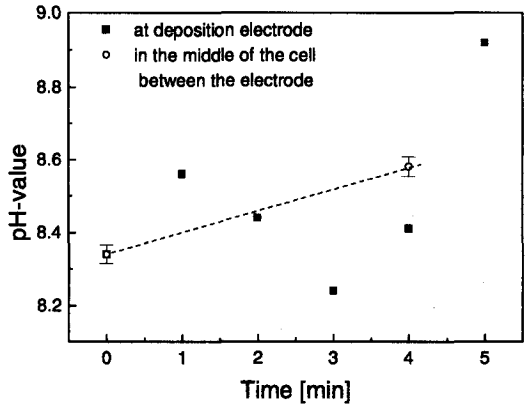

Fig. V-6: pH measurements at the deposition electrode. Point 1 marks the starting point with no electrical field. The applied voltage was 30 V at an electrode distance of 80 mm.

For comparison the pH value after four minutes was also measured in the middle of the suspension bath. The measurements were repeated three times with freshly prepared suspensions. At the beginning the pH in front of the deposition electrode is 8.35. After one minute of deposition time it increased to 8.6 to run through a minimum and then further increased to 8.9 after five minutes. In the middle of the cell the pH increases from 8.35 to 8.6 after four minutes. In summary, during the deposition process there is a pH gradient from more acaline at the deposition electrode to less alkaline in the center of the cell. This finding will be used later to explain the mechanism of the deposition process.

3.2.2 Dependence of Layer Thickness on EPD-Parameters

For practical applications it is desirable to predict the layer thickness using direct accessible EPD-parameters.

The thickness of the deposited layer is determined by the applied electrical field strength, the deposition time and by the specific properties of the suspension such as grain size of the ceramic powder, surface charge, pH and solids loading. Most work done so far on EPD used either an experimental or mathematical approach. Experiments were performed with different field strengths and deposition times and the layer thickness [40, 60, 75-78] or the ceramic mass deposited [40, 43, 56, 66, 67, 79-81] was measured after the deposition. Another method is to establish or use equations relating the yield of the ceramic mass to the different variables [40, 43, 82-87].

The aim of the following model evaluation is to relate the layer thickness using a kinetic model to the total charge passed through the cell. Thereby it is assumed that the ceramic particles are the only charge carriers. This neglects, that also the mobile counter-ions in the suspension are contributing to the current. However, in a steady state operation mode the latter species would only enter as a constant in the model. It is further assumed, that the concentration change of particles and counter-ions to the deposition is negligible versus time.

The deposited mass of particles is generally calculated using by means of the following equation [88]

$$\frac{dm(t)}{dt} = f \cdot A \cdot c_0 \cdot \upsilon_E \cdot E(t) \qquad \textit{Eq. V-1}$$

where m = deposited mass, t = deposition time, f = efficiency of the deposition (dimensionless), A = substrate surface, c_0 = solids loading of the suspension, υ_E= electrophoretic mobility, and E = electrical field.

In order to calculate properly the mass of deposited particles using Eq. V-1, the time-dependent change of the electrical field as a function of layer thickness must be known. However, this is very difficult to measure in practice (compare to appendix 3). Measurement of the applied voltage and current during the deposition is easier and was reported in literature: Hruschka [89] assumed that there are linear voltage drops across the suspension, across the already deposited layer and in the substrate. For the deposited layer thickness, $S(t)$, he derived the following equation:

$$S(t) \propto \frac{m}{A} = -C_1 + \sqrt{C_2^2 + C_1 \cdot t} \qquad \textit{Eq. V-2}$$

with the constants $C_1 = c_0 \cdot U_0 \cdot \dfrac{\zeta \cdot \varepsilon_L \cdot \varepsilon_S \cdot \varepsilon_0}{3 \cdot \eta \cdot (\varepsilon_L - \varepsilon_S)}$ and $C_2 = \dfrac{\left[d + D \cdot (\varepsilon_L - \varepsilon_A)\right] \cdot \varepsilon_S}{(\varepsilon_L - \varepsilon_S) \cdot \varepsilon_A}$

where $S(t)$ = thickness of the deposited layer, U_0 = applied voltage, ζ = zeta potential, η = viscosity of the suspension, ε_0 , ε_L and ε_S = dielectric constant in vacuum, dielectric constant of substrate, and dielectric constant of the suspension, respectively, D = thickness of the substrate, d = electrode distance.

Using the two parameters C_1 and C_2, it is possible to describe the relationship between layer thickness and the applied voltage and time. It is necessary also to know all the other parameters such as zeta potential and the dielectric constants

which can not be directly measured. However, the change in the solids loading is not considered.
Sarkar [40] derived an equation with takes into account this change in solids loading caused by the deposition:

$$\frac{dm}{dt} = m_0 \cdot k \cdot e^{-k \cdot t} \qquad \text{Eq. V-3}$$

with

$$k = \frac{f \cdot A \cdot v}{V} \qquad \text{Eq. V-4}$$

where m_0 = mass of the particles in the suspension, v = median velocity of a particle, V= volume of the suspension. The kinetic parameter k is very difficult to determine experimentally. Sarkar, also neglected the change in solids loading caused by sedimentation.

In this work, the particle transport in the suspension is treated as equivalent to the electrical current. The deposition rate can then be described as a function of the electrical current.

$$\frac{dm(t)}{dt} = \alpha \frac{m_T}{q_{eff}} I(t) \qquad \text{Eq. V-5}$$

where α = fraction of the particles which are deposited, m_T = median mass of a particle, q_{eff} = effective charge of a particle, I = current measured in the suspension. Integration of equation 1 and 4 yields the total deposit $m(t)$:

$$m(t) = f\, A\, c_0\, u_E \int E(t)\, dt = \alpha \frac{m_T}{q_{eff}} \int I(t)\, dt \qquad \text{Eq.V-6}$$

The integral of the current $I(t)$ gives the charge which has passed through a plane parallel to the electrode after a time t. This amount of charge, designated as Φ, is proportional to the deposited particle mass $m(t)$. The charge passed Φ can be calculated using the experimentally derived current values I:

$$\Phi = \int I\, dt = \sum I\, \Delta t \qquad \text{Eq. V-7}$$

Using Eq. V-2 (relationship between the weight of particles and the current) it can be written:

$$\Phi(U_0, t) = -C_2 + \sqrt{C_2^{\,2} + C_1\, U_0\, t} \qquad \text{Eq. V-8}$$

The current, I, is the derivative Eq. V-8:

$$I(U_0, t) = \frac{d\Phi}{dt} = C_1 \frac{U_0}{2} \left(C_2^{\,2} + C_1\, U_0\, t\right)^{-\frac{1}{2}} \qquad \text{Eq. V-9}$$

The following correlation was derived

$$S(U_0,t) \propto w(U_0,t) \propto \int I(U_0,t)dt \qquad \textit{Eq. V-10}$$

Hence it is possible to make predictions about the deposited layer thickness using equation V-9 and knowing the applied voltage and deposition time.

Using the a two parameter approach it was tried to fit the results of Fig. V-5 with Eq. V-9. The results are shown in Fig. V-7. The lines were calculated using the constants C_1 = 2.18·10-5 As/Ω and C_2 = 0.161 As for all three curves. The lines fit very well to the measured data. Therefore, it was demonstrated that the assumptions made above concerning the charge carriers is correct: The ceramic particles are the main charge carriers in an EPD experiment. Fig. V-8 shows the integrations of these measured data, the total charge Φ which has passed after a time *t*.

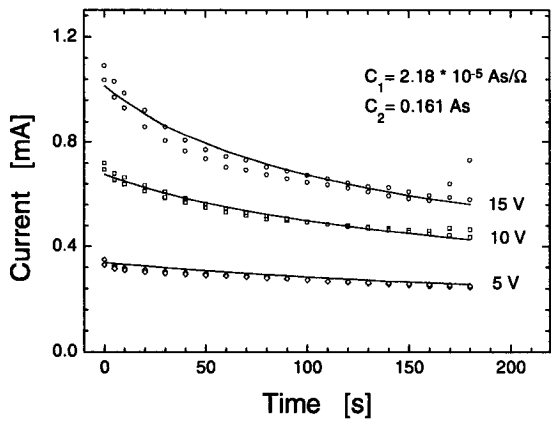

Fig. V-7: repeated results of measurements of the current between the electrodes during EPD experiments (Fig. V-5). The continuos lines are fitted according to Eq. V-9.

To check if this model can be used to predict layer thickness, EPD experiments were performed at different voltages and the resulting layer thicknesses after sintering was measured in the SEM. According to the model there should be a linear relationship between these two values. The results of the measurements of the layer thicknesses are shown in Fig. V-9. The error bars are due to the different layer thicknesses which are caused by the unevenness of the substrate surface. The straight line is a linear fit.

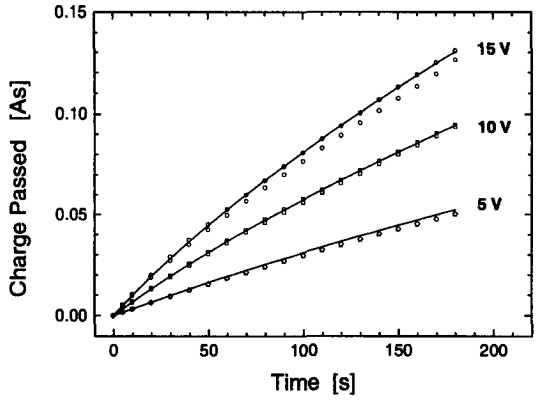

Fig. V-8: Dependence of charged passed on time. The curves were calculated by integration of the fitted curves of Fig. V-7.

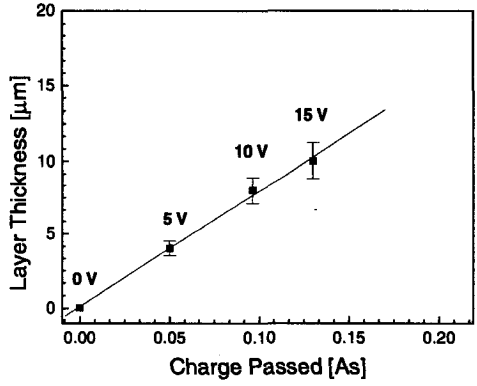

Fig. V-9: Dependency of passed charge vs. deposited layer thickness. The straight line is a linear fit.

This kinetic model can now be used to predict the layer thickness, knowing the applied voltage and time. However it is important to use a large enough amount of suspension to avoid changes of the solids loading.

A new *in-situ* method for the determination of the layer thickness during an EPD experiment, using an oscillating quartz, is presented in appendix 4. This method has the advantage that it is not influenced by changes in the solids content, viscosity or temperature in the suspension.

3.3 Drying and Sintering

After the deposition experiments the bi-layers were removed from the deposition cell and dried at room temperature for one day. For the measurements of the green density an EPD experiment was carried out using the large apparatus at a plate distance of 50 mm and an applied voltage of 30 V. After drying the samples were removed from the electrode. The green density of the zirconia layers was 55% TD[11].
The sintering properties of the substrate and of the deposited electrolyte had to be adjusted in order to a get crack-free and gas-tight product. Ideally, the two components used should exhibit not only an identical shrinkage, but also the same shrinkage rates during the whole sintering process. In Fig. V-10 the relative shrinkage of a dry pressed Ni-cermet precursor (green density at the beginning of the experiment 43% TD) and a dry pressed TZP sample (45% TD) is illustrated. Both materials showed different sintering onset-temperatures as well as shrinkage rates during the constant heating rate (3 K/min). Therefore, the sintering behavior of the two partners had to be fitted.

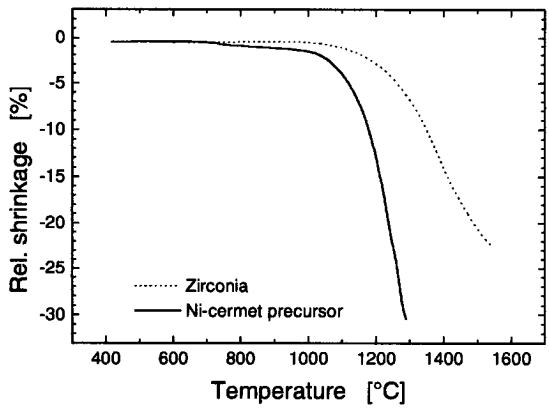

Fig. V-10: Sintering behavior of bulk zirconia and Ni-cermet precursor samples. Heating rate 3 K/min.

There are two possibilities for adjusting the sintering shrinkage: (1) The sintering shrinkage of the zirconia electrolyte can be decreased by calcination of the zirconia particles [89] and (2) the sinter properties of the anodic tape can be modified by pre-sintering. In this study changing the sintering properties of the tape by pre-sintering was chosen. In order to determine the shrinkage of the anode, tapes were

[11] Theoretical density of TZP: 6.01 g/cm^3

pre-sintered for one hour at different temperatures. The subsequent final sintering was aimed to take place at 1400 ℃ for one hour. The linear shrinkage after sintering is illustrated in Fig. V-11. Below a pre-sintering temperature of 1000 ℃ the shrinkage after final sintering at 1400 ℃ is almost constant because there is no sintering up to this temperature. Above 1000 ℃ pre-sintering temperature, the shrinkage starts to decrease in accordance with the dilatometer results (Fig. V-10). The shrinkage after a pre-sintering at 1350 ℃ is almost zero because the pre-sinter temperature is close to the final sintering temperature.

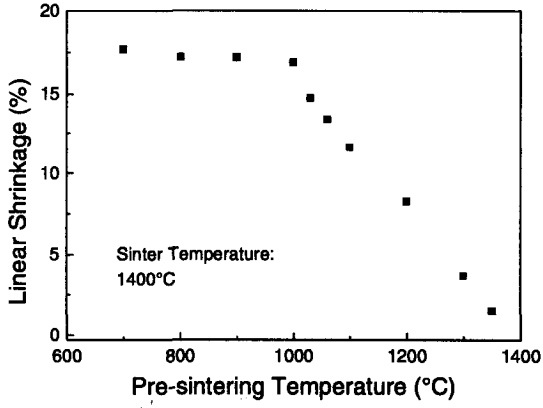

Fig. V-11: Shrinkage of Ni-cermet precursor tapes pre-sintered for one hour at different temperatures and subsequent final sintering at 1400 ℃ for one hour. The linear shrinkage shown occurred during the 1400 ℃ final sintering.

Fig. V-12 illustrates the sintering shrinkage and porosity change of anode tapes pre-sintered at 1100 ℃ and also of zirconia samples processed via electrophoretic deposition. Considering the sintering shrinkage of zirconia the sintering temperature of the two components should be 1400 ℃ or higher. The porosity of the anodic tapes decreases with increasing sinter temperature. For anode applications in SOFC the minimum porosity required is 30 vol. % [34]. Since the porosity is still high enough at a sinter temperature of 1400 ℃, this temperature was chosen for the sintering of the active anode and the electrolyte. Sintering of the bi-layer was performed at a heating rate of 1 K/min up to 1400 ℃, and a holding time of one hour.

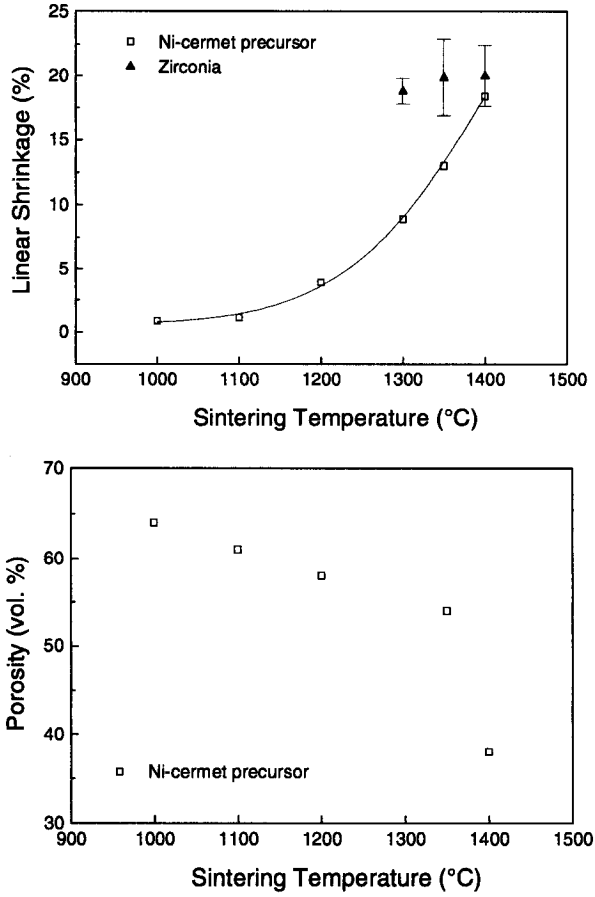

Fig. V-12: Shrinkage and porosity of anode tapes pre-sintered at 1100 °C after different sintering temperatures. The shrinkage of deposited zirconia electrolytes is included in the upper figure.

3.4 Layer Characterization

3.4.1 Optical Characterization

After sintering, the coated samples remained flat and did not show macrocracks. The micrographs of the sintered bi-layers Fig. V-13 and Fig. V-14 show good adhesion of the zirconia layer on the underlying substrate. The thickness of the electro-

phoretically deposited layer was 15 µm and remained constant across the whole substrate. The microstructure of the substrate was characterized by a fine grain size of 2 µm, that of the TZP layers by a grain size of 0.3 µm.

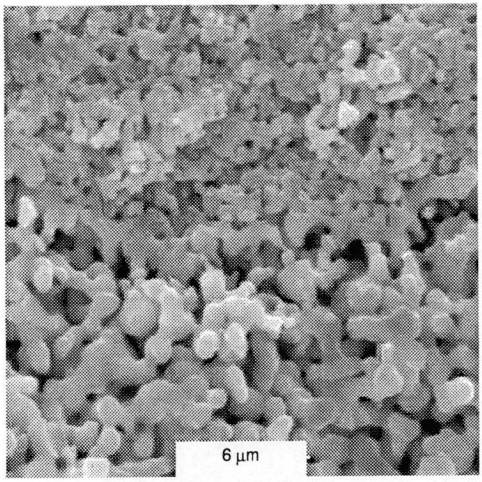

Fig. V-13: zirconia layer (top) and LSM substrate (bottom) after sintering. Plate distance 10 mm, applied voltage 5 V, 3 minutes.

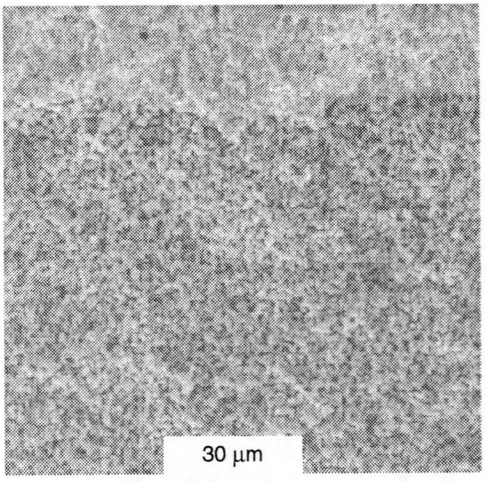

Fig. V-14: zirconia layer (top) and Ni-cermet precursor substrate (bottom) after sintering (plate distance 50 mm, applied voltage 30 V, 3 minutes).

3.4.2 Cell Measurements

The bi-layers produced were completed by sputtering platinum as cathode onto the anode-electrolyte bilayer. A Pt mesh[12] (1 cm x 1 cm) was used as current collector, attached to the electrodes with Pt paste[13] and fixed along the edges with a ceramic binder. Each platinum current collector was bonded to two platinum wires, one for the current and one for the voltage measurement. The wires were connected to the cell by electrical spot welding[14]. Alumina spacer rings were used on both sides to separate the gas rooms and were attached to the single PEN by a ceramic binder. The test cell was placed in a tubular furnace[15] and the gases were supplied through a quartz glass tube as schematically shown in Fig. V-15.

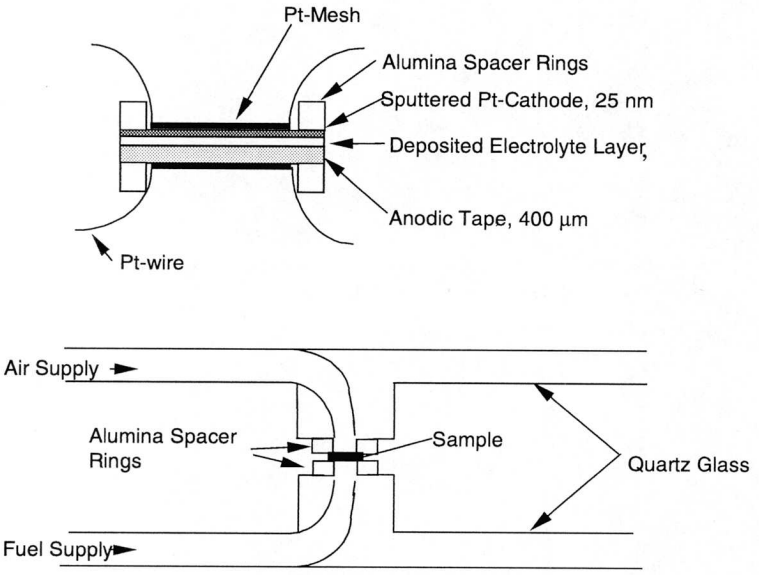

Fig. V-15: Schematic view of the sample used for the I-V measurements (upper image) and of the quartz glass sample holder (lower image).

Air was supplied to the cathode side and humidified (3%) H_2/N_2-mixture was used as fuel. The theoretical electromotoric force calculated from the Nernst equation at

[12] Pt mesh, Engelhard 52 mesh wire diameter 100 mm
[13] Pt, C 3650
[14] Resistronic 3201, Brügg, CH
[15] Gero, Neuhausen, FRG

these conditions is 1.03 V. The amount of gases was regulated by a gas flow meter. The cell current and voltage were measured with a digital multimeter[16] and regulated by a laboratory power supply. The test cells were heated to 700 ℃ and equilibrated at this temperature until they showed stable current and voltage. The open-circuit voltage, OCV which corresponds to E_{th}, (compare with chapter I) can be regarded as a measure of the quality of the electrolyte at a give oxygen chemical potential. An OC*V* close to the theoretical value means that the electrolyte is gas-tight.

Fig. V-16 shows typical current-voltage characteristics. The OCV of all samples tested did not reach the theoretical OCV estimated from the Nernst equation. Typical values were 0.9 V for 20 µm thick zirconia layers: This indicates that either none of the layers were gas-tight, or that the sealing of the test-cell was not perfect. (Checking of the electrolyte surfaces did reveal some cracking and pinholes).

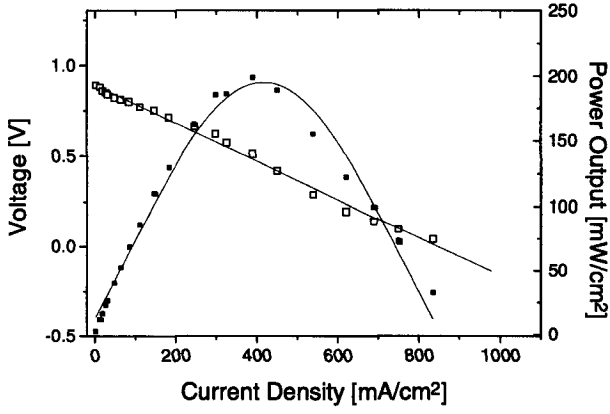

Fig. V-16: I-V characteristics of a PEN-element measured at 700 ℃: anode: Ni-cermet, electrolyte: EPD-zirconia layer, 20 µm, PT-cathode

3.5 General Discussion of the EPD-Process

Most reports on electrophoretic deposition found in the literature describe the deposition of ceramic suspensions onto electrically conducting electrodes or on metallic substrates [41, 55-57, 64, 68, 72, 75, 77, 83, 90-94]. Little information is available concerning the deposition on ceramic substrates [42-44, 89, 95]. In addition, for both techniques controversially discussions exist concerning the exact deposition

[16] Keithley 175 A

mechanism. In particular, the theories differ on the precise mechanism of how the charged particles come into contact with the electrode or an already deposited powder layer. Grillon [96] suggested particles undergo charge neutralization as they touch and deposit on the electrode. Shimbo [97] proposed secondary processes at the electrode producing hydroxides which adsorb on the particles and polymerize, holding them together in the deposit. Mizuguchi et al. [81] discussed the deposition of alumina particles from an acetone slurry containing nitrocellulose and a small amount of strong acid. They suggested a combination of the two mechanisms. Discharging of particles at the electrode brings them closer together so that nitrocellulose chains present at the particle surfaces could form bridges and cause coherence deposits. Koura [60] proposed the following deposition mechanism: charged particles in the suspension partially discharged at the deposition electrodes. The adsorbed H^+ ions of the following incoming particles move to the surface of the deposition electrodes by diffusing through small openings in the ceramic film and subsequently discharge with formation of gaseous H_2. Vanderperre [98] reported that there might be some discharge of particles at the electrode. El-Jazairi [99] stated that there is a strong dependency of the deposit layer density on the acidity of the suspension. He demonstrated that a pH-change of the suspension during the deposition occurs but he did not propose an explanation for this finding. Sarkar [40] proposed that the double layer around the tail of the ceramic particle becomes thinner so the incoming particles can approach each other closely enough. This means that van-der-Waals forces dominate the deposition process. For this reason, EPD is said to be a non-faradayic process.

At the moment, the exact deposition mechanisms at the electrode are not fully understood. We attempted to gain an understanding of electrochemical reactions at the deposition electrode in order to propose a model for the deposition for ethanol suspensions.

There are two conditions for a successful deposition:
The particles in the suspension must be transported to the deposition location and the particles must 'stick' to each other on the deposition place. If the particles in the suspension bear a surface charge, they always migrate towards the deposition location as long as the electrical field is strong enough. As we will see, the electrical properties of the substrate will play an important role. Hence, a suitable substrate for the deposition of positively charged zirconia particles has to be conductive (Fig. V-17(d)) or should have a negatively charged surface. In our first experiments, the Ni-cermet precursor substrates were non-conductive. ESA measurements of Ni-cermet precursor powder in ethanol (1 vol. %) gave a mobility value of $1.49*10^{-10}$ m^2/Vs indicating a positively charged surface. According to the deposition conditions the surface of the substrate had to be changed either to a negatively charged

surface by the application of specific adsorbing ions or to a conducting surface by reduction of the NiO to metallic Ni. In this work the Ni-O in the substrate was reduced to metallic Ni prior to the deposition process and therefore exhibited metallic conductivity. The electric field gradient corresponds to the situation (b) in Fig. V-17. The deposition of the positive charged zirconia particles was possible.

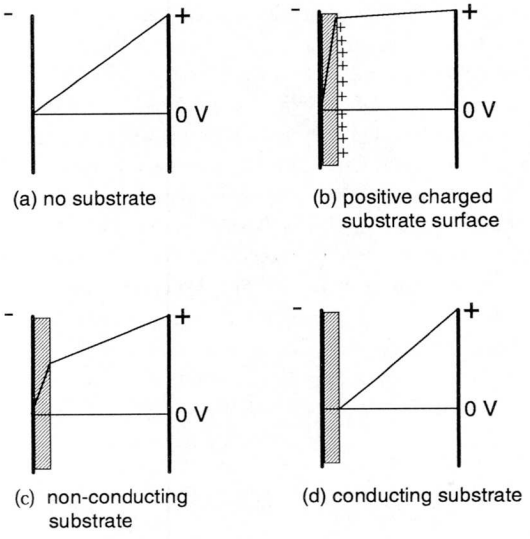

Fig. V-17: Course of the potential lines during the EPD process.

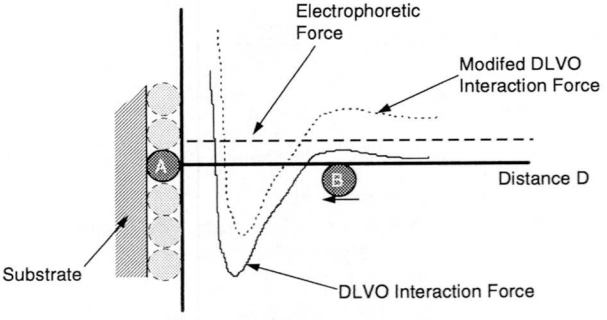

Fig. V-18: Schematic of the interactive forces between two particles during electrophoresis.

Let us now try to understand the deposition process: If the powder particles in the suspension bear a surface charge, they will always move towards the oppositvely charged electrode. The first incoming particles might discharge as soon as they touch the depositing electrode. The attractive Van-der-Waals forces will cause them to coagulate. However, there is no explanation why the following layers are able to stick to each other. Fig. V-18 shows the interaction force between two particles as a function of interparticle distance. If an external dc field is applied and particle A has reached the electrode, a second particle B can approach only if the applied field exerts a force greater than the mutual repulsive force.

Increasing the electrophoretic force by increasing the electrical field in the deposition cell is one possible method to overcome the repulsive potential barrier and enforce the deposition. However, deposition of thick layers takes place without any adjusting of the field strength. Therefore other mechanisms must be responsible for the deposition. They might be as follows: Besides positively charges particles there are always also negatively charged counter-ions ($H_2C_2O_5^-$) present in the suspension as well as positively charged co-ions (H^+). When the particles are migrating toward the negative electrode, the counter-ions migrate toward the positive electrode. Now, during the deposition, there is a change in the co- and counter-ion flow in the suspension: After a certain time, there might be less counter-ions at the negative deposition electrode.

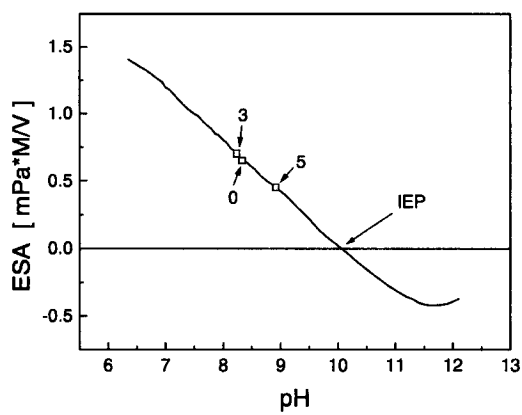

Fig. 19: ESA measurements of the EPD suspension; numbers correspond to the situations at the beginning of the deposition, after three and five minutes deposition time.

The particle surface is in equilibrium with the suspension. If the counter-ion concentration changes, the surface potentials of the particle also changes. Therefore,

the surface potentials of the particles vary with position. In addition there also must be a pH change in the suspension at the deposition electrode. The results of the pH measurements during an EPD experiment were already presented in Fig. V-6. After an initial increase the pH value decreased after 3 minutes due to the discharge of H^+ ions at the deposition electrode which was then followed by a constant increase of the pH-value. The following H^+-ions can not completely discharge because the layer already built up hinders the H^+ diffuse to the electrode. The first decrease can be explained by the fact, that not only the positively charged ceramic particles move to the deposition electrode but also the positive co-ions (H^+). These positively charged co-ions will recombine with e.g OH^- -ions or with H^+-ions to form H_2O or H_2. Thus, the overall pH-value in the suspension is increased as well, due to the generally lowered amount of H^+ ions.

The coagulation of the zirconia particles can now be explained. Fig. V-4 shows the surface charge of the zirconia particles at different pH values. The numbers in the figure correspond to situations at the beginning of the deposition, after three minutes and after five minutes deposition time. The particles show a decreased surface charge after five minutes deposition time compared to the starting point 0. The surface charge varies with the position and the time. Hence, the force which is necessary to overcome the DLVO interaction force (Fig. V-18) is lowered and the deposition of the next layers of ceramic particles can take place. This process is limited to diffusion. With an increasing thickness of the layer the diffusion path for the H^+-ions is longer, the surface charge is decreased and the repulsive force is too large to allow any further deposition.

Using the explanations given above, an electrode reaction model for the deposition of charged ceramic particles according to Fig. V-20 might be proposed. The charged particles and the co- and counter-ions are homogeneously distributed in the suspension (a). With the application of a dc-field, the particles and the co-ions migrate toward the oppositely charged electrode. As soon as the incoming ceramic particles touch the electrode there is a partial discharge. The adsorbed H^+-ions will diffuse through openings in the layer and will discharge to form H_2-gas or recombine with the counter-ion to form C_2H_5OH. These free H^+-ions together with the counterions are responsible for the increase of the pH-value. The then following decrease of the pH value is due to the lower amount of H^+-ions in the solution. The charge transfers occur on the negative deposition electrode and the rate limiting step of the deposition arises from a diffusion process of H^+-ions desorbed from the oxide particles through openings in the ceramic layer toward the electrode. These findings correspond very well with those of Koura et al. [100] and El-Jazairi [99].

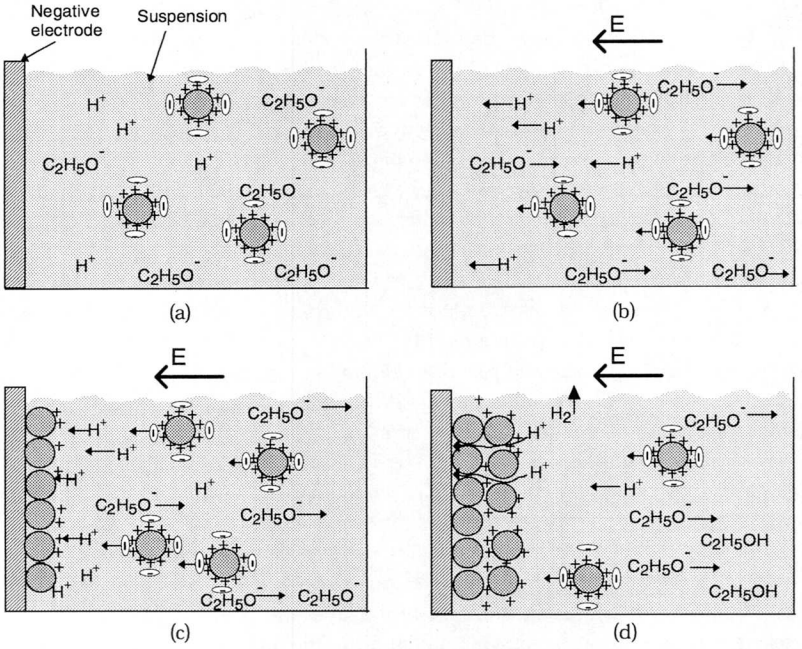

Fig. V-20: Schematic illustration of the deposition process:
(a) charged zirconia particles (grey spheres) and crowed C_2H_5O-counter-ions in the suspension without an electrical field, co- and counter-ions, H^+ and $C_2H_5O^-$, are homogeneously distributed in the suspension,
(b) with the application of a dc-field, the particles and the co-ions migrate to the oppositely charged electrode,
(c) zirconia particles deposit on the electrode and are partly discharged, pH decreases due to the local depletion of H^+-ions
(d) recombination of H^+-ions to H_2, and of H^+-ions with $C_2H_5O^-$-ions to ethanol. pH increases due to the local depletion of H^+-ions.

4 Summary

The suspension used for the electrophoretic deposition experiments contained 3 mol% Y_2O_3 stabilized zirconia in pure ethanol, with a median grain size of 0.3 µm after milling. The electrophoretic deposition method was successfully applied to

pre-sintered Ni-cermet and LSM substrates. Layers ranging from 4-100 µm in the thickness in the sintered state were fabricated.

The apparatus for the electrophoretic deposition had to be designed that a homogenous deposition was possible. The homogeneity of the electrical field is one of the main conditions for a successful deposition process. Based on two-dimensional field measurements and calculations using the formulation of Maxwell (given in appendix 3) the plate size was chosen as 12x12 cm using a 2 mm thick copper plate, with a maximum plate distance of 80 mm of no more than 5% deviation from the homogenous electrical field.

The substrate plays an important part in the deposition process. A successful deposition of the positively charged zirconia particles is only possible on substrates having negatively charged surfaces or with an electrically conducting substrate. The NiO-CGO substrates used were made highly conductive by reducing the NiO to metallic nickel. It was demonstrated that the deposition process is a combination of a charge-transfer and a diffusion process. After anincrease of the pH at the beginning of the electrophoresis the pH of the suspension decreased but then increased with continuing deposition. This behavior was explained by a concentration change of the H^+-ions in the suspension. An electrode reaction model for the deposition of charged ceramic particles was proposed. The stability of the suspension decreases in the electrode area, the suspension being shifted to its isoelectric point by the local change in pH.

A suggested kinetic model for the deposition process did not violate the observed parameters. It could be shown that there is a linear relationship between the total transported electric charge and the thickness of the deposited layer. This kinetic model can therefore be used to predict the layer thickness, knowing the applied current and duration.

The sintering properties of the substrate and of the deposited electrolyte were successfully adjusted to achieve crack-free and dense composites. The NiO-precursor tapes, pre-sintered at 1100 °C, exhibited the same shrinkage as the electrophoretic deposited zirconia layers. Although the produced PEN elements with EPD electrolyte layers did not exhibit the theoretical OCV-value, an acceptable cell performance was achieved at 700 °C with a 15 µm thick zirconia layer. Therefore, the EPD-process seems to be a promising method for the production of thin, dense electrolytes.

5 References

[1] S. A. Barnett, "A New Solid Oxide Fuel Cell Design Based on Thin Film Electrolytes", *Energy*, **15**, 1, pp. 1-9, 1990.

[2] B. H. Steele, "State-of-the Art SOFC Ceramic Materials", First European SOFC Forum, Luzern, Switzerland, U. Bossel Ed., Fuel Cell Forum, Oberrohrdorf, Switzerland, pp. 375-399, 1994.

[3] M. Agarwal, M. R. De Guire, and A. H. Heuer, "Synthesis of ZrO_2 and Y_2O_3-Doped ZrO_2 Thin Films Using Self-Assembled Monolayers.", *J. Am. Ceram. Soc.*, **80**, pp. 2967-2981, 1997.

[4] H. Arai, K. Eguchi, T. Tetoguchi, and R. Yamaguchi, "Fabrication of YSZ Thin Film on Electrode Substrate and its SOFC Characteristics", Third Internat. Conference on SOFC, Hawai, S.C. Singhal, H. Iwahara, Ed. The Electrochem Soc., pp. 167-174,1991.

[5] C. C. Chen, M. M. Nasrallah, and H. U. Anderson, "Synthesis and Characterization of YSZ Thin Film Electrolytes", *SSI*, **70/71**, pp. 101-108, 1994.

[6] Q. Gao, E. Rocheleau, and B. Liaw, "Thin Film Tetragonal Doped Zirconia: Synthesis and Characterization", 3rd Int. Symp. on SOFC, New York., pp. 38-47, 1993.

[7] E. M. Kelder, O. C. J. Nijs, and J. Schoonmann, "Low-Temperature Synthesis of Thin Films of YSZ and $BaCeO_3$ Using Electrostatic Spray Pyrolysis", *SSI*, **68**, pp. 5-7, 1994.

[8] K. A. Murugesamoorthi, S. Srinivasan, D. L. Cocke, and A. J. Appleby, "Novel Approaches for Fabrication of Thin Film Layers for Solid Oxide Electrolyte Fuel Cells", 25th Intersociety Energy Conversion Engineering Conference, AIChE, New York, USA, pp. 246-250,1990.

[9] K. Nord-Varhaug, C. Chen, E. M. Kelder, Van Berkel P. F., and J. Schoonman, "Thin Film Techniques for Solid Electrolyte Composites", 2nd Europ. SOFC Forum, Oslo, Norway, B. Thorstensen, Ed. pp. 331-340, 1996.

[10] K. Honegger, E. Batawi, C. Sprecher, and R. Diethelm, "Thin Film Solid Oxide Fuel Cell (SOFC) for Intermediate Temperature Operation", SOFC V, Aachen, Germany, U. Stimming, S.C. Singhal, H. Tagawa, W. Lehner, The Electrochemical Society, pp. 321-325, 1997.

[11] T. Setoguchi, K. Eguchi, and H. Arai, "Thin Film Fabrication of Stabilized Zirconia for Solid Oxide Fuel Cells", *Vacuum*, **42**, 16, p.1601, 1991.

[12] S. d. Souza, S. J. Visco, and L. C. Jonghe, "Reduced-Temperature Solid Oxide Fuel Cell Based on YSZ Thin-Film Electrolyte", *J. Electrochem. Soc.*, **144**, pp. L35-L37, 1997.

[13] P. K. Srivastava, T. Quach, Y. Y. Duan, R. Donelson, S. P. Jiang, F. T. Ciacchi, and S. P. S. Badwal, "Thin Film Solid Oxide Fuel Cells Prepared by DC Magnetron Sputtering for Intermediate Temperature Operation" in [9] pp. 761-772,1996.

[14] V. E. J. van Dieten and J. Schoonman, "Thin Film Techniques for Solid Oxide Fuel Cells", *SSI*, **57**, pp. 141-145, 1992.

[15] S. J. Visco, C. Jacobson, and D. J. L.C, "Fabrication and Performance of Thin Film- SOFC" in [9] pp. 710-717

[16] N. Q. Minh and T. Takehiko, "Science and Technology of Ceramic Fuel Cells", Amsterdam: Elsevier, pp. 70-90, 1995.

[17] T. A. Ring, "Fundamentals of Ceramic Powder Processing and Synthesis", San Diego, USA: Academic Press, pp. 629-631, 1996

[18] R. Fries and B. Rand, "Slip-Casting and Filter-Pressing," in *Materials Science and Technology, Processing of Ceramics, II*, vol. 17A, R. J. Brook, Ed. Weinheim: VCH, 1996, pp. 153-189.

[19] L. Svarovsky, "Solid-Liquid Separation", Boston, USA: Butterworths, pp. 211-220, 1977.

[20] T. Uchikoshi, Y. Sakka, K. Ozawa, and K. Hiraga, "Pressure Filtration and Sintering of Fine Zirconia Powder", *J. Europ. Ceram. Soc.* **5**, 669-674, 1998.

[21] R. E. Mistler, D. J. Shanefield, and R. B. Runk, "Tape Casting of Ceramics" in *Ceramic Processing before Firing*, G.Y. Onoda, L.L Hench, Ed., J. Wiley Sons. N.Y., pp. 411-449, 1978.

[22] R. E. Mistler, D. J. Shanefield, and R. B. Runk, "Tape Casting of Ceramics" in *Ceramic Processing before Firing*, G.Y. Onoda, L.L Hench, Ed., J. Wiley Sons. N.Y., p. 411,1978.

[23] E. P. Hyatt, "Making Thin Flat Ceramic - a Review", *Am. Ceram. Soc. Bull,*. **65**, pp. 637-638, 1986.

[24] R. J. Brook, "Processing of Ceramics Part I" in *Materials Science and Technology, A Comprehensive Treatment*, **17A**, R. W. Cahn, P. Haasen, and E. J. Kramer, Eds., VCH, pp. 410-430, 1996.

[25] C. J. Brinker and G. W. Scherer, "*Sol-Gel Science*", Academic Press, pp. 795-797, 1990.

[26] H. K. Anderson and M. M. Nasvallah, "Characterization of Oxides for Low Temperature SOFC", Gas Research Institute, London, pp. 101-111, 1991.

[27] C. C. Chen, M. M. Nasrallah, and H. U. Anderson, "Synthesis and Characterization of YSZ Thin Film Electrolytes," *SSI*,. **70/71**, pp. 101-108, 1994.

[28] W. H. Rhodes, Agglomerate and Particle Size Effects on Sintering Yttria-Stabilized Zirconia, *J. Am. Ceram. Soc.*, **64**, pp. 19-22, 1981.

[29] T. W. Kueper, J. V. Steven, and L. C. De Jonghe, "Thin Film Ceramic Electrolytes Deposited on Porous and Non-Porous Substrates by Sol-Gel Techniques", *SSI*, **52**, pp. 251-259, 1992.

[30] L. C. Klein, *Sol-Gel Technology for Thin Films, Fibers, Preforms, Electronics and Specialty Shapes*. New Jersey, USA: Noyes Publications, 50-79, 1988.

[31] S. d. Souza, S. J. Visco, and L. C. Jonghe, "Reduced Temperature Solid Oxide Fuel Cell Based on YSZ Thin Film Electrolyte," *J. Electrochem. Soc.*, **144**, pp. L35-37, 1997.

[32] K. Eguchi, T. Setoguchi, T. Inoue, and H. Arai, "Fabrication and Evaluation of Flat Thick Film Type SOFC", *SSI*, **37**, pp. 217-221, 1990.

[33] K. Murata and M. Shimotsu, "Fabrication and Evaluation of Electrode-Supported Planar SOFC", *Denki Kagaku*, **1**, pp. 38-43, 1996.

[34] N. Q. Minh and T. Takehiko, "Science and Technology of Ceramic Fuel Cells," Amsterdam: Elsevier, 1995, pp. 70-90.

[35] K. Kordesch and S. G., *Fuel Cells and Their Application*, VCH, pp. 146-147, 1996

[36] M. Cassidy, K. Kendall, and G. Lindsay, "Lower Temperature SOFCs Utilizing Screen Printed Electrolytes", in [9] pp. 667-676, 1996.

[37] M. Prica, K. Kendall, and M. Painter, "Transfer Printing of Thin Electrolyte Layers in Solid Oxide Fuel Cells.", SOFC IV, Yokohama, Japan, M. Dokiya, O. Yamamoto, H.Tagawa, S.C. Singhal, Eds. pp. 1056-1061,1995.

[38] H. Hellebrand, "Tape Casting," in *Materials Science and Technology, Processing of Ceramics, II*, **17A**, R. J. Brook, Ed. Weinheim: VCH, 1996, pp. 189-267.

[39] H. Taira, S. Sakamoto, H. Nakai, S. Towata, H. Takagi, and Y. Sakabe, "Development of Cofired Type Planar SOFC in [10], pp. 167-170, 1997.

[40] P. Sarkar and P. S. Nicholson, "Electrophoretic Deposition (EPD): Mechanism, Kinetics, and Application to Ceramics", *J. Am. Ceram. Soc.*, **79**, pp. 1987-2002, 1996.

[41] T. Tsuda, "Electrophoretic Forming of Ceramics" in *Electric Field Applic. in Chromat. Indust. Chem. Proc.*, VCH, pp. 12-19, 1995.

[42] T. Ishihara, K. Sato, K. Mizuhara, and Y. Takita, "Preparation of Yttria-Stabilized Zirconia Film for Solid Oxide Fuel Cells by Electrophoretic Deposition Method", *Chem. Lett.*, pp. 943-946, 1992.

[43] T. Ishihara, K. Shimose, T. Shiomitsu, and Y. Takita, "Electrophoretic Deposition of Y_2O_3-Stabilized ZrO_2 on the Porous $La_{0.8}Sr_{0.2}$ MnO_3 Cathode Substrate for SOFC" , in [37] pp. 334-343, 1995.

[44] T. Ishihara, K. Sato, and Y. Takita, "Electrophoretic Deposition of Y_2O_3 Stabilized ZrO_2 Electrolyte Film in Solid Oxide Fuel Cells", *J. Am. Ceram. Soc.*, **79**, pp. 913-919, 1996.

[45] A. M. El-Sherik, P. Sarkar, and A. Petric, "Electrophoretic Deposition of Lanthanum Gallate Solid Electrolyte Coatings on Cathode Substrates", The 1997 Joint Internat. Meeting, Paris, The Electrochem. Soc., p. 2564, 1997.

[46] F. F. Reuss, "Notice sur un Nouvel Effet de l'Electricite Galvanique", *Philips Res. Rep.*, **1**, p. 215, 1809.

[47] S. E. Sheppart, "The Electrical Deposition of Rubber", *Trans. Am. Electrochem. Soc.*, **52**, pp. 47-82, 1927.

[47] J. H. DeBoer, "Electrodeposition of a Thin Layer of Powdered Substances", *Rec. Trav. Chem.*, **58**, pp. 662-665, 1939.

[48] A. S. Berkmann, "Elektrophorese zur Herstellung von Porzellantiegeln", *Tr. Keram. Inst.*, **20**, p. 6, 1948.

[49] M. Melvin, "*Electrophoresis*", John Wiley & Sons, pp. 7-15, 1987.

[51] G. L. Dvornichenko, Y. V. Nizhnik, T. V. Slavikovskij, and L. V. Nikolajchuk, "Deposition of Polymer Dispersions for the Purpose of Producing Protective Coatings on Metals", *Kolloidnyi Zhurnal*, **55**, pp. 45-49, 1993.

[52] M. J. Shane, J. B. Talbot, C. Ross, E. Sluzky, and K. R. Hesse, "Electrophoretic Deposition of Phosphors I. Conductivity and Zeta Potential Measurements", *Coll. Interface Sci.*, **165**, pp. 325-333, 1994.

[53] T. V. Myasnikova, A. K. Krivtsov, V. E. Myasoedov, V. I. Piskarev, and Kosobokov-Y.A., "Effect of a Pulsed Current on the Properties of Cathophoresis Coatings", *Prot. Met.*, **25**, pp. 705-707, 1990.

[55] L. M. Apininskaya and V. V. Furman, "Electrophoretic Deposition of Coatings (a Literature Review)", *Soviet Powder Metall. Metal-Ceram.*, **12**, 2, pp. 61-64, 1973.

[56] S. N. Heavens, "Manufacture of Beta Alumina Shapes by Electrophoretic Deposition", *Proceed. Brit. Ceram. Soc.*, **38**, pp. 119-126, 1986.

[57] J. H. Kennedy and A. Foissy, "Fabrication of Beta-Alumina Tubes by Electrophoretic Deposition from Suspensions in Dichlormethan", *J. Electrochem. Soc.*, **122**, pp. 482-486, 1975.

[58] H. G. Krüger and H. Wittwer, "Elektrophorese" in *Technische keramische Werkstoffe*, J. Kriegesmann, Ed. , ch. 3.4.11.0, pp. 1-23, DKG, 1997.

[58] K. G. Herd, Salasoo L., E. Laskaris, R. A. Ranze, C. G. King, P. Haldar, and J. O. Hoehn, "Development and Fabrication of a Bi-2223 Racetrack Coil for Generator Applications", *IEEE-Transact. Appl. Supercond*, **7**, pp. 51-534, 1997.

[59] N. Koura and H. Shoji, "Preparation of High-Tc Superconductors by Electrophoretic Deposition Method", *Physica C 190*, **1-2**, pp. 163-164, 1991.

[60] N. Koura and H. Shoji, "BSCCO Superconductor Coating by the Electrophoretic Deposition Method", *Physica C 200*,. **1-2**, pp. 50-54, 1992.

[61] H. S. Maiti, S. Datta, and R. N. Basu, "High-Tc Superconductor Coating on Metal Substrates by an Electrophoretic Technique", *J. Am. Ceram. Soc.*, **72**, pp. 1733-1735, 1989.

[62] R. Flukiger, R. E. Gladyshevskii, and E. Bellingeri, "Methods to Produce Tl(1223) Tapes with Improved Properties ", *J. Superconduc.*, **11**, pp. 23-26, 1998.

[63] E. Bellingeri, R. E. Gladyshevskii, and R. Flukiger, "Textured Tl(1223)/Ag Tapes Prepared by Electrophoretic Deposition", *J. Superconduct.*, **11**, pp. 77-78, 1998.

[64] R. Fischer, E. Fischer, G. Portu, and E. Roncari, "Preparation of Ceramic Micro-Laminate by Electrophoresis in Aqueous System", *J. Mat. Sc. Lett.*, **14**, pp. 25-27, 1995.

[65] P. S. Nicholson, P. Sarkar, and X. Haung, "Electrophoretic Deposition and its Use to Synthesize ZrO_2/Al_2O_3 micro-laminate ceramic/ceramic composites", *J. Mat. Sc.*, **28**, pp. 6274-6278, 1993.

[66] P. Sarkar, X. Haung, and P. S. Nicholson, "Electrophoretic Deposition and its Use to Synthesize YSZ/Al_20_3 Micro-Laminate Ceramic/Ceramic Composites", *Ceram. Engin. Sci. Proc.* **14**, 9-10, pp. 707-716 ,1993.

[67] L. Vandeperre and O. Van Der Biest, "SiC-Graphite Laminates Shaped by EPD", *J. Ceram. Am. Bull.*, **77**, 1, pp. 53-58, 1998.

[68] J. M. Andrews, A. H. Collins, D. C. Cornish, and J. Dracass, "The Forming of Ceramic Bodies by Electrophoretic Deposition", *Proc. Br. Ceram. Soc.*, **12**, pp. 211-229, 1969.

[72] D. R. Brown and F. W. Salt, "The Mechanism of Electrophoretic Deposition", *J. Appl. Chem.*, **15**, pp. 40-48, 1965.

[73] K. A. Egerer and G. Landsberg , "Electrophorese und Electrosedimentation in nichtwässerigen Suspensionen", *Ges. Physik. Chemie*, **59**, pp. 207-222, 1955.

[71] M. S. J. Gani, "Electrophoretic Deposition - A Review", *Industrial Ceramics*, **14**, pp. 163-174, 1994.

[72] S. N. Heavens, "Electrophoretic Deposition as a Processing Route for Ceramics" in *Advanced Ceramic Processing and Technology*, 1, J. G. Binner, Ed., Noyes Publ., pp.255-286, 1980.

[73] M. Melvin, *Electrophoresis,*. John Wiley & Sons, p. 6, 1987.

[74] G. Wang, P. Sarkar, and P. Nicholson, "Influence on Acidity on the Electrostatic Stability of Alumina Suspensions in Ethanol", *J. Am. Ceram. Soc.*, **80**, pp. 965-972, 1998.

[75] P. Sarkar, C. Haung, and P. S. Nicholson, "Structural Ceramic Microlaminates by Electrophoretic Deposition," *J. Ceram. Soc.*, **75**, pp. 2907-2909, 1992.

[76] B. Ferrari and R. Moreno, "Electrophoretic Deposition of Aqueous Alumina Slips", *J. Europ. Ceram. Soc.*, **17**, pp. 549-556, 1997.

[77] B. Ferrari and R. Moreno, "Electrophoretic Deposition of Aqueous Alumina Slips," *J. of the Europ. Ceram. Soc.*, **17**, pp. 549-556, 1997.

[78] F. Harbach and H. Nienburg, "Homogeneous Functional Ceramic Components through Electrophoretic Deposition from Stable Colloidal Suspensions II. Beta Alumina and Concepts for Industrial Production," *J. Europ. Ceram. Soc.*, **18**, pp. 685-692, 1998.

[79] T. Ishihara, T. Kudo, H. Matsuda, Y. Mizuhara, and Y. Takita, "Electrophoretic Deposition of Stabilized Zirconia for Solid Oxide Fuel cells", in [4], pp. 334-343 ,1993.

[80] R. Nass, W. Storch, H. Schmidt, F. Harbach, R. Neeff, and H. Nienburg, "Electrophoretic Deposition of Alumina from Non-Aqueous Dispersions", Powder Processing Science, Berchtesgaden, Germany, DKG, H. Hausner, G.L. Messing, Ed., pp.625-632 ,1988.

[81] J. Mizuguchi, K. Sumi, and T. Muchi, "A Highly Stable Nonaqueous Suspension for the Electrophoretic Deposition of Powdered Substances.," *J. Electrochem. Soc.*, **130**, pp. 1819-1825, 1983.

[82] J. Mizusaki, K. Amono, S. Yamauchi, and K. Fueki, *SSI*, **22**, pp. 323, 1987.

[83] Y. H. Zhang, Z. Jiang, "Electrophoretic Deposition Forming of SiC-TZP Composites in a nonaqueous Sol Media," *J. Am. Ceram. Soc.*, **77**, pp. 1946-1949, 1994.

[84] Z. Zhang, Y. Huang, and Z. Jiang, "Reply to "Comment on Electrophoretic Deposition Forming of SiC-TZP Composites in a Nonaqueous Sol Media"," *J. Am. Ceram. Soc.*, **78**, pp. 3167-3168, 1995.

[85] P. Sarkar and P. Nicholson, "Comments on "Electrophoretic Deposition Forming of Sic-TZP in a Nonaqueous Sol Media"," *J. Am. Ceram. Soc.*, **78**, pp. 3165-3166, 1995.

[86] A. Sussmann and T. J. Ward, "Electrophoretic Deposition of Catings from Glass Isopropanol Slurries," *RCA Review*, **42**, pp. 178-197, 1981.

[87] L. J. Vandeperre and O. Van der Biest, "Electric Current and Electric Field for Electrophoretic Deposition from Non-Auqueous Suspensions," *Ceram. Trans.*, **85**, 1997.

[88] H. C. Hamaker and E. K. W. Verwey, "The Role of The Forces Between the Particles in Electrodeposition and other Phenomena," *Philipps Res. Rpts,*. **1**, pp. 181-185, 1939.

[89] M. K. M. Hruschka, "Entwicklung der elektrophoretischen Beschichtung für die Herstellung dünner Elektrolytschichten", Ph.D. Thesis, Report No. 3221,. Jülich, Germany, 1996

[90] P. S. Nicholson, P. Sarkar, and X. N. Huang, "Potentially Strong and Tough ZrO_2 based Ceramic Composites by Electrophoretic Deposition", Zirconia V,

Melbourne, Australia, Technomic Publishing Company, Inc., pp. 502-516, 1993.

[91] B. Ferrari and R. Moreno, "Zirconia Coatings onto Nickel Electrodes by Aqueous Electrophoretic Deposition", Ceramic Processing 1997, St. Barbara, USA, 1997.

[92] F. Harbach and H. Nienburg, "Homogeneous Functional Ceramic Components through Electrophoretic Deposition from Stable Colloidal Suspensions I. Basic Concepts and Application to Zirconia," *J. Europ. Ceram. Soc.*, **18**, pp. 675-683, 1998.

[93] R R. Clasen, "Keramische Formgebung durch elektrophoretische Abscheidung durch wäßrige Suspensionen: Grundlagen und Anwendung", Formgebung aus Suspensionen, Bayreuth, Germany, DKG, pp. 139-155, 1996.

[94] A. Brandstädter-Springer, F. Harbach, H. Nienburg, and L. Weiler, "Elektrophorese-Ein modernes Verfahren für Hochleistungskeramiken", DKG Jahrestagung, Bayreuth, DKG, Germany, pp .45-51 ,1992.

[95] J. Laubersheimer, Ritzhaupt H.-J., J. Hausselt, and G. Emig, "Electrophoretic Deposition of Sol-Gel Ceramic Microcomponentes Using UV-Curable Alkoxide Precursor," *J. Europ. Ceram. Soc.*, **18**, pp. 255-260, 1998.

[96] F. Grillon, D. Fayeulle, and M. Jeandin, "Quantitave Image Analysis of Electrophoretic Coating," *J. Mater. Sc. Lett.*, vol. 11, pp. 272-275, 1992.

[97] M. Shimbo, K. Tanzawa, M. Miyakawa, and T. Emoto, "Electrophoretic Deposition of Glass Powder for Passivation of Hig-Voltage Transistors," *J. Electrochem. Soc.*, vol. 132, pp. 389-398, 1985.

[98] L. Vanderperre, K.U. Leuven, The Netherlands, "Personal Communication", 1997.

[99] B. El-Jazairi, D. White, and J. P. Roberts, "On Electrohoretic Deposition of Alumina from Non-Aqueous Suspension", 9th Conf. on Science of Ceramics, Noordwigkerhout, The Netherlands, pp. 46-53,1977.

[100] N. Koura, T. Tsukamotoa, H. Shoji, and T. Hotta, "Preparation of Various Oxide Films by an Electrophoretic Deposition Method: A Study of the Mechanism," *J. Jpn. Appl. Phys.*, **34**, pp. 1643-1647, 1995.

VI Outlook and Further Work

1 PEN-Design

Processing of thin zirconia layers via electrophoresis was one of the aims of this work. It turned out that the used Ni-cermet precursor substrates had to be reduced to get a conductive substrate which can be used for deposition. The reduction causes an increase of the porosity and the substrates were quite brittle after this treatment. As mentioned in the introduction of this work, there are two possibilities of building-up a PEN structure: starting from the anode side, as performed in this work, or starting from the cathode side using LSM or other cathode materials such as LSCF (e.g. $La_{1-x}Sr_xCo_{1-y}Fe_yO_3$) or LSCO (e.g. $La_{1-x}Sr_xCo_yO_{3-y}$) [1, 2]. These perovkites are electrically conductive even at room temperature and could be used as substrate for the electrophoretic deposition without any further treatments. However, zirconia can not be deposited directly onto the LSM due to undesired chemical interactions at the interface [3]. Therefore, it is necessary to deposit a thin protective layer of e.g. CGO and deposit a zirconia layer on top of it afterwards. Currently, a research program is performed in ETH Zürich dealing with the DC reactive magnetron sputtering of ceria-yttria and yttria-zirconia layers on porous LSCF supports [4].

Other powder suspensions such as doped lanthanum gallate, doped ceria, or doped bismuthoxide [5] could be used to produce alternative electrolytes via EPD on porous cathode substrates. The feasibility of EPD for the deposition of alternative electrolytes was already demonstrated by El-Sherik [6] who deposited dense $La_{0.8}Sr_{0.2}Ga_{0.85}Mg_{0.15}O_{0.28}$-coatings on porous LSCF-cathode substrates.

2 Electrophoretic Deposition

Although the electrophoretic deposition process was studied in detail in this work it needs further theoretical investigation in order to model its exact deposition mechanism. It is suggested to perform impedance spectroscopic measurements to further study the charge transfer mechanism of the ceramic particles and ions at the electrodes. The discussion in literature is controversial concerning the charge transport in the suspension [7, 8]: It is unclear whether the charge transport is carried out by the charged ceramic particles or by the ions in the suspension or by both. Impedance spectroscopy could give answers to these questions.

3 Alternative Processing Methods

In the course of this dissertation other processing methods for thin electrolytes were also briefly examined (Appendix 2) but not studied in detail. Some of them are very promising but further experimental work is required: The elegant method transfer printing is probably the most interesting candidate. It is simple and easy to perform and the processed layers were very homogeneous and dense. Furthermore, the films can be joined to anodic or cathodic substrates of considerable roughness. Pressure filtration was not considered in this work because the used substrates were not mechanically stable enough to bear the high pressures during filtration. However, thicker and less porous substrates, and careful adjustment of the applied pressure would certainly make pressure filtration a very good processing method for the formation of thin layers.

4 Determination of Layer Thickness using an Oscillating Quartz

In preliminary experiments (appendix 4) it was demonstrated that an oscillating quartz can be principally used to determine the layer thickness during an EPD experiment. However, it turned out that the quartz crystal is very sensitive concerning mounting conditions. The quartz crystal can operate if only one face is dipped into the solution only. Therefore further experiments with optimised quartz holders are necessary. Deposition experiments with the oscillating quartzes in the same suspension as the EPD apparatus need to be performed for calibration.

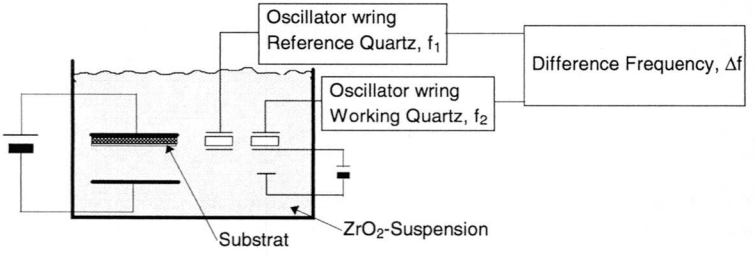

Fig. VI-1: Schematic set-up of the in-situ *determination of layer thickness using an oscillating quartz.*

The set-up of such a measurement is shown in Fig. VI-1. The layer thickness at various field strengths and deposition times can be compared to the measured difference in frequency and a calibration curve can be drawn.

5 References

[1] L. W. Tai, M. M. Nasrallah, H. U. Anderson, D. M. Sparlin, and S. R. Sehlin, "Structure and Electrical Properties of $La_{1-x}Sr_xCo_{1-y}Fe_yO_3$. Part1. The System $La_{0.8}Sr_{0.2}Co_{1-y}Fe_yO_3$" *SSI*, **76**, pp. 259-271, 1995.

[2] L. W. Tai, M. M. Nasrallah, H. U. Anderson, D. M. Sparlin, and S. R. Sehlin, "Structure and Electrical Properties of $La_{1-x}Sr_xCo_{1-y}Fe_yO_3$. Part 2. The System $La_{1-x}Sr_xCo_{0.2}Fe_{0.8}O_3$" *SSI*, **76**, pp. 271-283, 1995.

[3] A. Mitterdorfer, "$La_2Zr_2O_7$ Formation and Oxygen Reduction Kinetic of the $La_{0.85}Sr_{0.15}Mn_yO_3$,$O_3$ (g) YSZ System", *SSI (in print)*, 1998.

[4] C. Kleinlogel, M. Gödickemeier, and L. J. Gauckler, "Cathodes and Cathode Support Structures for Intermediate Temperature Solid Oxide Fuel Cells", The 1997 Joint Internat. Meet., Paris, The Electrochem. Soc., pp. 2494, 1997.

[5] N. Q. Minh and T. Takehiko, "Science and Technology of Ceramic Fuel Cells", Amsterdam, Elsevier, p. 96-101, 1995..

[6] A. M. El-Sherik, P. Sarkar, and A. Petric, "Electrophoretic Deposition of Lanthanum Gallate Solid Electrolyte Coatings on Cathode Substrates", The 1997 Joint Internat. Meet., Paris, The Electrochem Soc. pp. 2564, 1997.

[7] L. J. Vandeperre and O. Van der Biest, "Electric Current and Electric Field for Electrophoretic Deposition from Non-Aqueous Suspensions", *Ceram. Trans.*, **85**, 1997.

[8] P. Sarkar and P. S. Nicholson, "Electrophoretic Deposition (EPD): Mechanism, Kinetics, and Application to Ceramics" *J. Am. Ceram. Soc.*, **79**, pp. 1987-2002, 1996.

Appendix 1

Experimental Details for the Preparation of Ni-CGO Anodes via Tape Casting

1 Introduction

State of the art anodes for solid oxide fuels cells (SOFC) are composed of Ni-cermet. The ceramic part of the cermet is mostly stabilized zirconia and is responsible for the mechanical stability [1], for the prevention of the nickel coarsening at operating temperatures [1-4], and for achieving an anode thermal expansion coefficient which is close to that of the electrolyte [1, 5, 6]. NiO, is the starting material, is reduced to metallic nickel when exposed to the fuel in the SOFC. This metallic Ni is responsible for the electrical conductivity. Several other compositions have also been tested: ruthenium/YSZ [7, 8], mixed-conducting oxides such as ZrO_2-Y_2O_3-TiO_2 [9-11] and CeO_2 based materials [12-17]. In this study, Gd-doped ceria (CGO) was chosen as the ceramic constituent. However tapes processed with a mixture of NiO and ceria were always brittle and cracked during drying. Successful tape processing was only possible with the addition of 9.5 wt.% of cubic stabilized zirconia. This concentration was empirically established.

The aim of this present study was to evaluate the influence of the addition of zirconia on the electrophoretic mobility of the suspension, and on the thermal expansion, sintering shrinkage and electrical conductivity of the tapes. A model for the favorable effect of the zirconia addition on the tape casting process is suggested in the conclusion.

2 Experimental Procedure

The Ni-CGO powder consisting of 70 wt% NiO and 30 wt% $Ce_{0.8}Gd_{0.2}O_3$ (Praxair, USA, medium grain size 0.75 μm) was mixed with the appropriate amount of zirconia powder (ZrO_2-8Y, Tosoh, Japan, medium grain size 0.23 μm). The two powders, the solvent and the dispersant were mixed in a ball mill for 6 hrs. Plasticizer and binder were added and the suspension was homogenized again for half an hour in the ball mill. The exact recipe is listed in Table 1-1.

MATERIAL	wt.%	FUNCTION
60 g Ni-CGO	56.7	Ceramic Powder
10 g ZrO_2	9.5	Ceramic Powder
23 ml Toluene	17.4	Solvent
1.8 g Beycostat	1.8	Dispersant
5.2 g Polyethyleneglycol 600	4.9	Plasticizer
4.5 g Bis(2-ethylhexyl)phtalate	4.3	Plasticizer
5.8 g Polyvinylbutyral (PVB)	5.5	Binder

Table 1-1: Slurry composition of the anode tape.

The suspension was then processed using a tape casting device with a movable doctor blade [1]. Before casting, the glass plate was covered with a polyethylene-foil. The slurry was poured on the plate and spread by the doctor blade with an opening of 250 µm at a speed of 30 cm/min. After drying for 24 hours at ambient temperature round samples were cut out the leather-hard tapes with a metal puncher. The burnout of the organic additives and the underlying foil was carried out using a heating ramp of ½ K/min up to 450 ℃. Sintering was then performed with a heating ramp of 2 K/min up to a temperature of 1350 ℃ and holding at his temperature for one hour. Mobility measurements of the suspensions were carried out using an ESA-system[2]. The suspensions with 1 vol. % solids loading were treated ultrasonic before each measurement. For the expansion and conductivity measurements powder mixtures were dry milled for three hours, isostatically pressed to bars and sintered at 1350 ℃ for one hour. Expansion measurements and the sinter experiments were carried out with a Theta Differential Dilatometer[3]. The electrical conductivity was measured using the 4-pt. method in a reducing atmosphere. All experiments were performed as a function of different NiO-CGO/ZrO_2 ratios.

3 Results

3.1 Optical Characterization and Element Mapping

Fig. 1-1 shows the microstructure of the sintered anode tape made with the composition given in Table 1-1. The porosity was 50 vol. % and the grain size was 0.5 -1 µm. Element mapping with EDX showed a homogeneous distribution of the three

[1] EPH Associates Inc. Orem, Utah, USA

[2] ESA-8000 system, Matec Applied Science, Hopkinton, MA, USA

[3] Dilatronic™ II

components although there were some zirconia agglomerates. The Ni was very homogeneously distributed and formed a percolative network.

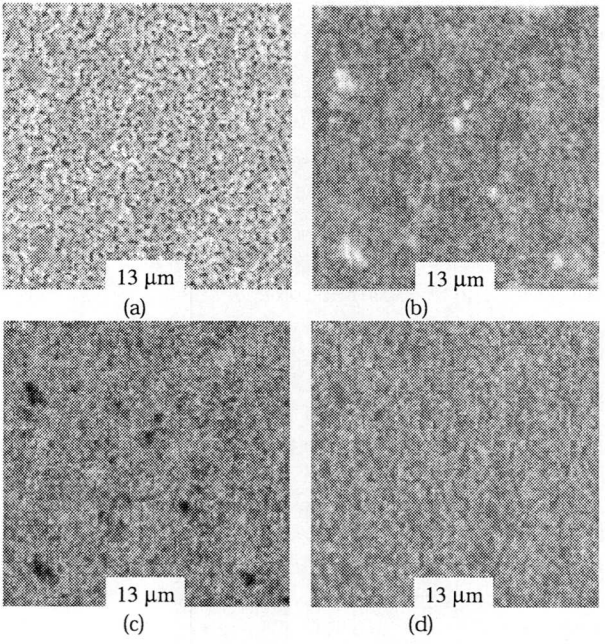

Fig. 1-1
(a) SEM micrograph of the sintered tape cast anode made with the composition given in Table 1-1.
(b) element mapping of zirconium, (c) nickel, and (d) cerium.

3.2 Dynamic Electrophoretic Mobility

Fig. 1-2 illustrates the dynamic electrophoretic mobility of the suspension as a function of different Ni-CGO/ZrO_2 ratios. The mobility of ceramic particles in an organic medium is generally very small [18, 19] compared to those in aqueous media. 1 vol % Ni-CGO powder in toluene exhibited a mobility of $3.7 \cdot 10^{-12}$ m^2/Vs. The addition of 14.3 wt.% zirconia (referred to the amount of Ni-CGO) increased the mobility by a factor of 2. Pure zirconia in toluene had a mobility of $13.2 \cdot 10^{-12}$ m^2/Vs.

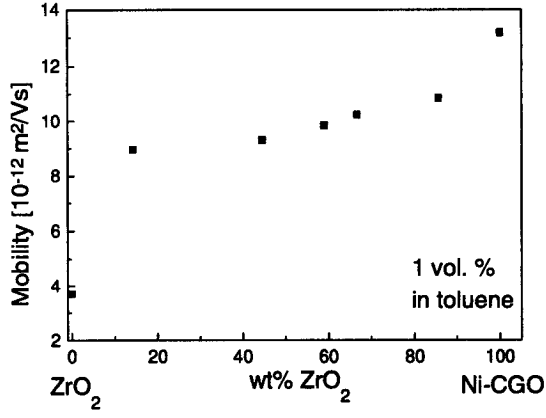

Fig. 1-2: Mobility of 1 vol. % solids suspensions in toluene prepared with different Ni-CGO/ZrO_2 ratios. The addition of ZrO_2 increased the mobility.

3.3 Thermal Expansion Coefficient

Fig. 1-3 shows the variation of the expansion coefficient (RT to 800 ℃) as a function of the ZrO_2-content.

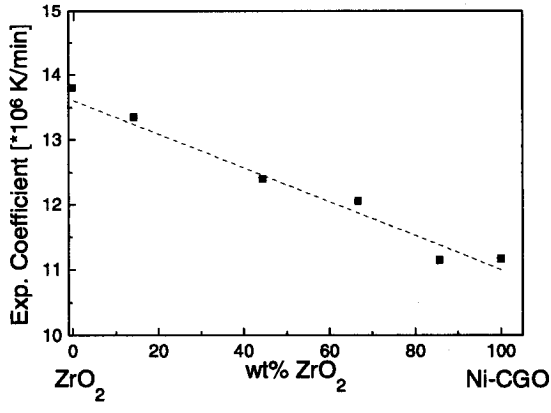

Fig. 1-3: Average expansion coefficient ((RT to 800 ℃) of dry pressed and sintered samples with different Ni-CGO/ ZrO_2 ratio showing a linear relationship between wt.% Ni-CGO and expansion coefficient. The dashed line represents the expansion coefficient calculated with the rule of mixture.

Using the expansion coefficients of the single components of the mixture (NiO: $14 \cdot 10^{-6}$ K^{-1} [20], CGO: $12.7 \cdot 10^{-6}$ K^{-1} [21], ZrO_2: $11 \cdot 10^{-6}$ K^{-1} [22]) the expansion coefficient for the mixture could be estimated as $13.2 \cdot 10^{-6}$ K^{-1} by applying the rule of mixture. This calculated value fits very well the value of $13.38 \cdot 10^{-6}$ K^{-1}. The thermal expansion coefficient of different Ni-CGO/ZrO_2 varies with the zirconia addition, decreasing with decreasing Ni-content (or with increasing zirconia content). This finding is in agreement with the measurements of Majumdar [5] and Ivers-Tiffée [6].

3.4 Sintering Shrinkage

Fig. 1-4 illustrates the sintering shrinkage at 1350 ℃ as a function of different CGO/ZrO_2 ratios. The shrinkage is practically the same for the different ratios.

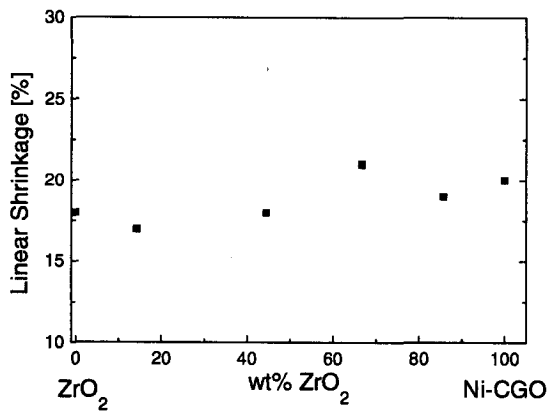

Fig. 1-4: Sinter shrinkage at 1350 ℃ of dry pressed and sintered samples with different CGO/ZrO_2 ratios. The shrinkage kept almost constant.

3.5 Electrical Conductivity

The electrical conductivity as a function of different NiO contents is shown in Table 1-2. The measurements were performed at 700 ℃ under H_2-atmosphere. Marked in bold are the conductivity of the pure Ni-CGO sample and that with the used zirconia addition. The electrical conductivity of Ni-cermet is strongly dependent on its nickel content [23]. The percolation threshold for the conductivity of the cermet is at about 35 vol. % NiO. Below that, the conductivity of the cermet is similar to that of zirconia. Above this value there is a change to metallic conduction through the nickel phase. The conductivity of pure Ni-CGO was $9.4 \cdot 10^{-5}$ S/m whereas the sam-

ple prepared with a powder mixture corresponding to the tape recipe exhibited a conductivity of $7.2 \cdot 10^{-5}$ S/m. Thus, the conductivity of the used tape composition is not remarkably decreased. Thus, the interconnected network of the nickel is not disturbed by the zirconia addition.

wt.% ZrO_2	Electr. Conductivity [S/m]
100.0	$2.0 \cdot 10^{1}$
85.7	$4.6 \cdot 10^{5}$
44.5	$2.0 \cdot 10^{4}$
14.3	$7.2 \cdot 10^{5}$
2.0	$9.4 \cdot 10^{5}$

Table 1-2: Electrical Conductivity of sintered dry pressed samples with different Ni-CGO/zirconia ratios.

4 Summary and Conclusion

Measurements of the mobility suggested that a suspension based on pure Ni-CGO is poorly stabilized. During drying the Ni-CGO will form agglomerates which will cause density differences in the tape and lead to severe crack formation. The crack-preventing addition of zirconia is due to the stabilizing effect of the zirconia powder particles in the suspensions. The almost uncharged Ni-CGO-particles are most probably situated between the highly charged zirconia particles and are supported by them as shown in Fig. 1-5.

Thus, the tape can now be successively processed without cracking. The addition of zirconia did not significantly change the properties of the active anode. Moreover, the lowering of the expansion coefficient is certainly an advantage. The Ni-cermet anode generally has a higher thermal expansion coefficient than YSZ and other cell components. Thus lowering the degree of mismatch between the anode and the other cell components decreases stresses. The electrical conductivity of samples prepared according to the tape cast recipe with addition of zirconia does not change significantly compared to that of pure Ni-CGO powder. The conductivity is still high enough for application in a SOFC.

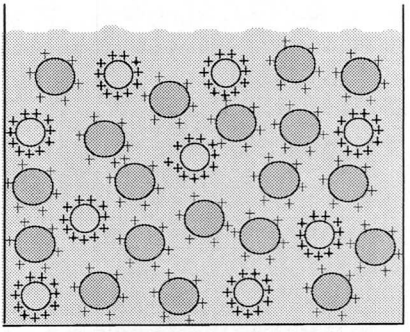

Fig. 1-5: Model for the favorable effect of the zirconia particles onto the tape cast processing of the Ni-CGO. Grey spheres: Ni-CGO particles, white spheres: charged zirconia particles.

5 References

[1] N. Q. Minh and T. Takehiko, "Science and Technology of Ceramic Fuel Cells", Amsterdam: Elsevier, pp.147-118, 1995.

[2] T. Kawada, N. Sakai, H. Yokokawa, M. Dokiya, M. Mori, and T. Iwata, "Characteristics of Slurry-Coated Nickel Zirconia Cermet Anodes for Solid Oxide Fuel Cells" *J. Electrochem.*, **137**, pp. 3042-3947, 1990.

[3] P. Ekanayake, M. Gödickemeier, and L. J. Gaukler, "Electrochemical Characterization and Microstructure of Ni-YSZ Anodes in Solid Oxide Fuel Cells (SOFC)" *SSI*, **42**, pp. 535-543, 1997.

[4] S. Murakami, Y. Akiyama, N. Ishida, Y. Miyake, M. Nishioka, Y. Itoh, T. Saito, and N. Furukawa, "Study on Solid Oxide Fuel Cells, I. Influence of ZrO_2 Content in an Anode on its Electrode Characteristics" *Denki-Kagaku*, **59**, pp. 320-324, 1991.

[5] S. Majumdar, T. Claar, and B. Flandermeyer, "Stress and Fracture Behavior of Monolithic Fuel Cell Tapes" *J. Am. Ceram. Soc.*, **69**, pp. 628-633., 1986.

[6] E. Ivers-Tiffée, M. Schiessl, and W. Wersing, "Ceramic and Metallic Components for a Planar SOFC" *Berichte Bunsenges.*, **94**, pp. 978-81, 1990.

[7] M. Suzuki and A. Kajimura, "Geometrical Analysis of SOFC Anodes Fabricated by Electrochemical Vapor Deposition" *Denki Kagaku*, **65**, pp. 859-864, 1997.

[8] H. Sasaki, M. Suzuki, S. Otoshi, A. Kajimura, and M. Ippommatsu, "High Power Density Solid Oxide Electrolyte Fuel Cells" *J. Electrochem. Soc.*, **139**, pp. L12-13, 1992.

[9] S. S. Liou and W. L. Worrell, "Electrical Properties of Novel Mixed-Conducting Oxides" *Appl. Phys. A*, **A49**, pp. 25-31, 1989.

[10] R. M. C. Marques, J. R. Frade, and F. M. B. Marques, "Ceramic Materials for SOFC Anode Cermets", Third International Symposium on Solid Oxide Fuel Cells, Honolulu, Hawai, S.C. Singhal, H. Iwahara, The Electrochem. Soc. 1993, pp. 513-22.

[11] M. T. Colomer, L. S. M. Traqueia, J. R. Jurado, and F. M. B. Marques, "Role of Grain Boundaries on the Electrical Properties of Titania Doped Yttria Stabilized Zirconia" *Materials-Research-Bulletin*, **30**, pp. 512-522, 1995.

[12] T. Takahashi, H. Iwahara, and Y. Suzuki, "Electrode Materials for High Temperature Solid Electrolyte Fuel Cells, in [10] pp. 113-119.

[13] M. Mogensen, T. Lindegaard, and T. U. Hanse, "Physical Properties of Mixed Conductor Solide Oxide Fuel Cell Anodes of Doped CeO_2" *J. Electrochem. Soc.*, **141**, pp. 2122-2128, 1994.

[14] I. Metcalfe, P. H. Middleton, P. Petrolekas, and B. C. H. Steele, "Hydrocarbon Activation in Solid State Electrochemical Cells" *SSI Ionics, Diffusion & Reactions.*, **57**, pp. 259-264, 1992.

[15] H. Uchida, N. Machizuki, and M. Watanabe, "High-Performance Electrode for Medium-Temperature Operating Solid Oxide Fuel Cells. Polarization Property of Ceria-Based Anode with Highly Dispersed Ruthenium Catalysts in (H_2+CO_2/+H_2O) Gas" *J. Electrochem. Soc.*, **143**, pp. 1700-1704, 1996.

[16] H. Nagamoto, K. Kumagai, and H. Murayama, "Characteristics of Ni/Nd-Doped Ceria Anode for Solid Oxide Fuel Cell", 1995 MRS Fall Meeting., Boston, USA, 1995, pp. 255-259.

[17] M. Watanabe, H. Uchida, M. Shibata, N. Mochizuki, and K. Amikura, "High Performance Catalyzed-Reaction Layer for Medium Temperature Operating Solid Oxide Fuel Cells" *J. Electrochem. Soc.*, **141**, pp. 342-346, 1994.

[18] M. E. Labib and R. Williams, "The Use of Zeta-Potential Measurements in Organic Solvents to Determine the Donor-Acceptor Properties of Solid Surfaces" *J. Coll. Interf.*, **97**, pp. 356-378, 1993.

[19]H. Koelmans, "Suspensions in Non-Aqueous Media" *Philips Research Reports*, **10**, pp. 161-193, 1955.

[20] R. C. Weast and D. R. Lide, *Handbook of Chemistry and Physics.* Florida, USA: CRC Publishers, 1990.

[21] M. Gödickemeier, "Mixed Ionic Electronic Conductors for Solid Oxide Fuel Cells", Diss. ETH No. 11348, p. 85, 1986

[22] in [1] p. 80

[23] in [1] pp. 156-158

Appendix 2

1 Different Deposition Techniques

The support structure for the electrolyte deposition is composed of the ceramic foam and the active anode as described in chapter IV-5. However, not for all the deposition experiment, a complete support structure was necessary. For the optimization of the deposition processes, a cast Ni-cermet precursor tape with a thickness of 450 μm was chosen as substrate for all experiments to ensure sufficient mechanical stability. This thick tape was pre-sintered at 1100 ℃ for all the deposition experiments (with the exception of the laminating process).

1.1 Tape Laminating

The recipe of the zirconia tape laminated with a green Ni-cermet precursor tape is given in Table 2-1.

MATERIAL		wt.%	FUNCTION
100 g	ZrO_2 (TZP) (3YS Tosoh)	62.2	Ceramic Powder
42 g	Ethanol/ Toluol (68:32wt%)	26.1	Dispersion Medium
2.65 g	Triolein[1]	1.6	Dispersant
5 g	Polyethylengylcol 600[3]	3.1	Plasticizer
3 g	Bis(2-ethylhexyl)phtalate[3]	1.9	Plasticizer
8 g	PVB[2]	4.9	Binder

Table 2-1: Slurry composition for the zirconia tape

The zirconia tape was prepared according to the procedure already described for the Ni-cermet precursor tape (chapter IV-5.2), the milling time was 48 hrs. The tape was cast using a doctor blade with an opening of 200 μm. After drying the tape had a thickness of 80 μm. Two round samples (30 mm in diameter) were cut out of the tapes, placed on top of each other and laminated at a pressure of 3 bar at a temperature of 30 ℃ in a lamination box. This laminated bilayer was covered with a porous zirconia plate and sintered according to the following schedule derived by the DTA measurements of both tapes (Fig. 2-1):

---

[1] Fluka Chemie, CH-Buchs

[2] Mowital B20 H, Hoechst, Germany

25 K/h to 300 ℃ (holding time 1h)
25 K/h to 400 ℃ (holding time 3h)
60 K/h to 1400 ℃ (holding time 1h)
120 K/h to 30 ℃

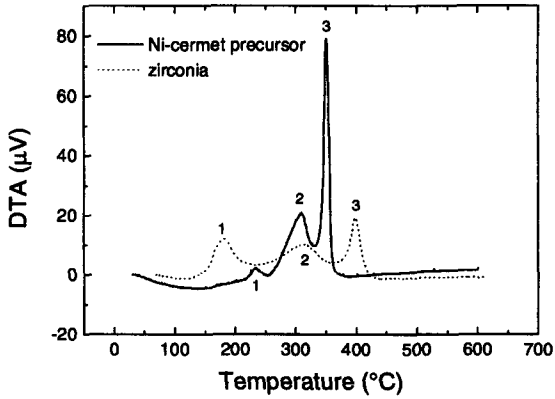

Fig. 2-1: Thermal-analysis of the zirconia and Ni-cermet precursor tape. Peaks can be correlated to the decomposition of solvent(1), dispersant (2), binder and plasticizer (3).

The green density of the zirconia tape was 35% of the theoretical value (TD = 6.01 g/cm^3). After sintering, the two tapes were intimately connected without a separating gap as presented in Fig. 2-2. The samples showed no macroscopic cracks after sintering. However, the bilayer was not totally flat but showed some warpage. This was probably due to the low green density of the zirconia tape which therefore exhibits a higher sintering shrinkage than the Ni-cermet precursor tape. Nevertheless, the zirconia layer was almost dense and had a thickness of 50 µm. The closed porosity is characterized by isolated round holes with diameters of 3-5 µm. These holes can also be seen at the surface of the zirconia layer and are probably formed due to the high organic content in the green tape. It is interesting to note that the sintering shrinkage is not the same in each direction. The samples exhibit a larger shrinkage perpendicular due the surface than in the than lateral direction. This can be seen by comparing the appearance of the holes: They change from totally round in the surface picture (b) to more longish shaped holes in the fracture surface (a).

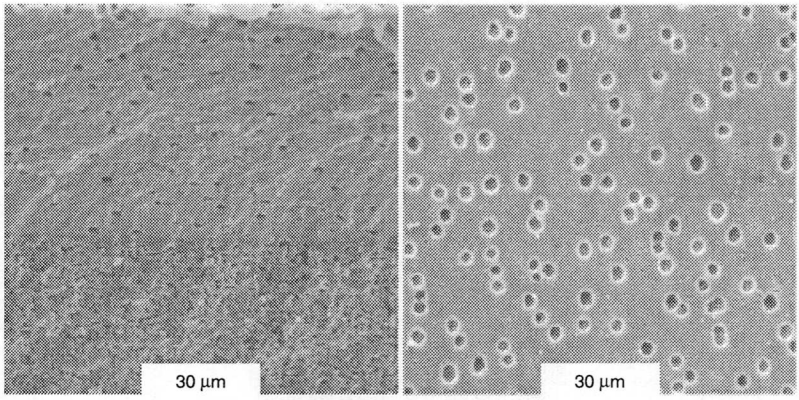

Fig. 2-2: SEM-micrograph of the laminated tape sample after sintering. (b) fracture surface: zirconia on top, Ni-cermet precursor below, (b) surface of the zirconia layer.

1.2 Sedimentation

The anodic pre-sintered tape to be coated was placed onto a porous porcelain in a filter funnel. A hallow cylinder consisting of polydimethylsiloxane[3] (PDMS) was prepared and placed onto the anodic tape. The very low surface tension and the elasticity of the PDMS leads to a sealing of the polymer cylinder with the anodic tape. The aqueous zirconia suspension (2 vol. % solids loading) used in this deposition process was stabilized electrostatically by adjusting the pH at 5 (according to the mobility values of Fig. 2-3) with hydrochloric acid. After milling for 24 h with zirconia milling balls in a polyethylene bottle the suspension was passed through a 6 µm sieve[4] to remove agglomerates and other impurities. The ceramic suspension was then poured into the PDMS cylinder which was subsequently closed with a plastic foil. The set-up is shown in Fig. 2-4. After a week the supernatant liquid was decanted and the sediment was dried for two days. The PDMS cylinder was removed from the anode substrate and the bilayer was sintered with a heating rate of 1 K/min to 1400 ℃ with a holding time of one hour). For the measurement of the green density the resulting green layer was removed from the substrate.

---

[3] Sylgard 184, Dow Corning, USA

[4] Seidengaze AG, CH-Zürich

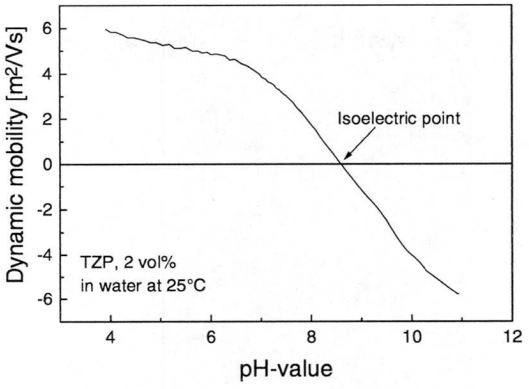

Fig. 2-3: Mobility measurement of a water based zirconia suspension.

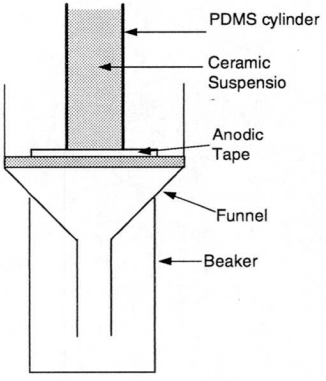

Fig. 2-4: Schematic of the sedimentation process.

The green density of the zirconia layer made via sedimentation was 59% TD. Fig. 2-5 illustrates the microstructure of the sintered zirconia layer. The layer did not show any voids and had a very fine microstructure. However, it was not possible to co-sinter the zirconia with the Ni-cermet precursor. They did not sinter together and separated during sintering.

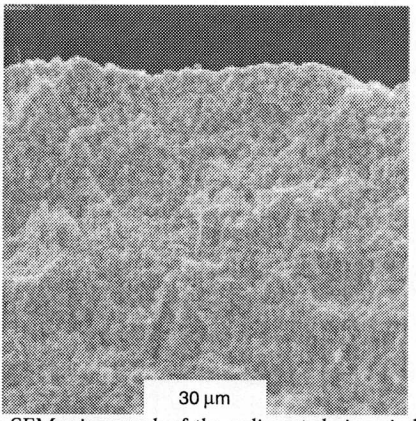

Fig. 2-5: SEM-micrograph of the sedimented zirconia layer after sintering.

1.3 Slurry Coating

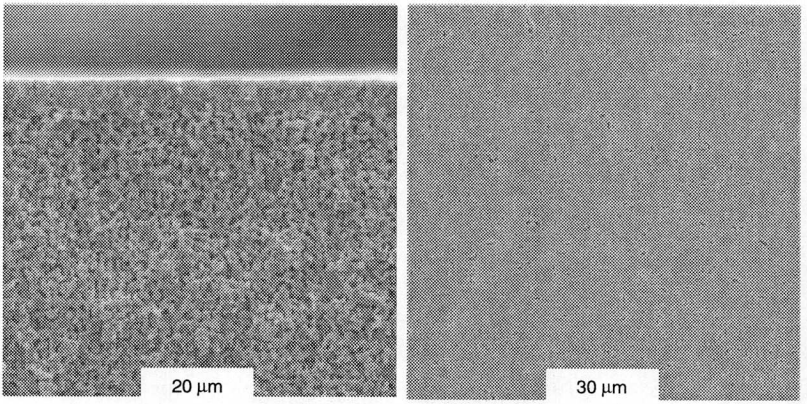

Fig. 2-6: SEM-micrograph of the zirconia layer processed via slurry coating after sintering.

(a) fracture surface: zirconia on top, Ni-cermet precursor below,
(b) surface of the zirconia layer.

The zirconia suspension used was prepared in the same way as the suspension of the sedimentation process. 1 ml suspension was then cast onto the substrate and

dried at room temperature for 4 hours. This process was repeated 5 times. For the measurement of the green density the resulting green layer was removed from the substrate. Sintering of the bilayer was performed with a heating rate of 1 K/min to 1400 ℃, and a holding time of one hour.
The green density of the slurry-coated zirconia layer was 40% TD. The coated samples were flat and did not show severe cracking after sintering. As seen in Fig. 2-6 the zirconia layer adhered very well to the anodic substrate. Some of the zirconia was deposited inside the porous substrate which results in a very good mechanical interlocking. The flat layer had a uniform thickness of 8 μm. The surface of the slurry-coated layers showed severe microcracking after sintering due to strong shrinkage during drying.

1.4 Transfer Printing

A highly viscous zirconia suspension was prepared by mixing the powder with an organic screen-print paste[5] and milling for 24 hrs. The suspension was then screen-printed using a screen-print mask with an area of 1 by 1 cm on a paper coated with a water soluble gum[6]. The thickness of the printed layer was 100 μm.

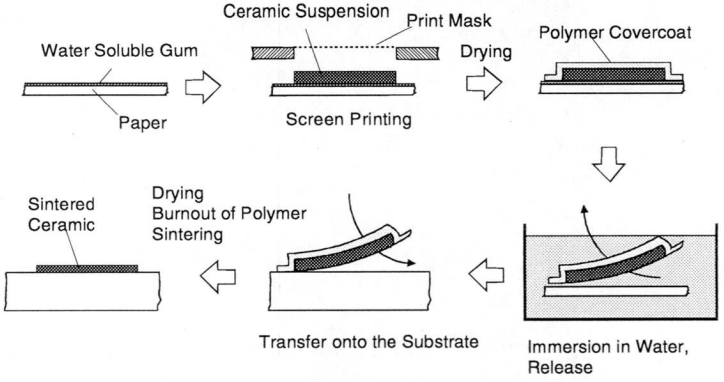

Fig. 2-7: Schematical description of the transfer-printing process.

After drying, an acrylic resin covercoat[7] was screen-printed (or painted) over the zirconia layer. The zirconia layer with the covercoat was dried for one day, released from the paper by immersion in water, and then draped over the pre-sintered ano-

[5] screen print paste: 6B/292, Cookson Matthey, Burslem, Staffs, U.K.
[6] gum paper: KVD, Keramik Dekor Verlag, Postfach 1343, D-90507 Zirndorf
[7] covercoat:OPL 465, Cookson Matthey, Burslem, Staffs, U.K.

dic tape. Again, the sample was dried for one day and then sintered with a heating rate of 1 K/min to 1400 ℃, and a holding time of one hour.
The green samples exhibited a density of 50% TD. The coated samples remained flat after sintering and showed no cracks. The micrograph of the transfer printed layer (Fig. 2-8) shows very good adhesion of the zirconia film to the substrate. The thickness of the layer was about 15 µm and remained constant across the whole substrate.

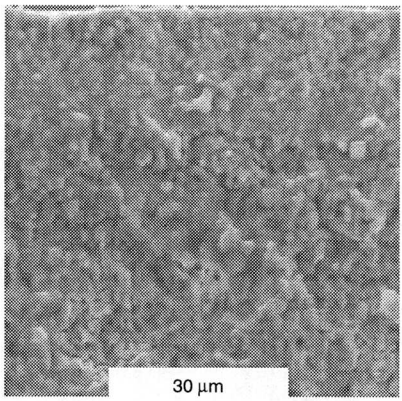

Fig. 2-8: SEM-micrograph of the zirconia layer processed via transfer printing after sintering. Fracture surface: zirconia on top, Ni-cermet precursor below.

2 Summary

From all the feasible processing methods for the deposition of thin layers on the porous substrate, the elegant method of transfer printing seems to be the most promising method. It is simple, quick and the surface roughness is of no importance. A second alternative is pressure filtration using the same set-up as described for the sedimentation process, if one succeed in improving the mechanical strength of the used substrate.

Appendix 3

Quarz Crystal: A New *in-situ* Method for the Determination of the Layer Thickness During an EPD-Process

This new method uses a an oscillating quartz crystal plate, usually AT-cut, upon which an additional mass is loaded resulting in a lowering Δf of the oscillation frequency. The equation governing the frequency change Δf has been given by Sauerbrey [1] and may be written in simple form as

$$\Delta f = k \Delta m \qquad \text{Eq. 3-1}$$

where k is a constant and Δm is the incremental mass load.
Quartz crystals are widely used as mass sensitive device in gas analysis with a considerable variety of coating materials [2, 3]. Only few references describe the application of quartz crystals for monitoring under-liquid mass deposition [4-6]. However, the observed frequency shift in liquids is not only caused by a mass effect, but properties such as density and viscosity of the liquid and viscoelastic properties of the coating [6] may also change it.

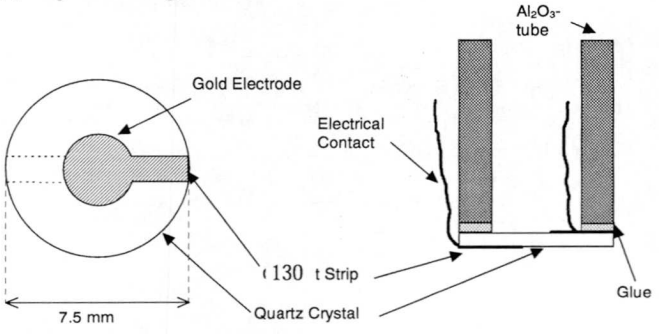

Fig. 3-1: The quartz crystal with the sputtered gold electrodes on the left side. On the right side the cross section of the used set-up.

Round AT-cut quartz crystals with a resonance frequency of 5 MHz (Quartz Crystal Technology) were used in both the working and reference oscillator circuits. On both sides of the quartz crystals gold electrodes were applied, as shown in Fig. 3-1 to ensure good electrical contacts. The quartz crystal was glued with a sealant (Sylgard 184, Dow Corning, USA) onto a Al_2O_3-tube having a diameter of 26 mm. The wiring diagram is shown in Fig. 3-2. The circuit consists of two identical oscillator coils and a simple differential wiring which shows the frequency difference

between the working and the reference crystal. The oscilloscope was Le Croy 9450A. This circuit was utilized according the modified set-up of Bruckenstein [7] and Hwang [8].

Two measurements were performed: measurements of the frequency difference as a function of the medium used and electrophoretic measurements which were carried out using the working quartz crystal as the negative electrode and a copper electrode as positive electrode. The quartz crystals were fixed with one face in contact with the ceramic suspension containing the dispersed zirconia particles. The distance between the two electrodes was 5 cm, the applied electrical voltage 5 V.

Table 3-1 lists the results of the experiments of the two crystals in different media. There was a frequency difference when using the same medium for both crystals which was due to a incomplete performed tuning of the resonance frequency of both crystals. However, there was a measurable difference of the frequency when using different media. The method is therefore generally suited for the intended measurements.

Reference Crystal in	Working Crystal in	Frequency Difference
Air	Air	2.245 kHz
Air	Ethanol	5.202 kHz
Ethanol	Ethanol	2.526 kHz
Ethanol	Suspension	4.902 kHz

Table 3-1: Frequency Difference as a function of the medium.

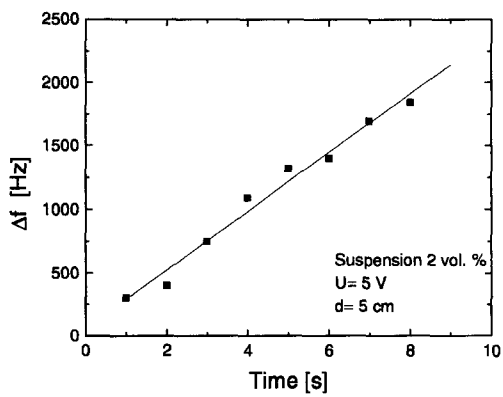

Fig. 3-3: Frequency difference vs. deposition time.

In Fig. 3-3 the frequency difference is plotted against the deposition time. Clearly, there is an linear increase in the frequency difference, which is due to the additional mass load is which was deposited on the working electrode.
The measurement of the layer thickness using the quartz crystal would have the advantage that it is independent of changes in the suspensions such as viscosity, temperature and solids loading. In preliminary experiments it was demonstrated that this method can be principally used to determine the layer thickness during an EPD experiment. However, it turned out that the quartz crystal is very sensible concerning mounting conditions.

References

[1] G. Z. Sauerbrey, "Verwendung von Schwingquarzen zur Wagung dünner Schichten und zur MIkrowaaung " *Z. Phys.*, **155**, pp. 206, 1959.

[2] L. Göpel, J. Hesse, and J. N. Zemel, *Sensors: Chemical and Biochemical Sensors*: VCH Weinheim, pp. 23-46, 1991.

[3] J. J. MaGallum, "Piezoelectric Devices for Mass and Chemical Measurements", *Analyst*,. **114**, pp. 1173, 1989.

[4] H. Muramatsu, J. M. Dicks, E. Tamiya, and J. Karube, "Piezoelectric Crystal Biosensor Modified with Protein A for the Determination of Immonoglbulins", *Anal. Chem.*, **59**, pp. 2760-2763, 1987.

[5] J. Hartmann, J. Auge, R. Lucklum, S. Rösler, P. Hauptmann, B. Adler, and E. Dalcanale "Supramolecular Interactions on Mass Sensitive Sensors", *Sens. Actuators*,. **B34**, pp. 305-311, 1996.

[6] J. S. Graham and D. R. Rosseinsky, "Apparantly Viscoeleastic Responses in a Quarts Crystal Microbalance Study of an Electrodepsited Non-Aqueous Colloid Film", *J. Chem. Soc. Faraday Trans.*, **90**, pp. 3657-3661, 1994.

[7] S. Bruckenstein and M. Shay, "Experimental Aspects of Use of the Quartz Crystal Microbalance in Solution", *Electrochem. Acta*, **30**, pp. 1295-1300, 1985.

[8] E. Hwang and Y. Lim, "Construction of Low Noise Electrochemical Quartz Crystal Microbalance", *Bull. Korean. Chem. Soc.*, **17**, pp. 39-42, 1996.

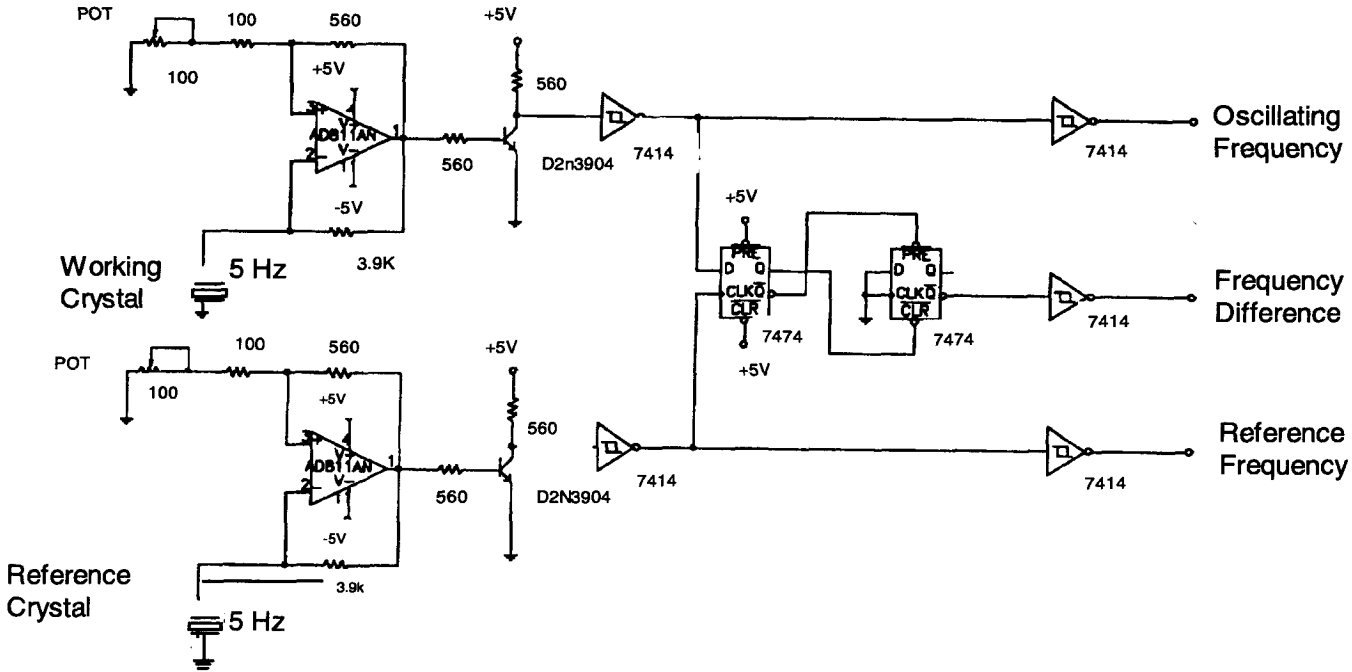

Fig. 3-1: Wiring diagram of the used set-up.

Appendix 4

1 Electric Field Distribution in the EPD-Cell

The EPD apparatus can be compared to a simple plate capacitor. The applied electrical voltage will build up the electrical field between two plates which must be homogeneous to guarantee an even distribution of the ceramic particles. Fig. 4-1 shows a field inhomogeneity at the edges of a plate condenser. To avoid this, the size of the condenser plates has to be adjusted to that of the substrate. The apparatus should allow to use substrates with diameters from 40 to 70 mm.

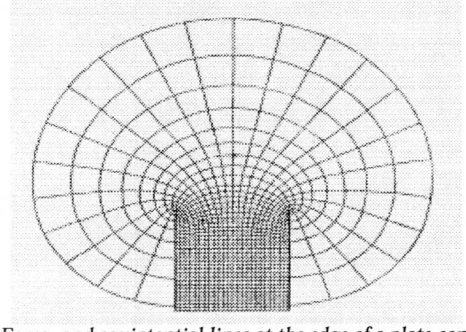

Fig. 4-1: Force- and equiptential lines at the edge of a plate condenser [1].

1.1 Field Calculations

The homogeneity of the electrical field is one of the main conditions for a successful deposition process. Knowing the exact course of the field lines allows the calculations of the dimensions of the apparatus. Generally, electrical fields can be defined using experimental, mathematical or graphical methods [2-5]. The experimental methods can be divided into three groups: (1) Methods where samples are in the electrical field, (2) Methods, which represent the field (analogy-methods), (3) Methods, in which field probes are used. The most common method is the measurement with a field probe. However, its size will distort the electrical field. Electro-optical field probes do not have this disadvantage, but are expensive and are not commercially available [6].

1.1.1 Analogy-Method

By using the analogy method, the system is simplified to a two-dimensional problem. The two-dimensional conductor was a 100x320 mm sized graphite paper, on

which the two conductive silver electrodes were painted with a length of 200 mm and at a distance of 50 mm (Fig. 4-2). A potential of 50 V was applied and the potential between the silver electrodes was measured by means of a metal probe. The measurements were performed at distances of 1, 5, 10, 15 and 20 mm parallel to the positive electrode. This measuring range cuts several equipotential lines whose potential was measured with a voltmeter. For each distance the measurements were performed three times, the error was ± 0.8 V.

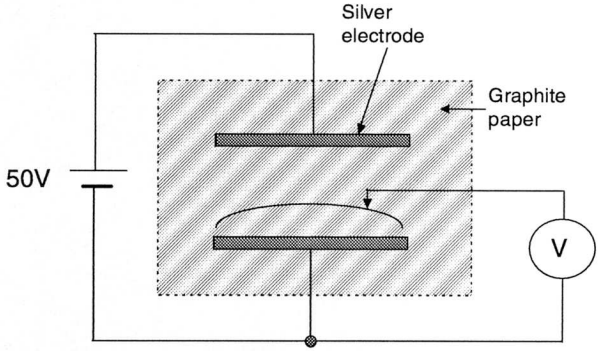

Fig. 4-2: Analogy method: The graphite paper is the two-dimensional conductor; the potential between the two silver electrodes can be measured.

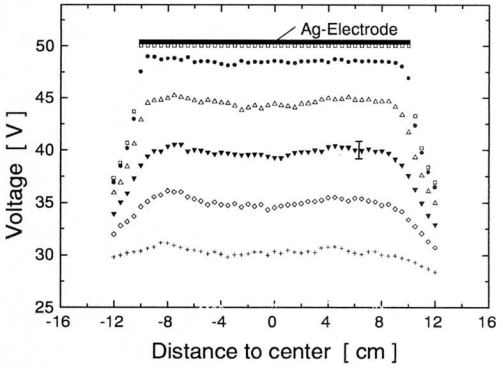

Fig. 4-3: Potential between two silver electrodes measured in different distances (0, 1, 5, 10, 15, and 20 mm).

As illustrated in Fig. 4-3, the potential decreases at the edges of the electrodes which corresponds to a decrease of the electrical field at that location. The potential is mostly lowered at the outer third of the electrode. For the homogeneous deposi-

tion on a substrate, the size of the substrate must be at least one third smaller than the used electrode. Therefore, the dimensions of the electrodes must be at least 10 cm for the desired substrate length of 7 cm large substrates (at an electrode distance of 5 cm). For safety reasons a plate size of 12 cm was chosen.

1.1.2 Conformal Representation

The homogeneous field was transformed to a field of a semicircle against a straight line with the help of the formulation of Maxwell [5, 8].
The representation functions of the borders of the plate condenser are:

$$z = \frac{a}{\pi}(w + 1 + e^{w}) \qquad \textit{Eq. 4-1}$$

A separation into a real- and an imaginary part gives:

$$x = \frac{a}{\pi}\left[u + 1 + e^{u} \cdot \cos(v)\right] \qquad \textit{Eq. 4-2}$$

$$y = \frac{a}{\pi}\left[v + e^{u} \cdot \sin(v)\right] \qquad \textit{Eq. 4-3}$$

This results in two relationships, $x = f_x(u,v)$ and $y = f_y(u,v)$ with the parameters u and v assuming of a v/u-system, the boundaries of the field are formed by $v_I = 0$ and $v_{II} = \pi$. The w-plane is represented as a field of the z-plane in which the zero-potential line is a straight line, and the π-potential is a semicircle. These lines are represented in such a way that the π-line bents down 180° (Fig. 4-4.).

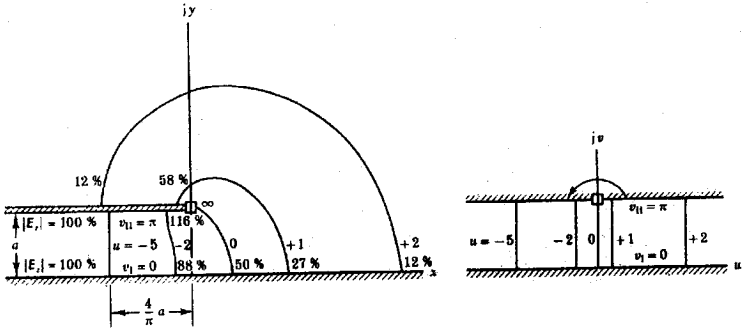

Fig. 4-4: transformation of a homogeneous field of a semicircle into a straight line with the help of the Maxwell equation [8].

With these two v-borders the original Eq. 4-1 simplifies to

$$\left.\begin{aligned} x &= \frac{a}{\pi}\left(u + 1 + e^{u}\right) \\ y &= 0 \end{aligned}\right\} \quad \text{for } v_I = 0 \qquad \textit{Eq. 4-4}$$

and

$$\left.\begin{aligned} x &= \frac{a}{\pi}\left(u+1-e^{u}\right) \\ y &= a \end{aligned}\right\} \quad \text{for } v_{II} = \pi \qquad \textit{Eq. 4-5}$$

Hence, a is the distance between the two lines. Concerning the field lines of the represented electrode system, line u=0 is at the square symbol. For u = negative, the field lines run more and more between the straight lines. Starting at the already straight field line u=-5 (with $x = -4/\pi \cdot a$) they are all within the homogeneous region. However, for positive u the field lines are located predominantly in the border zone of the conformation.

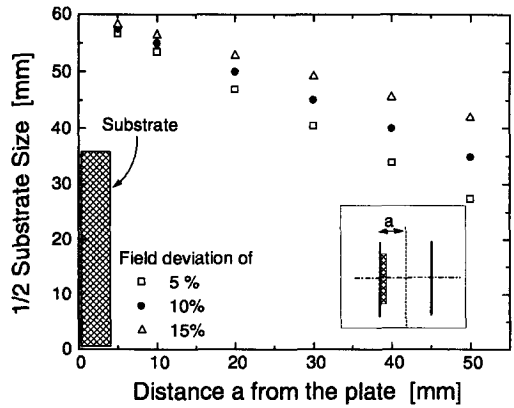

Fig. 4-5: Calculated field deviations at the edge of a plate condenser. The plate size was kept constant at 12 cm. Field deviations of 5, 10 and 15% were calculated for different plate distances. The homogenous field in the middle was taken as 100%.

For the calculation of the ratio between the field strength at the border and of the homogeneous field strength the following formula can be used [5]:

$$V_E = \frac{1}{\sqrt{1+e^{2u}+2e^{u}\cdot\cos(v)}} \qquad \textit{Eq. 4-6}$$

This relationships can be limited to one half of the electrode due to symmetry reasons whereby the abscissa x is the symmetry axis between the two electrodes. This relationship is useful to calculate the electrical field in relationship to the distance a. Therefore, the equation 4-5 was used, where $v_{II} = \pi$. Its values were compared with those resulting from equation 4-6. The size of the electrodes was 12 cm.

Deviations from the homogeneous field (100%) are plotted in Fig. 4-5. Due to symmetry, only the upper left quarter of the whole arrangement is drawn. The insert of Fig. 4-5 shows the whole arrangement. The deviation from the external applied electrical field depends on the plate distance a. For the 7 cm large substrate the half plate distance should be not more than 4 cm. At this and smaller distances the field deviation is less than 5 %.

2 Summary

The aim of this study was to determine the dimensions of the EPD apparatus for a homogenous deposition onto porous substrates. The EPD-apparatus should allow to use substrates with diameters from 40 to 70 mm. The field strength should be variable in order to investigate the deposition parameters. This is possible by changing the distance between the two electrode plates or the applied voltage. The electrical field between the plates must be homogeneous to guarantee a homogeneous deposition of the ceramic particles. The size of the electrode plates has to be adjusted to the size of the substrate thus avoiding inhomogeneities. Two methods of field strengths calculations were performed to determine the proper plate size. According to these calculations a plate size of 14x14 cm was chosen with a maximum plate distance of 8 cm.

3 References

[1] W. Rogowski, "Die elektrische Festigkeit am Rande des Plattenkondensators," *Archiv für Elektrotechnik*, **12**, pp. 1-15, 1923.

[2] R. Strigel, *Ausmessung von elektrischen Feldern*, Karlsruhe, G.Braun, pp. 1-9, 1949.

[3] M. Marinescu, *Elektrische und magnetische Felder*. Berlin: Springer Verlag, pp. 107-122, 1996.

[4] J. Glimm, "*Feldsonden, Stand der Technik und aktuelle Probleme bei Feldmessungen*", Braunschweig: Physik. Techn. Bundesanstalt, pp. 7-84, 1992.

[5] M. Beyer, W. Boeck, K. Möller, and W. Zaehng, *Hochspannungstechnik*. Springer Verlag, pp. 25-61, 1986.

[6] P. Bauerschmid, "*Optischer Spannungs- und E-Feldsensor auf Basis eines X-Cut-Quarz-Resonators mit streckenneutraler optischer Signalübertragung*", Düsseldorf: VDI Verlag, pp. 18-25, 1995.

[7] Physik, "Praktikumsanleitung, Physik, Versuch Nr. 3" ETH Zürich, Zürich 1997.

[8] H. Prinz, "*Hochspannungsfelder*", München: Oldenbourg, pp.113-116, 1969.

Abbreviations

CGO: $Ce_{0.8}Gd_{0.2}O_3$
EPD: Electrophoretic Deposition
ESA: Electrokinetic Sonic Amplitude
HEXIS: Heat Exchanger Integrated Stack
LSM: $La_{0.84}Sr_{0.16}C_{0.02}O_3Mn_{3-x}$
LSCF: $La_{1-x}Sr_xCo_{1-y}Fe_yO_3$, Alternative cathode material
LSCO: $La_{1-x}Sr_xCo_yO_{3-y}$, Alternative cathode material
Ni-CGO: Mixture of 70 wt.% NiO and 30 wt.% CGO
PEN: Positive Electrode, Electrolyte, Negative Electrode
PPI: Pores per Linear Inch
SEM: Scanning Electron Microscope
SOFC: Solid Oxide Fuel Cell
TZP: Tetragonal Stabilized Zirconia Polycrystals

Curriculum Vitae

Personal

Date and place of birth:	July, 2, 1962, in Saarbrücken, Germany
Marital status:	Married
Nationality:	German

Education

1969-1983	Grundschule and Gymnasium in Saarbrücken
1988-1994	Student of Materials Science, University Erlangen-Nürnberg, Germany
1994	Diploma in Materials Science
1994 - present	Research associate and Ph.D. student, chair of Nonmetallic Materials, Dept. of Materials Science, ETH Zürich, Switzerland

Work Experience

1983-1986	Apprenticeship as veterinary associate
1986-1987	Manager of animal pound, Erlangen, Germany
1987-1988	Physican assistant, Dr. med. Streng, Erlangen
1989-1993	Physican assistant, Dr. med. Kuschma

Study Abroad

08/92-05/93	Scholarship of the DAAD (DeutscherAkademischer Auslandsdienst) Student at College for Ceramics, Alfred University, Alfred, New York, USA

Publications

1. S. Al-Wakeel, J. Will, N. Ari, "Entwicklung und Inbetriebnahme einer Elektrophorese-Einheit zur Abscheidung dünner Zirkonoxid-Schichten", *Bull. Hochschule Zürich*, **37**, 47, pp.10-11, 1998

2. L.J. Gauckler, W. Si, T.J. Graule, F.H. Baader, and J. Will, "Enzyme Catalysis of Ceramic Forming: Alumina and Silicon Carbide", Key Engin. Mat. **159-160**, pp 135-150, 1999

Presentations

1. J. Will, F.H. Baader, D. Tieche, T.J. Graule, and L.J.Gauckler, "Direct Coagulation Casting (DCC): Processing of Al_2O_3", Poster, Internat. Conference on Ceramic Processing Science and Technology, Sept. 11-14, Friedrichshafen, Germany, 1994.

2. F.H. Baader, J. Will, D. Tieche, T.J. Graule, and L.J. Gauckler, "High Strength Alumina Produced by Direct Coagulation Casting", Proc. Internat. Conf. Ceram. Process. Science and Techn., Sept. 11-14, Friedrichshafen, Germany, pp 463-467, 1994.

3. J. Will, F.H. Baader, D. Tieche, T.J. Graule, and L.J. Gauckler, "Direct Coagulation Casting (DCC): Herstellung von Al_2O_3-Keramik", Poster, SVMT Conference, May^{13th}, Thun, Switzerland, 1995.

4. J. Will and L.J. Gauckler, "Ceramic $LaSrMnO_3$ Foams for SOFC", Swiss SOFC Day, November^{10th}, Ovronnaz, Switzerland, 1995.

5. J. Will, D. Tieche, T.J. Graule, F.H. Baader, and L.J. Gauckler, "Forming of Complex Ceramic Bodies By Direct Coagulation Casting (DCC)", Poster, 2nd Internat. Meeting of the Pacific Rim Ceramic Societies, *PacRim2*, July 15-17, Cairns, Australia, 1996.

6. J. Will, Z. Xie, T.J. Graule, F.H. Baader, and Gauckler, "Direct Coagulation Casting (DCC): Prozessverfahren", Proc. Werkstoffwoche 96, Symp. 6, Stuttgart, Germany, pp. 519-524, G. Ziegler, H. Chedron, W. Herml, J. Hirsch, H. Kalaska (Eds), DGM, Stuttgart, Germany, 1997.

7. L.J. Gauckler, T.J. Graule, F.H. Baader, and J. Will, "Enzyme Catalysis of Alumina Forming", Proc. Int. Symp. on Novel Synthesis and Processing of Ceramics, Oktober, 26-29, Kurume, Kyushu/Fukuoka, Japan, 1997

8. L.J. Gauckler, T.J. Graule, F.H. Baader, and J. Will, "Colloidal Processing of Ceramics: Direct Coagulation Casting", Proc. 3rd Int. Ceramic Congress, Turkish Ceramic Society, Oktober, 22-25. Istabul, Turkey, III Ceramic Congress, 2, pp. 11-26, 1996.

9. J. Will, M. Gödickemeier, L.J. Gauckler, "Ceramic Current Collectors", Poster, Proc. SOFC IV, Aachen, Germany, pp. 757-761, U. Stimming, S. C. Singhal, H. Tagawa, W. Lehnert (Eds.), The Electrochem. Soc. New York, USA, 1997.

10. J. Will, R. Stadler, M. Hruschka, L.J. Gauckler, "Fundamentals of Ceramic Processing", Proc. NATO Advanced Summer School, Erice, Sicily July 14-24, Oxygen Ion and Mixed Conductors and their Technological Applications, 1997.

11. J. Will, L. Gubler, S. Al-Wakeel, L.J. Gauckler, "Electrophoretic Deposition of Zirconia", Poster, NATO Advanced Summer School, Erice, Sicily, July 14-24, Oxygen Ion and Mixed Conductors and their Technological Applications, 1997.

12. J. Will, L. Gubler, S. Al-Wakeel, L.J. Gauckler, "Electrophoretic Deposition of TZP on Porous Substrates", Ceramic Processing 1997, St. Barbara, USA, September 7-10, 1997.

13. J. Will, L.J. Gauckler, " Komponenten für planare, anodenseitig gestütze Fest-Elektrolyt-Brennstoffzellen" June, 26 University of Saarland, Chair of Powder Technology of Glass and Ceramics, Saarbrücken, Germany, 1998.

14. J. Will, S. Al-Wakeel, L.J. Gauckler, "Elektrophoretische Beschichtung von Anodensubstraten für die Herstellung dünner Elektrolytschichten", DKG Annual Meeting, Oktober 5-7, Erlangen, Germany, 1998.